Growth and Morphogenesis:
Quantifying 3D Surface Growth Patterns and Shape Changes in Developing Leaves

Lauren Remmler

Thesis submitted to the
Faculty of Graduate and Postdoctoral Studies
In partial fulfillment of the requirements
For the M.Sc. degree in
Biology with Specialization in Bioinformatics

Department of Biology
Faculty of Science
University of Ottawa

Abstract

Formation of organ shape is an intriguing yet largely unanswered question in developmental biology. Shapes arise as a result of tightly controlled spatial variation in the rates and directions of tissue expansion over the course of development; therefore, quantifying these growth patterns could provide information about the underlying mechanisms of morphogenesis. Here we present a novel technique and computational tools for quantifying growth and shape changes in developing leaves, with a few unique capabilities. This includes the ability to compute growth from three-dimensional (3D) coordinates, which makes this the first method suitable for studying leaf growth in species or mutants with non-flat leaves, as well as small leaves at early stages of development, and allows us to simultaneously capture 3D shape changes. In the following, we apply these methods to study growth and shape changes in the first rosette leaf of *Arabidopsis thaliana*. Results reveal clear spatiotemporal patterns in growth rates and directionality, and tissue deformation maps illustrate an intricate balance involved in maintaining a relatively flat leaf surface in wild type leaves. Semi-automated tools presented make a high throughput of data possible with this method, and algorithms for generating mean maps of growth will make it possible to perform standardized comparative analyses of growth patterns between wild type and mutants and/or between species. The methods presented in this thesis will therefore be useful for studying leaf growth and shape, to further investigate the mechanisms of morphogenesis.

Résumé

Comment un organe acquiert sa forme particulière au cours du développement est une question intéressante mais largement non résolue. La forme d'un organe résulte de la façon dont les taux et directions de croissance de ses tissues varient dans l'espace et dans le temps. Quantifier les motifs de croissance est donc nécessaire pout élucider les mécanismes sous-jacents de la morphogenèse. Nous présentons ici une nouvelle méthodologie pour quantifier la croissance et les changements de forme dans les feuilles en développement. Cette méthodologie s'appuie sur le développement de nouvelles techniques expérimentales et de programmes informatiques, et présente des avantages uniques : la croissance de la surface des feuilles et le changement de forme peuvent être analysés en trois dimensions (3D), pour une longue période et de large déformations. De plus l'analyse de multiples échantillons permet de générer une cartographie moyenne des motifs de croissance à la surface des feuilles au cours de leur développement, ainsi qu'une description quantitative de la déformation des tissus sous l'effet de leur croissance. Dans cette thèse, nous présentons les résultats de croissance et de changements de forme de la première feuille de rosette d'*Arabidopsis thaliana* au cours de son développement. Les cartes moyennes de croissance révèlent des motifs spatio-temporels évidents tant pour les taux que pour les directions de croissance. De plus, la description de la déformation des tissus démontre l'équilibre complexe impliqué dans le maintien d'une surface relativement plane dans les feuilles. La méthode proposée et les logiciels associés permettra d'effectuer des analyses comparative de la croissance entre feuilles de type sauvage et feuilles de mutants aux formes altérées, afin d'élucider les mécanismes de la morphogenèse foliaire.

Table of contents

List of Tables

Chapter 3

Chapter 4

List of Figures

Chapter 1

Chapter 2

Chapter 3

Chapter 4

Chapter 5

Frequent Acronyms and Variable Names

DAS	Days after sowing
SVD	Singular value decomposition
p	Scaling factor along the maximal direction of growth
q	Scaling factor along the minimal direction of growth
RGR	Relative growth rate
RSE	Relative standard error
rmsd	Root mean square deviation
rcr	Relative curving rate

Statement of Contributions of Collaborators and Co-Authors

Chapter 2: "Computational tools for quantifying growth in developing leaves from 3D vascular coordinates"

Authors and Contributions: L. Remmler, R. Assaf, and A.G. Rolland-Lagan
A.G.R.L. designed the research. L.R. performed the research with advice from A.G.R.L., using data collected by R.A. L.R. wrote the manuscript.

Publication plan: some parts to be included in the following
"Quantifying vein patterns in growing leaves" (in preparation)
R. Assaf, L. Remmler, and A.G. Rolland-Lagan

Chapter 3: "Quantifying growth patterns at the leaf surface"

Authors and Contributions: L. Remmler and A.G. Rolland-Lagan
A.G.R.L. designed the research. L.R. and A.G.R.L. did the research. L.R. wrote most of the programs. L.R. did the data analysis. L.R. and A.G.R.L. wrote the manuscript.

Publication plan: submitted

Chapter 4: "Quantifying tissue deformation: the link between growth patterns and shape deformations"

Authors and Contributions: L. Remmler and A.G. Rolland-Lagan
L.R. and A.G.R.L. designed the research. L.R. and A.G.R.L. did the research. L.R. wrote all the programs, and wrote the manuscript with advice from A.G.R.L.

Publication plan: to be submitted

Acknowledgements

First and foremost I would like to thank my thesis supervisor Dr. Anne-Gaëlle Rolland-Lagan for providing me such an interesting project to work on. Your insight and guidance has been invaluable, and your steady flow of creative ideas has made for an exciting research experience. Your encouragement has been deeply appreciated, and working in your lab has been such a pleasure. I am excited and grateful to have the opportunity to continue working with you and learning from you!

Thank you also to my committee members Dr. Robert Laganière and Dr. Shelley Hepworth for all of their helpful ideas and encouraging feedback throughout my project. Thanks to Dr. Stéphane Aris-Brosou for his feedback on parts of the thesis used in class projects, and Dr. Howard Rundle for reviewing the final thesis.

Thanks to lab members Mira and Rebecca who took the time to train me in various lab procedures, and for their support and camaraderie throughout my graduate student experience – your friendship has been an equally valuable outcome of the past two years! Thanks to Alice Syzmanski for her assistance and company during some late nights developing some of the techniques of this thesis.

Thank you to *all* of the Rolland-Lagan lab members and other colleagues at the university for providing a fun workplace environment and a sense of community that was also an important aspect of making all the time I've spent in the lab enjoyable. Thank you to other friends who made sure I got away from the lab once in a while too, and all of my friends and family for their support and encouragement during my studies.

Chapter 1: General Introduction

1.1 Thesis outline

This thesis is presented as a series of articles on related but distinct projects (Chapters 2-4), preceded by a General Introduction (Chapter 1) and followed by a General Conclusion (Chapter 5).

The project began by developing computational tools for quantifying leaf surface growth from 3D coordinates of vein branching points, as part of another project on the quantification of vein patterning in leaves (Assaf et al., in prep). These results are presented in Chapter 2, as a stand-alone report of the thesis author's work.

This was used as a foundation for the main project of this thesis, which involved the development of a new technique for quantifying leaf growth using topically applied microscopic fluorescent particles. We also developed additional computational tools to allow for a higher throughput of data, and more detailed analyses of growth patterns. This project is presented in Chapter 3, as an adaptation of a manuscript which has recently been submitted.

As we analyzed the results of Chapter 3, we realized it would be helpful to develop tools to show the deformation of tissue during growth, and to quantify changes in the 3D leaf shape. This makes it possible to follow changes in growth parameters within specific regions of tissue over time as they move throughout the leaf, and to link growth patterns to shape changes. This work is presented in Chapter 4, as an adaptation of a manuscript we are preparing for publication.

Each chapter thus has its own introduction and discussion specific to the content of the chapter. To minimize repetitiveness, the General Introduction is limited to an overview of background information pertinent to the thesis rationale, and additional information on and explanations of concepts that will reappear in the main chapters. By the same token, the General Conclusion contains a summary and integration of the contents of the three articles, and a broader overview and exploration of future research directions.

Note that the list of references is given at the end of the thesis, while supplemental figures and data referred to in Chapters 2-4 can be found at the end of the chapter in which they are cited.

Supplemental videos and custom software presented in the thesis will be made available on the Rolland-Lagan website (www.science.uottawa.ca/~arolland) in the future.

1.2 Describing and quantifying parameters of growth

1.2.1 Descriptors of growth

Growth is often described simply by a rate of expansion in length, volume, or area. In most cases however, this does not provide a complete description of growth. Growth directionality, or anisotropy, must also be considered.

Anisotropic growth occurs when material expands preferentially in one direction (as opposed to isotropic growth, in which tissue expands equally in all directions). As illustrated in Figure 1.1A-C, anisotropy and growth direction can play a very important role in determining the shape outcome of a material after expansion.

The main direction of growth, i.e. the direction of anisotropic expansion, is referred to as the direction of maximal growth. The direction of minimal growth is, by the laws of mechanics, always oriented orthogonally to this axis. Anisotropy is the ratio between the growth rate in these two directions; e.g. if a square were to double in height and quadruple in width, the anisotropy would be 2.0.

Rotation may also occur during growth (Figure 1.1D) when there is variation in growth rates, anisotropies and/or directions in neighbouring material, due to the interconnectivity of the material. Thus, rotation is not a local property of the material, but it reflects overall shape changes.

These descriptors of growth – the main direction of growth, anisotropy, and rotation - are related to a group of growth defining variables referred to as strain parameters, which are explained in section 1.2.2.

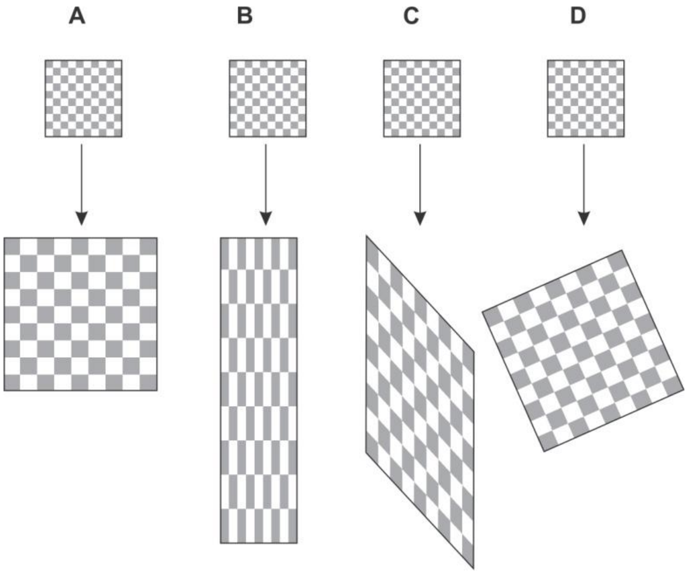

Figure 1.1: Different shape outcomes as a result of anisotropy and rotation.

Squares at the top represent tissue before growth and those at the bottom represent the material after growth. Growth rates are homogenous across the squares, and are equal in all three examples, i.e. the area of the material after growth is the same in A-C. The chequered pattern illustrates how landmarks on or within the material would be deformed.

(A) The square grows isotropically, i.e. equally in all directions.

(B) The square grows anisotropically along the vertical axis and becomes elongated into a rectangle.

(C) The square grows anisotropically along an oblique angle, resulting in a new parallelogram shape.

(D) The square grows isotropically but rotates during growth resulting in a “diamond” shape.

1.2.2 *Strain parameters and the growth transformation matrix*

Growth strain parameters can be computed via singular value decomposition (SVD) of a growth transformation matrix (see Goodall and Green, 1986). In Chapters 2-3, our 3D data will be adapted to compute growth via this method; therefore, it may be useful to have an understanding of the steps involved and the mathematical interpretations of growth strain.

Computing growth strain parameters

Let's consider growth of a triangular region. At the first time point the triangle vertices' coordinates lie at A, B, and C, which we will store in a vector named T1. At a later time points, the triangle coordinates have moved to a new position; we will refer to these as A', B', and C', and store them in T2. By centering T1 and T2 at the origin, we can define each triangle with any two points, as the third can now be deduced. We then have:

$$\mathrm{T1} = \begin{pmatrix} \mathrm{xA} & \mathrm{yA} \\ \mathrm{xB} & \mathrm{yB} \end{pmatrix} \rightarrow \mathrm{T2} = \begin{pmatrix} \mathrm{xA'} & \mathrm{yA'} \\ \mathrm{xB'} & \mathrm{yB'} \end{pmatrix}$$

The mathematical transformation of these points can be written as

$\mathrm{T1} \times \mathrm{Tr} = \mathrm{T2}$

Where, Tr is a 2x2 transformation matrix with the form

$\mathrm{Tr} = \begin{pmatrix} a & b \\ c & d \end{pmatrix}$, and can be calculated by

$\mathrm{Tr} = \mathrm{T2} \times \mathrm{T1}^{-1}$.

Goodall and Green (1986) defined four intermediate quantities that can be computed from the transformation matrix as follows:

$$t = [(a+b)^2 + (b-c)^2]^{1/2}$$
$$w = [(a-d)^2 + (b+c)^2]^{1/2}$$
$$\tau = \arctan[(b+c)/(a-d)]$$
$$\omega = \arctan[(b-c)/(a+d)]$$

From these intermediate quantities, we can calculate the strain parameters,

$p = (t + w)/2$

$\theta = (\tau - \omega)/2$

$q = (t - w)/2$

$\Psi = (\tau + \omega)/2$

which give meaningful information about growth, as explained in the following section.

The growth transformation matrix

Growth strain parameters are often represented graphically by strain crosses. Strain crosses consist of two orthogonal arms, where the orientation of the arms indicate the direction of maximal and minimal growth, and the length of the arms represent the relative growth rates in those directions. Strain crosses are actually a visual representation of the growth transformation (Figure 1.2A).

With the strain parameters, we can reconstruct the growth transformation matrix as a product of three separate more meaningful transformations:

$$\mathrm{Tr} = \begin{pmatrix} \cos\theta & -\sin\theta \\ \sin\theta & \cos\theta \end{pmatrix} \begin{pmatrix} p & 0 \\ 0 & q \end{pmatrix} \begin{pmatrix} \cos\psi & \sin\psi \\ -\sin\psi & \cos\psi \end{pmatrix}$$

$$= T_\theta \times T_{pq} \times T_\Psi$$

The first transformation applied, T_θ, is a rotation matrix that rotates the material clockwise, by θ (Figure 1.2B). Secondly, T_{pq}, which is a simple affine scaling matrix, scales the material along the x-axis by a factor of p, and along the y-axis by a factor of q (Figure 1.2C). Lastly, T_Ψ rotates the material counter-clockwise by Ψ (Figure 1.2D) to bring the material into its final position after growth.

The conventions of SVD dictate that the result p is always greater than q; therefore, p and q tell us the maximal and minimal scaling factors, respectively. As the material was first rotated clockwise by θ to orient the p

with the x-axis, the angle θ tells us the direction of maximal growth with respect to the original coordinates of the material as measured from the positive x-axis.

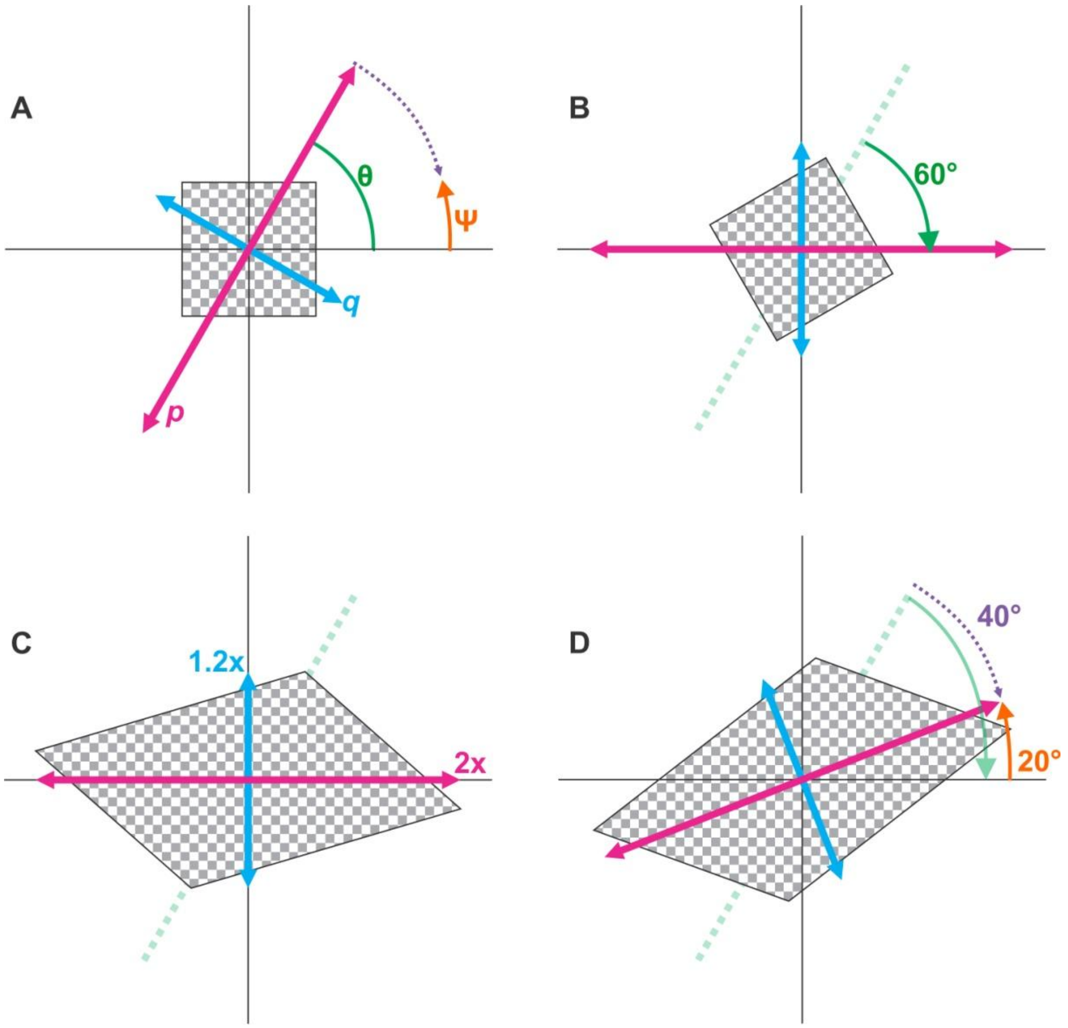

Figure 1.2: Strain crosses and the growth transformation.

(A) A square of material at time *t*, with the four strain parameters, *p, q,* ψ and θ, labelled on their respective features of the strain cross.

(B) T_{θ} rotates the material clockwise by θ to align the maximal direction of growth with the x-axis.

(C) T_{pq} scales the material by factors *p* and *q* in the x and y axis respectively

(D) T_{Ψ} rotates the material counter-clockwise by Ψ, to bring the material into its final position after growth, at time *t+1*. The difference between θ and ψ gives the angle of actual overall rotation of the material, shown in purple.

Of course in reality, the material does not rotate itself around to line up with an x-axis before growing, and then rotate back. This is simply the mathematical interpretation of growth as defined by the growth strain parameters. The overall counter-clockwise rotation that the material actually experiences during growth is Ψ-θ.

1.3 The link between growth and shape

The identity and function of any object, appendage, organ, or organism is largely determined by its material and its shape. In the making of a man-made object, the appropriate materials are assembled into a functional structure according to a blueprint, while in nature, all of the organs and appendages of an organism arise from a single cell. The generation of different tissue types from this single cell origin is becoming increasingly understood from studies of cell differentiation, but what directs the highly structured organization of the tissues into specific patterns and functional shapes within an organism remains an intriguing but difficult question in the field of developmental biology (Coen et al., 2004; Tsukaya, 2006).

The development of shape is most predominantly determined by spatial growth patterns (Piazza et al., 2005); as depicted in Figure 1.3, a variety of shapes can be produced simply through spatial heterogeneities in growth. These growth patterns may result from variations in the concentration, distribution, and flux of growth regulating biochemical signals, as well as from mechanical constraints. Quantitative data on spatial growth patterns could provide information about the interactions, gradients, and regulation of biochemical or biophysical signals, which will aid in improving our understanding of the mechanisms of genetic and environmental influences on shape, through their effects on growth.

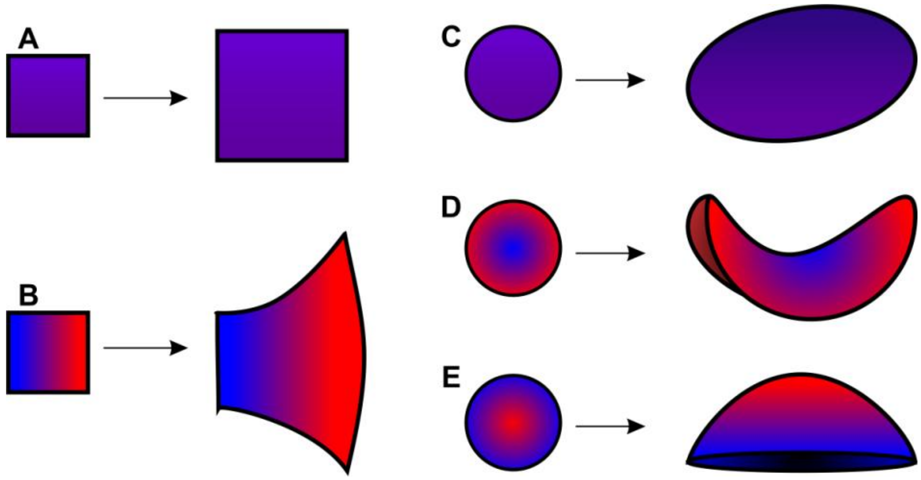

Figure 1.3: Various 2D and 3D shapes arise through differences in spatial growth patterns.

Tissues that are initially the same shape before growth (the left side of the arrows), morphose into different 2D (A-B) and 3D (C-D) shapes (right side of arrows). Colours reflect growth rates, ranging from high (red) to low (blue). C-E is adapted from Nath et al. 2003.

1.3.1 D’Arcy Thompson’s grid transformations

Nearly a century after its publication, D’Arcy Thompson’s book On Growth and Form (1917) remains a popular and well-respected piece of literature among developmental biologists. In this book, he presented a unique approach for analyzing shape differences, with intriguing results; he showed that in many cases, a set of points defining the morphology of one species could be deformed to produce the morphology of a related species, using a set of relatively simple mathematical transformations.

These results suggest that the evolution of different morphologies could be explained by genes involved in morphogen signals, which lead to slight changes in the spatial and/or temporal growth patterns of that species, such as gradients of growth or anisotropy. For example, compare Figure 1.4A to Figure 1.1C showing the outcome of anisotropic growth of a square, and Figure 1.4B to Figure 1.3B showing the outcome of growth in a square with a linear gradient of growth rates.

However, looking at morphological differences between the final adult forms of species only hints at this; obviously, these differences arise through the accumulation of differences in development. To investigate this, growth and shape changes occurring throughout the development of the two species being compared would need to be quantified.

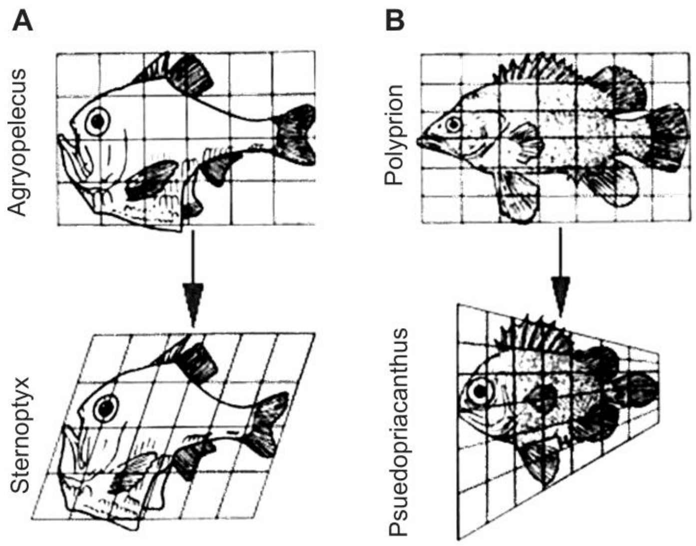

Figure 1.4: D'Arcy Thompson's grid transformations.

Thompson showed how different morphologies of related species can be derived from one another through simple affine transformations. In these images he illustrates this in fish species. A square grid is superimposed on the form of one species (above arrows). On a related species, a grid with lines that fit through the corresponding morphological features (below arrow) can be obtained from a simple deformation of the square grid. Adapted from Thompson, 1917.

1.4 The importance of studying leaf growth

Leaves are the vegetative organs of plants and the main sites of photosynthesis, and their development is of significant botanical, biological, and agricultural interest. Leaves serve as good subjects for the study of growth, given their relatively planar structure, visual accessibility, rigid cell walls and adhesive intercellular material that prevent cell migration from contributing to growth (Cosgrove, 2005), and the controllability of growth conditions.

Diverse leaf shapes across plant species have evolved to maximize success for the plant's particular environment, by expanding the leaf photosynthetic surface, offsetting water loss, improving convective cooling across the leaf, and withstanding external forces (Cronk, 2009). In addition to the biological importance to the plant, leaf growth and shape is also of major economical importance in crop species. Photosynthetic rate is primarily determined by leaf area, and so plant biomass accumulation rate is directly dependent on leaf growth rates (Tardieu and Granier, 2000). Knowledge of molecular and genetic pathways and interactions involved in leaf growth could therefore be useful in bio-engineering of crops with higher yields, faster growth rates, or better environmental tolerances.

1.4.1 The use of Arabidopsis as a model organism for studying growth

Arabidopsis (*Arabidopsis thaliana* (L.) Heynh) is a small flowering plant of the mustard family, which includes economically important crop species such as turnip, cabbage, broccoli, and canola. Arabidopsis is commonly used by plant biologists as a model organism due to its fast life cycle, small size, high reproduction rate, and simple, fully sequenced genome, as well as the homology of many of its genes and proteins across the plant kingdom (The Arabidopsis Genome Initiative, 2000). Its relevance in the study of plant growth processes is supported by the fact that many genes and hormones that have been found to increase growth in Arabidopsis have similar roles in various crop species such as potato, tomato, and rice (Gonzalez et al., 2009).

1.5 Methods for quantifying leaf growth

Quantification of spatial growth patterns requires tracking landmarks distributed across the tissue in question. Early efforts to measure growth, dating back to 1933, involved drawing ink dots on the leaf surface to delineate a grid of small rectangles (Avery, 1933; Richards and Kavanagh, 1943). Other studies since then have employed the same concept of quantifying growth at the leaf surface by tracking ink marks (Poethig and Sussex, 1985; Granier and Tardieu, 1998; Wang et al., 2011; Saurer and

Possingham, 1970; Maksymowych, 1962), or vein intersections (Wolf et al., 1986; Walter and Schurr, 1999; Walter et al., 2003; Taylor et al., 2003; Erickson, 1966; Maksymowych, 1959).

Quantifying growth can be impeded by the time-consuming task of manually tracking and measuring coordinates of landmarks over time. One of the first computational tools in the field of botany, published in 1966 by Erickson, was a computer program for measurement and calculation of leaf growth strain (Erickson, 1966). More recently, the laborious task of identifying and tracking landmarks has also been greatly aided by digital image sequence analysis software packages. These employ low-level motion analysis algorithms to measure growth by following the displacement of all identifiable features in time lapsed video images of a leaf (Schmundt et al., 1998; Ainsworth et al., 2005; Wiese et al., 2007).

A significant limitation of all currently available methods is that they are not applicable to leaves in early stages of development, in which major shape changes and growth processes occur. This is because drawing or printing ink dots on the leaf surface require that the leaf be relatively large, and vascular features are not visible in leaves at early stages of development. In the case of digital image sequence analysis, the experimental set-up requires the leaf to be pulled flat under a camera by tension from a frame at the leaf base and weights clipped to the tip and sides (Schmundt et al., 1998) or from weights threaded through the margins of the leaf (Figure 1.5) (Wiese et al., 2007); this would require that the leaves be relatively large. Furthermore, it is known that developing plants can sense and respond to external forces (Chehab et al., 2009), and so it would be very difficult to apply the constraints without some interference to the natural growth patterns.

Also, leaves that have a certain curvature simply cannot be held flat without folding or tearing, and so this method is limited to the study of relatively flat leaves. None of the existing techniques involve methods for extracting 3D coordinates of the landmarks nor algorithms for computing growth from 3D data, which greatly limits their applicability. Many leaf mutants with altered growth have altered 3D shapes (e.g. White, 2006; Nath et al., 2003) and there has been increased interest in the past decade in more geometrically complex leaf shapes, such as such as those with stronger curvatures, rolling, ruffling, wrinkling, and twisting (Tsukaya, 2006; Piazza et al., 2005; Cronk, 2009; Walter et al., 2009; Micol, 2009). However, as many researchers have pointed out, methods to study the growth of such three-dimensional surfaces are not available.

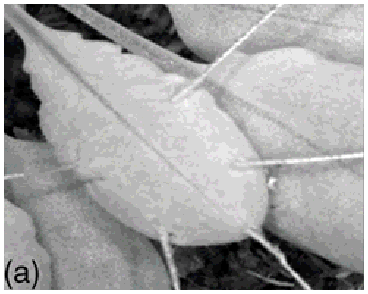

Figure 1.5: Experimental set-up digital image sequence analysis method. The leaf is pulled into a flat position by weights threaded through its margins. From Wiese et al., 2007.

1.6 Thesis objectives

The purpose of this thesis was to develop a new approach for quantifying leaf growth patterns to overcome the limitations of currently available methods. Namely, we sought to develop a method that allows growth to be measured from early stages of development, and from 3D coordinates. This furthermore required the development of novel computational tools for data extraction, calculation, analysis, and display. We also aimed to quantify and describe shape changes and tissue deformation over the course of development, to provide a complete picture of the link between organ growth patterns and morphogenesis.

Chapter 2: Computational tools for quantifying growth in developing leaves from 3D vascular coordinates

2.1 Summary

In this chapter we present a new technique for quantifying leaf growth from 3D coordinates of leaf vascular landmarks, and tools for computing mean spatial maps of growth that will make it possible to compare and identify altered growth patterns in mutant plants. We apply these tools to data obtained from a previous analysis of vein patterning, and compare the results to a previously existing method for computing growth from 2D projections of the coordinates. We find that the 2D projection method is quite accurate for computing growth rates and anisotropy in relatively flat leaves, but the addition of the algorithms for computing results from 3D coordinates will make it possible to study more curved leaves in the future. Furthermore, we present another tool for computing growth rates along the midvein, which may be useful as a fast way to approximate the proximodistal gradient of growth observed in the mean spatial maps.

2.2 Introduction

Tools that allow researchers to quantify the tightly controlled spatial and temporal patterns in the rates and directions of tissue expansion over the course of development could be extremely useful in studying the underlying mechanisms of morphogenesis. Tools to quantify these parameters in leaves, more specifically, would be of interest not only to developmental biologists, but also to researchers in the fields of evolutionary biology, agriculture, and biotechnology. Thus it is not surprising that some such tools do exist, but to date are only applicable to leaves in later stages of development, when most growth and shape changes have already occurred.

The Rolland-Lagan lab recently developed a non-invasive procedure which allows us to image leaves *in vivo* and to acquire data on the 3D position of fluorescent vascular landmarks on the leaf (Assaf et al., in prep). This can be done without mechanical manipulation of the leaves, and is applicable to the leaves from an earlier stage of development than has been previously possible. Preliminary work was done to measure growth in 2D by projecting vascular coordinates onto a plane fitted through the 3D coordinates of the leaf surface, and tracking the divergence of these vascular coordinates over time. In the following we present adaptations and additions to the existing software that allow us to compute growth from the 3D coordinates of vascular landmarks. This will not only improve the accuracy of our growth measurements, but will make it possible to use this method to study leaves with more complex 3D curvatures, which has not previously been done.

We also present a new tool for quantifying and describing 3D growth rates along the proximodistal axis of the leaf. A proximodistal gradient of growth, with growth rates being highest at the base and lowest at the tip, has been observed in most other leaf growth studies (Poethig and Sussex, 1985; Granier and Tardieu, 1998; Wang et al., 2011; Saurer and Possingham, 1970; Maksymowych, 1962; Wolf et al., 1986; Wolf et al., 1986; Walter and Schurr, 1999; Walter et al., 2003; Taylor et al., 2003; Schmundt et al., 1998; Wiese et al., 2007). As such, there may be cases in which is it somewhat redundant to quantify growth across the entire leaf, and it may be sufficient to simply quantify growth along the proximodistal axis. Here we compute growth of vein segments along the midvein, which could serve as a useful tool for a quick assessment of leaf proximodistal growth gradients.

2.3 Methods and computational tools

2.3.1 Plant materials and microscopy

All data used in this analysis was collected by lab member R. Assaf with assistance from M. Tu. using experimental procedures developed by R. Assaf and thesis supervisor A.G. Rolland-Lagan.

The protocol employs the AtSuc2prom:GFP (strain cs9105 available from www.arabidopsis.org), which has GFP fluorescence in the vascular tissues. The seeds are sterilized and imbibed in water for four days at 4° C, then grown in soil in the lab on a 16 hour light cycle at 23°C on light shelves (ArabiSun Lighting System from Lehle Seeds). In the results presented here, leaves were imaged every 24 hours from 11 to 19 days after sowing (DAS11-19) with a Leica Z16 APO A MacroFluo fluorescence macroscope (from Leica Microsystems).

The Leica Application Suite is used to take a series of images, referred to as z-stack images, within a range of user-specified depths of focus. The series of images is then be processed by the LAS Montage software to create a sharp composite image and a depth map, by identifying the in-focus regions of each z-stack image with an algorithm similar to that described by Widjanarko et al. (2002). The application also saves details such as the vertical step size between focal planes and the resolution of the image in millimetres per pixel, in xml files. This is done first under reflective brightfield lighting in order to obtain a depth map (Figure 2.1A), and then under fluorescence to view the leaf vasculature (Figure 2.1B).

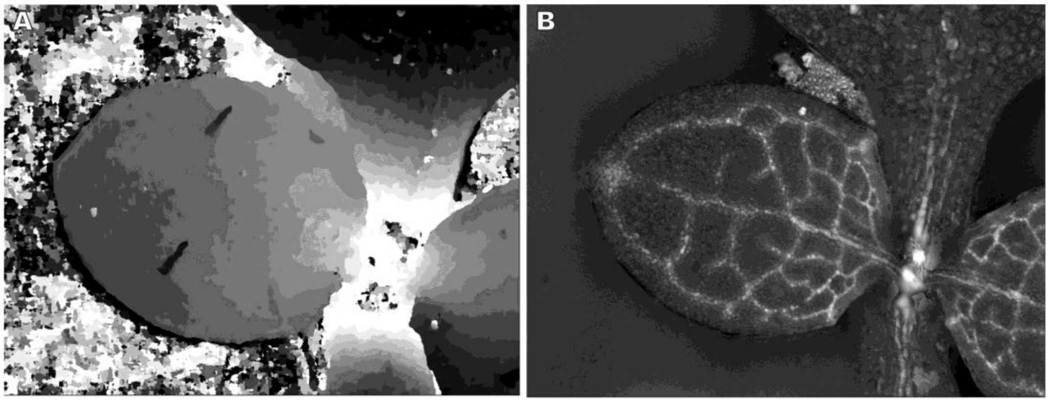

Figure 2.1: Microscope images generated for extraction of 3D surface and vein positions.

Leica LAS Montage Module images generated from z-stack images of an Arabidopsis AtSuc2prom:GFP leaf. We use the brightfield z-stack to obtain a depth map (A), and the fluorescence z-stack to obtain a multifocus montage image of the fluorescent vasculature (B).

2.3.2 Extracting vascular landmarks in 3D

Note that the programs described from this point forward were developed by our lab in Matlab (from The Mathworks, Inc.) unless otherwise noted.

The 2D projection of the leaf outline and vein network are digitally traced from the microscope images (Figure 2.1) using a custom user interface previously developed (Rolland-Lagan et al., 2009). Branching points, i.e. the intersections of veins, are automatically identified by a program which finds start or end points of the traced vein segments that are connected to others.

The 3D coordinates of the outline and of the leaf are extracted from the depth map. In the depth map, all of the regions of the specimen that are in focus at a particular focal plane are coloured in a particular shade of gray. For example, in Figure 2.1A, there are 5 distinct focal planes. However, in reality we know that the leaf is curved and spans in-between the focal planes. To convert the depth map from a surface of flat steps to a more realistically curved surface, it is “smoothed” using a square averaging window with dimensions of 50x50 pixels (on the 1041x1393 image) using the *fspecial* and *imfilter* functions from Matlab’s Image Processing Toolbox.

However, we do not want to average values near the leaf edges with depth map areas outside of the leaf outline, so before the depth map can be smoothed, those areas beyond the outline are cropped out, and then replaced with values from the leaf perimeter. See Figure 2.2B. Finally, using the vertical step size (stored by the microscope software in xml files), we convert grayscale pixel values to actual vertical height values.

The 3D leaf surface is then reconstructed by fitting a mesh over the area enclosed by the leaf outline and extracting z-coordinates at the corresponding positions on smoothed depth map (Figure 2.2D and SVideo 1). To align all samples in the same way, each leaf reconstruction is shifted and rotated so that it is centered on the origin, with the proximodistal axis in line with the y axis.

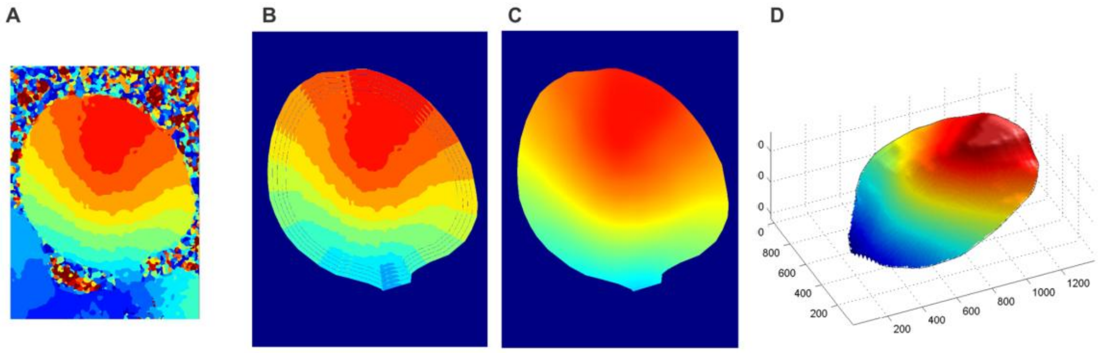

Figure 2.2: Depth map adjustments and 3D leaf reconstruction.

(A) Original depth map, displayed on a red-green-blue based colour scale (instead of grayscale) for better visual clarity.

(B) Data outside of the leaf outline are removed (appearing as dark blue in these images), and the areas of the depth map corresponding to marginal regions of the leaf are stretched and added around the depth map several times.

(C) The depth map values are averaged in a 50x50 pixel window, to create a more realistically smooth leaf surface.

(D) Regions within the leaf outline are used to reconstruct the leaf in 3D.

2.3.3 *Tracking landmarks over time*

A tracking program displays images of a leaf at two successive time points, *t* and *t+1* (Figure 2.3). The user is prompted to match up all branching points in the two images by clicking with a computer mouse first on a branching point in the image of the leaf at time *t*, and then the corresponding branching point in the image of the leaf at time *t+1*. The identified points are added to a list of matched branching points for *t* and *t+1*. The user is asked to first select points along the midvein and indicate when this is complete so that a list of midvein points can be stored.

The z-position of each branching point is retrieved by using the x and y pixel coordinates of the branching points as column and row indices for the matrix of z-values. The true x and y positions of every point are calculated by dividing the pixel position by the image resolution (retrieved from the xml file).

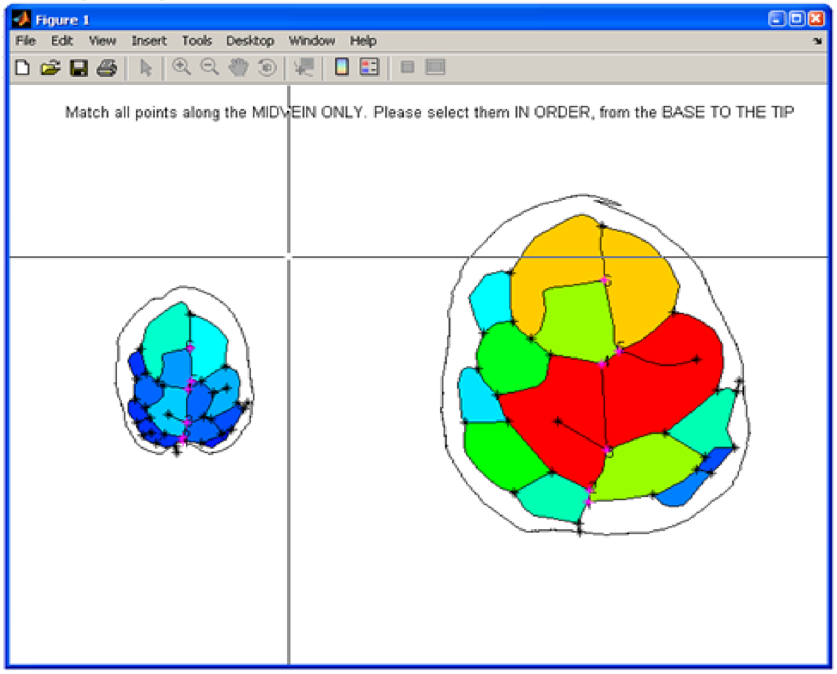

Match all points along the MIDVEIN ONLY. Please select them IN ORDER, from the BASE TO THE TIP

Figure 2.3: Interface for matching branching points over time.

A leaf at DAS7 is plotted in the left of the window, and the same leaf at DAS9 is plotted on the right. The user clicks on a branching point on the DAS7 leaf, and then on the corresponding branching point on the DAS9 leaf.

Note that the colours are from a separate set of vein patterning analysis programs that are used in conjunction with the growth programs presented here.

2.3.4 Computing growth rates along the midvein

The 3D length of each vein segment along the midvein is calculated from the 3D distance between adjacent branching points, for *t* and *t+1*. The increase in length of a segment between two time points represents the growth rate along that segment, normalized by dividing by the length of the segment. In other words:

$$RGR(t) = \frac{L(t+1) - L(t)}{L(t)} \times \frac{1}{\Delta t} \times 100\%$$

where *RGR(t)* is the relative growth rate of the segment for time *t, L(t)* is the length of the segment at time *t, L(t+1)* is the length of the segment at the next time point, and *Δt* is the time increment between *t* and *t+1.*

We add an additional “positioning” segment to the bottom of the midvein to cover the distance from the leaf base to the lowest midvein branching point, and one at the top to cover the distance between the highest midvein branching point to the leaf tip. These two additional segments make it possible to align segments from all leaf samples according to their relative position along the leaf proximodistal axis, by scaling each leaf’s segments to the mean leaf length.

2.3.4.1 *Adjusting mean midvein growth values*

We initially found that the growth of segments along the midvein fluctuated dramatically in some samples (Figure 2.4A). This is inconsistent with the results of other studies, and closer inspection revealed that it seems to be an artefact arising from limited resolution in the digitization of veins. Determining the position of branching points with high precision is not always possible, as vein fluorescence can be thick and patchy at larger resolutions (SFigure 2.2). In short segments, a very small discrepancy in the digitized position of the branching points that define it over time can have a dramatic effect on the relative length of the segment, and thus its apparent growth rate.

For this reason we decided to average the growth of any segment less than 10% of the total length of the leaf with the growth of the segments before and after it. In this round of smoothing, the values are weighted by a linear scale corresponding to the length of the segment in question, such that any segment under 2% of the leaf length is given a weight of zero in the averaging (i.e. the growth value assigned to these very short segments is based entirely on an average of the two surrounding segments), and any segment 10% of the leaf length and up is given a weight of one (i.e. is not averaged).

Inaccuracies in the branching point positions do not only affect short segments; a discrepancy at one branching point will cause one adjoining segment to appear shorter than its actual length and the other adjoining segment to appear longer than its actual length, leading to an erroneous decrease in the growth of the first segment and increase in the second. To reduce these effects, we also average all the growth values of all segments with their neighbours. The results of these two modifications greatly reduce the variation, as presented in Figure 2.4B.

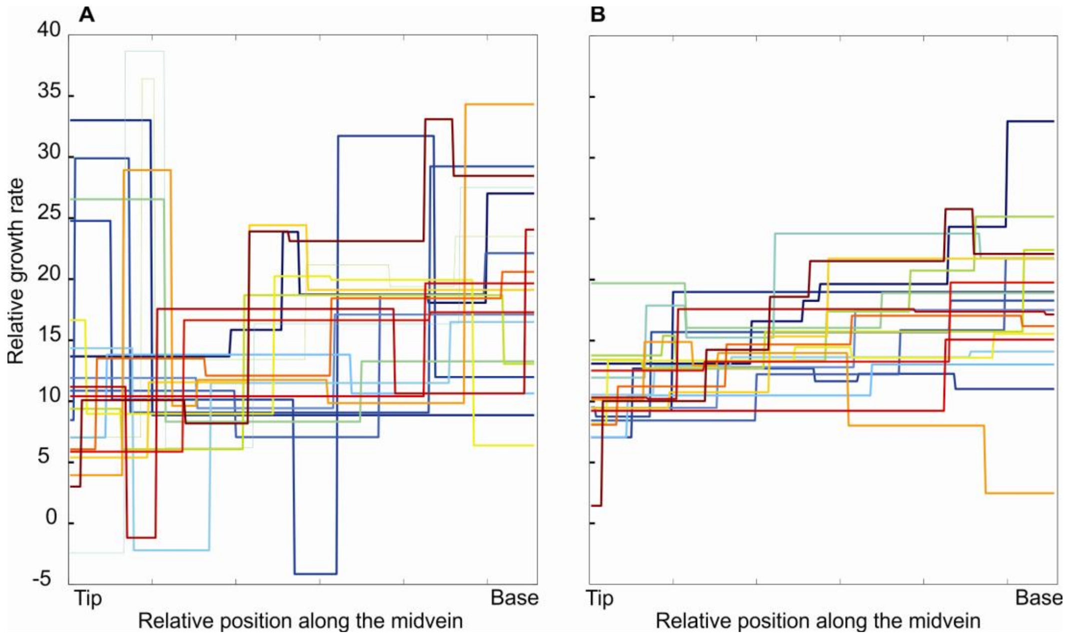

Figure 2.4: Effect of smoothing midvein results.

Relative increase in length along the midvein for all leaf samples at DAS11, with each sample shown in a different colour, before (A) and after (B) smoothing algorithm is applied.

2.3.5 Displaying mean midvein growth

A vector is created to store the growth rates along each sample's midvein, and the midvein coordinates are scaled to the length of a vector (Figure 2.5C). For each segment the rows of the vector that correspond to the segment's position along the midvein are filled with the growth rate value of that segment. Vectors for all samples are concatenated into a matrix (Figure 2.5D), and the values in each line are averaged horizontally and stored in a vector of the same length (Figure 2.5E). The vector of averaged growth rates is expanded horizontally for better viewing, and is displayed as an image with a colour map. Standard error (SE) for each row is computed in a similar manner, and the user can choose to display this adjacent to the growth bar in a colour bar, or to show the means and standard error in a scatter plot.

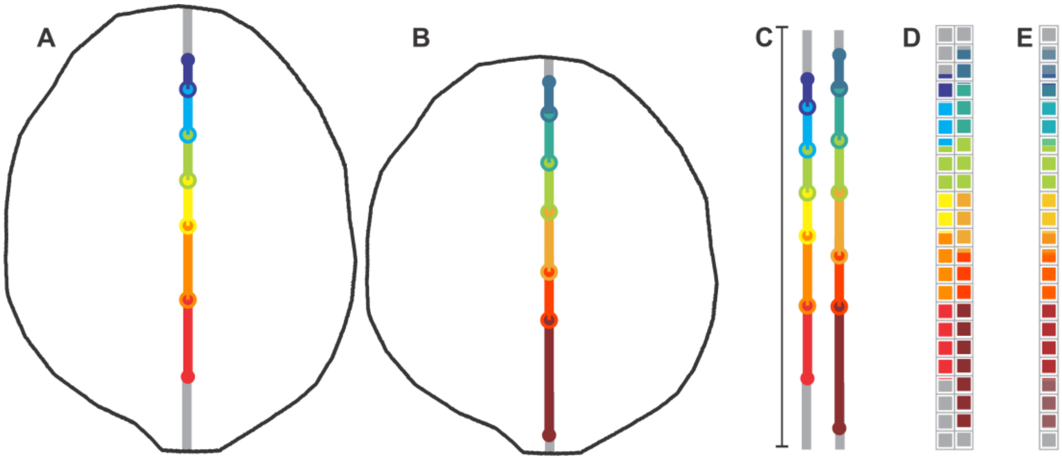

Figure 2.5: Illustration of algorithm for creating mean midvein vector.

(A-B) In this example we consider two leaf samples, A and B, of different sizes, with segment growth information at different positions along the midvein. The growth rate values of each segment are represented by colour. An additional segment with no values is added to the top and bottom of the leaf (grey lines).

(C)The coordinates of both leaves' midvein segments are scaled to the mean leaf length (black scale bar). The segments from the two samples are now aligned according to their relative position along the leaf.

(D) We scale these midvein segments again to a predefined vector length, and then add the growth rate value of each segment to the rows of the vector that correspond to the segment's position along the midvein, and concatenate the vectors of all samples.

(E) Each row is averaged to compute the mean growth rate at each position along the midvein and stored in the mean midvein vector.

2.3.6 *Computing growth from 3D coordinates*

To subdivide the surface into small regions that can be tracked over time, we apply a *Delaunay* triangulation function to connect all of the branching point coordinates through non-intersecting triangles; we apply the same triangulation on the matched branching points at the next time point. Using singular value decomposition (SVD) formulas, as explained by Goodall and Green (1986), it is possible to compute a variety of growth parameters for each triangle. However, these SVD calculations are not directly applicable to 3D landmarks. To compute growth strain parameters from 3D coordinates, we developed an algorithm to first rotate the triangle coordinates onto a 2D plane, as follows.

The triangle is first shifted so that one vertex lies at the origin (Figure 2.6A), and the normal vector to a plane fit through the triangle is found using the cross product of two of the triangle points. The projection of the angle of this vector in the x-y plane (α) is obtained, and is essentially equal to the 2D angle between the normal and the positive x-axis. The triangle is rotated clockwise around the z-axis by the angle α, bringing the projection of the normal in the x-y plane in line with the positive x-axis (Figure 2.6B). Consequently this puts the intersection of the triangle and the x-y plane along the y axis. The angle between the normal and a vector along the z-axis (β) is now calculated using the dot product. The projection of the normal is in line with the x-axis, so if the triangle is now rotated around the y-axis by the angle β, the normal will become perfectly aligned with the z-axis in 3D. The triangle will therefore now lie in the x-y plane (Figure 2.6C).

This procedure described in the above paragraph is applied to each triangle at time *t* and the same triangle at time *t+1* (i.e. after it underwent growth deformations). Now various parameters of growth can be computed from the time *t* and time *t+1* flattened triangles through singular value decomposition (SVD). These parameters include the direction of maximal growth (θ_f).), the rotation (ψ_f), and the scaling factors *p* and *q*. *p* is the scaling factor along the main direction of growth, and *q* is the scaling factor along the minimal direction of growth, which by the laws of mechanics is oriented orthogonally to the maximal direction of growth.

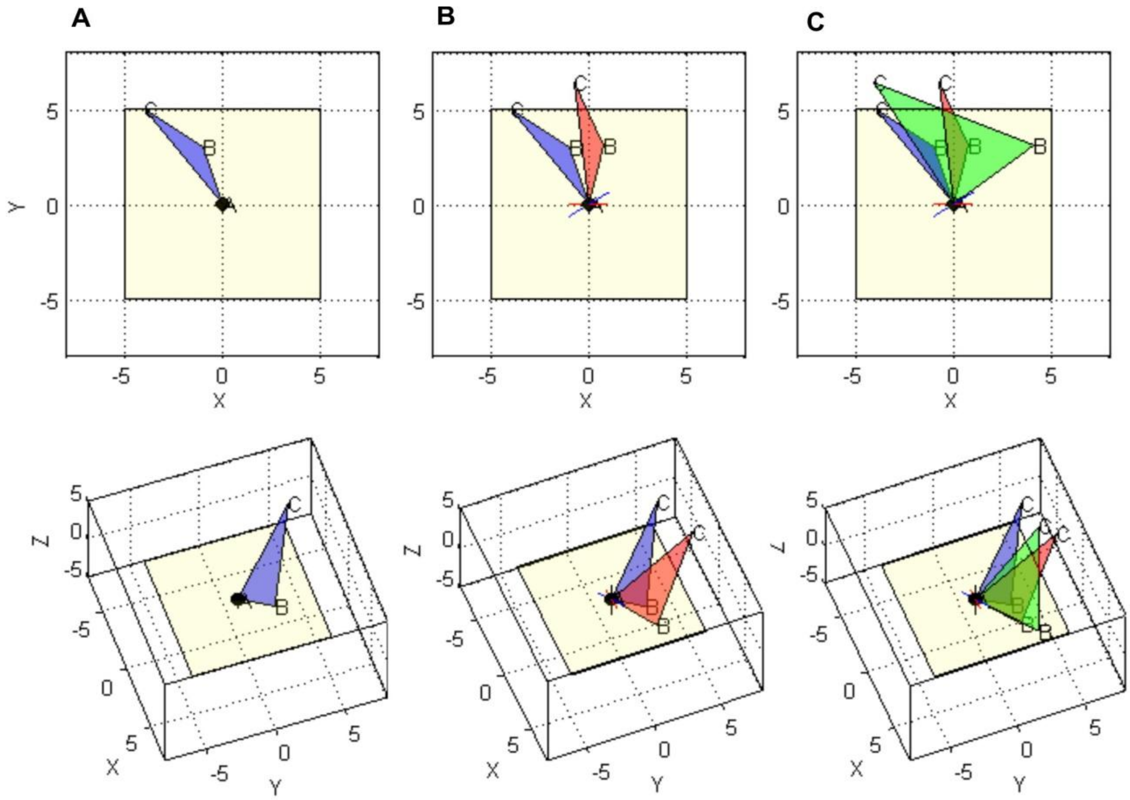

Figure 2.6: Illustration of the triangle flattening algorithm.

Each figure in the top row is shown from a 3D view in the figure directly below it.

(A)The triangle is shifted so that one vertex lies at the origin (black dot).

(B)The normal vector to a plane fitted through the triangle is found (blue line), and is used to rotate the triangle around the z-axis (red triangle) to bring the projection of the normal (red line) in the x-y plane in line with the positive x-axis.

(C)The triangle is now rotated around the y-axis, bringing the plane of the triangle to lie in the x-y plane.

Since the angles obtained are computed after the triangles have been rotated on to the x-y plane, the actual direction of growth and rotation of tissue must be adjusted to account for this. To compute the overall rotation of the triangle, we apply a total transformation matrix (the *t* flattening rotations, the rotations and scaling of growth, and the inverse of the *t+1* flattening rotations) to a unit vector aligned along the positive x-axis. The resulting position of the vector gives the final angle of rotation the tissue experienced during growth, as measured from the positive x-axis. To align the direction of growth with the position of the triangle within the 3D leaf, we apply the inverse of the *t* flattening rotations to a unit vector in the direction of θ_f.

The resulting angles for the direction of growth and rotation of tissue can be described by two components: the angle in the x-y plane, and the angle from the z-y (or z-x) plane. For the purposes of making deductions about growth signals, the relevant angle is the angle within the plane of the tissue. However this is complicated to visualize, since publications only allow for 2D images, or projections of 3D images, and since the leaf is fairly flat, we decided it was appropriate to just show the 2D projections of the angles. We convert all angles to reference angles in the range of ±90; this is because tissue expands along the main direction of growth with no forward or backwards orientation (so a direction of 45° is equivalent to 225°, for example).

From the scaling factors we compute the relative growth rate (RGR) for each triangle as:

$$RGR(t) = \frac{A(t+1) - A(t)}{A(t)} \times \frac{1}{\Delta t} \times 100\% = (p \times q) \times 100\%$$

where *RGR(t)* is the relative increase in area for the period of growth from time *t* to *t+1*, *A(t)* and *A(t+1)* is the area of the triangle at day *t* and *t+1*, respectively, and *p* and *q* are the scaling factors along the maximal and minimal directions of growth over time *t* to *t+1*.

Growth anisotropy, a measure of how preferentially growth occurs along the maximal directional growth, is computed from the ratio of the scaling factors, *p/q*. An anisotropy value of 1 indicates that growth is occurring evenly in all directions, and increasing values indicate that growth is occurring more predominantly along the main direction.

2.3.7 Making mean spatial maps

Using programs developed by Rolland-Lagan et al. (2009), the mean leaf shape for each time point is computed (Figure 2.7A), and the triangle coordinates of each leaf sample of that DAS are warped according to the difference between the sample leaf shape and the average leaf shape (Figure 2.7B-C).

Now, for each leaf sample, a “map” (2D matrix), is made in the shape of the mean leaf. To make a map of RGR, for each triangle on the leaf, the corresponding region of the map is determined and filled with RGR values of that triangle. This procedure is explained more thoroughly in Figure 2.8.

Maps of all samples are stacked into a 3D matrix, which is then averaged along the 3rd dimension at each point across the mean leaf shape (as illustrated in Figure 2.9), to produce a mean RGR spatial map.

This process is performed for all growth parameters, and repeated for all DAS’s.

The mean directions and rotations cannot be calculated through the usual arithmatic mean formula, since we are dealing with angles. For example, consider one sample which has a growth direction of 88° and another which has a growth direction of -84°; both have a direction of growth that is nearly aligned along the proximodistal axis of the leaf. The arithmatic mean of these two angles is 2°, but this would incorrectly suggest that the mean direction of growth occurs along the mediolateral axis of the leaf. To compute the mean direction and rotation we use circular statistics, as outlined by Zar (1996).

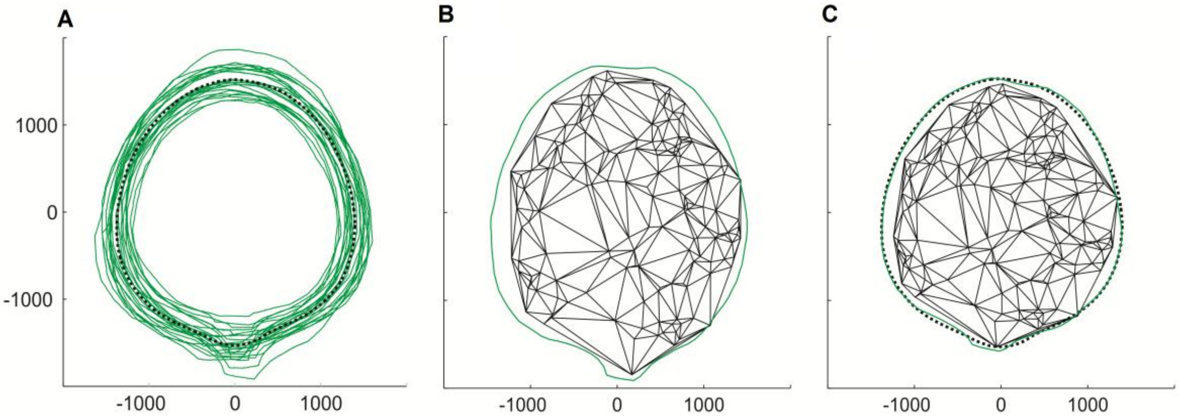

Figure 2.7: Warping samples to the mean leaf shape for computing mean maps.

(A) Leaf outlines of all samples at DAS11 in green, with the mean leaf outline for DAS11 plotted as the dotted black line.

(B-C) Warping of one DAS11 leaf sample coordinates (B) to the mean leaf shape (C).

Figure 2.8: Illustration of how a growth map is made, for the calculation of mean maps.

(A) A growth rate has been calculated for each triangle on the leaf, as indicated by the numbers plotted. The leaf has been centered on the origin (black dot) and warped to the mean leaf as explained in Figure 2.7.

(B) A mean map matrix with 200 rows and 182 columns is made.

(C) The leaf and landmark coordinates are shifted and scaled so that coordinates are all positive and lie between 1 and 200. These coordinates now correspond to the row and column number of the map matrix.

(D) A region of the shifted and scaled leaf has been zoomed in on; same region of the map matrix is shown by a grid laid over top.

(E) For each triangle on the shifted and scaled leaf, the coordinates defining the area it covers can be rounded to whole numbers and used to find the corresponding rows and columns in the map matrix; these elements of the matrix are then filled with the growth rate for that triangle. Note that the values displayed in the matrix appear upside down since row numbers are listed from top to bottom (as opposed to y coordinates which are plotted such that they increase from bottom to top).

(F) The final fully filled growth map matrix.

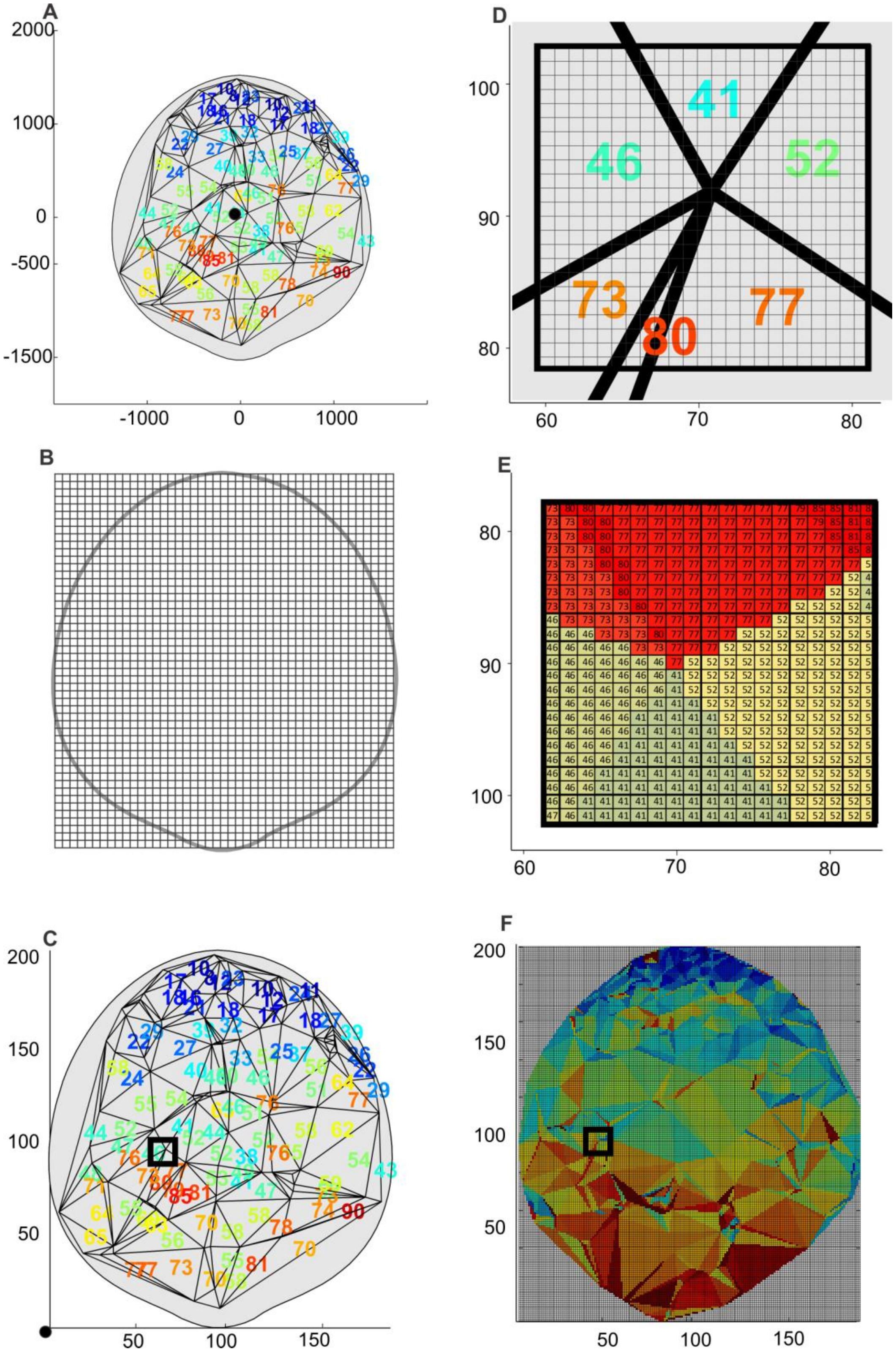

73	80	80	77	77	77	77	77	77	77	77	77	77	77	79	85	85	81	8
73	73	80	80	77	77	77	77	77	77	77	77	77	77	77	79	85	81	8
73	73	80	80	77	77	77	77	77	77	77	77	77	77	77	77	85	81	8
73	73	73	80	77	77	77	77	77	77	77	77	77	77	77	77	77	85	8
73	73	73	80	80	77	77	77	77	77	77	77	77	77	77	77	77	77	5
73	73	73	73	80	77	77	77	77	77	77	77	77	77	77	77	77	52	4
73	73	73	73	80	77	77	77	77	77	77	77	77	77	77	77	52	52	4
73	73	73	73	73	80	77	77	77	77	77	77	77	77	52	52	52	52	4
46	73	73	73	73	73	77	77	77	77	77	77	77	52	52	52	52	52	5
46	46	46	73	73	73	80	77	77	77	77	52	52	52	52	52	52	52	5
46	46	46	46	46	73	73	77	77	77	52	52	52	52	52	52	52	52	5
46	46	46	46	46	46	46	77	52	52	52	52	52	52	52	52	52	52	5
46	46	46	46	46	46	46	41	52	52	52	52	52	52	52	52	52	52	5
46	46	46	46	46	46	46	41	52	52	52	52	52	52	52	52	52	52	5
46	46	46	46	46	46	41	41	41	52	52	52	52	52	52	52	52	52	5
46	46	46	46	46	41	41	41	41	41	52	52	52	52	52	52	52	52	5
46	46	46	46	46	41	41	41	41	41	52	52	52	52	52	52	52	52	5
46	46	46	46	41	41	41	41	41	41	41	52	52	52	52	52	52	52	5
46	46	46	46	41	41	41	41	41	41	41	41	52	52	52	52	52	52	5
46	46	46	41	41	41	41	41	41	41	41	41	52	52	52	52	52	52	5
46	46	46	41	41	41	41	41	41	41	41	41	41	52	52	52	52	52	5
46	46	41	41	41	41	41	41	41	41	41	41	41	41	52	52	52	52	5
47	46	41	41	41	41	41	41	41	41	41	41	41	41	52	52	52	52	5

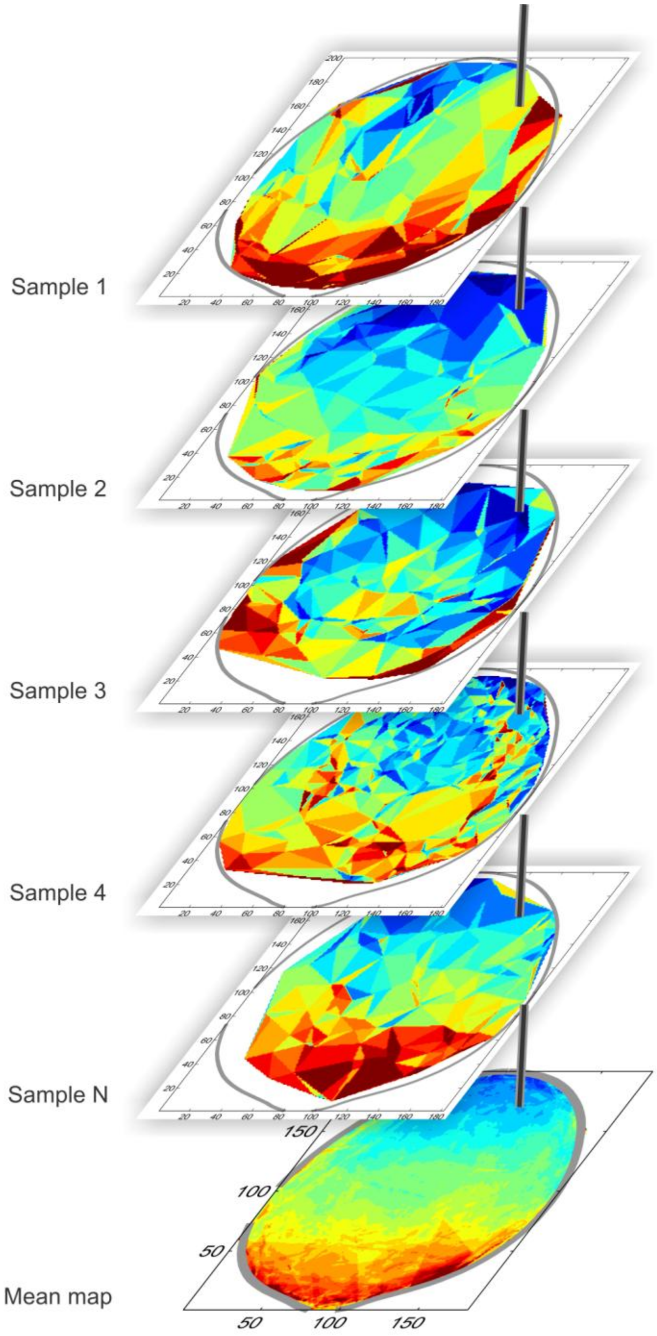

Figure 2.9: Illustration of how mean maps are made.

Once map matrices have been made for all leaf samples, as explained in Figure 2.8, all maps are stacked in a 3D matrix. Now, at each position across the mean leaf shape the values are averaged across all samples to produce the mean spatial map.

2.4 Results and discussion

As Chapter 3 contains a detailed analysis of growth, the discussion of these results will mainly be limited to an analysis of the method and comparison of 2D and 3D results.

2.4.1 Mean growth rates along the midvein

As expected, the results of mean growth rates along the midvein show a distinct proximodistal gradient of growth, with the highest rates at the base and the lowest rates at the tip (Figure 2.10). This gradient is consistent with what has been found by other leaf growth studies in a variety of species. The observation of this proximodistal gradient of growth has also been supported by several molecular and cellular-level studies that link this to cell-cycling patterns, where cells stop dividing first at the tip, then progressively toward the base (Tardieu and Granier, 2000; Granier and Tardieu, 1998; Donnelly et al., 1999).

Figure 2.11 shows the mean and standard error (SE) of the mean midvein growth rates (for visual clarity, we show DAS11 and DAS19 only). At all time points the SE tends to be higher at the base of the leaf; one may think this is due to the fact that the growth rates also tend to be higher at the base. However, the SE values were actually fairly similar for all time points, despite the fact that the mean growth rates become much lower over time. This tells us that a) growth rates near the base of the leaf tend to vary more among samples, and b) growth rates become more variable over time (or possibly growth rate measurements become less accurate as the leaf grows).

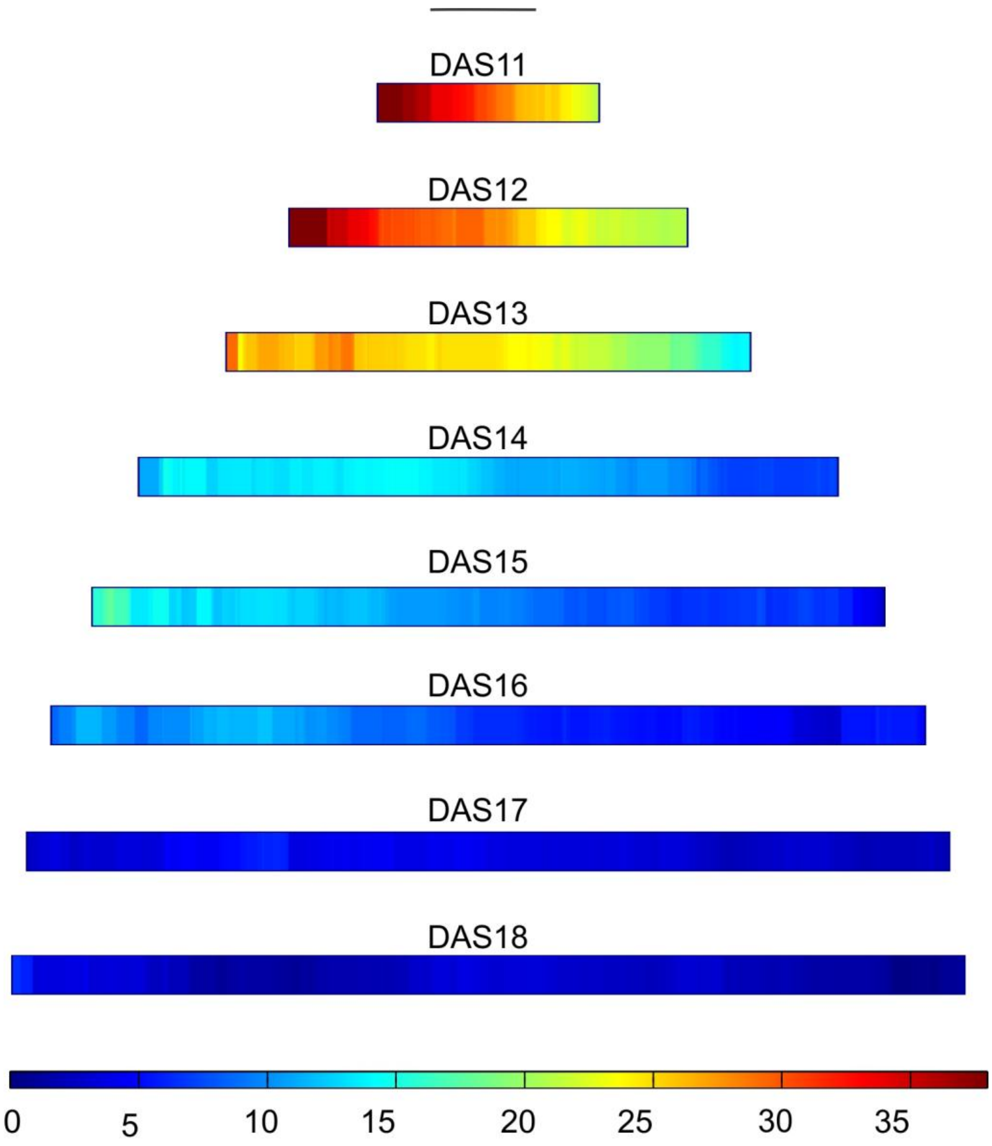

Figure 2.10: Mean midvein growth bars for DAS11-18.

The colours correspond to the relative increase in length per day in percent, according to the colour bar at the bottom. Each bar is scaled to the mean midvein length for that DAS, and oriented with the base at the left and tip at the right. The scale bar at the top represents 1mm. N=20.

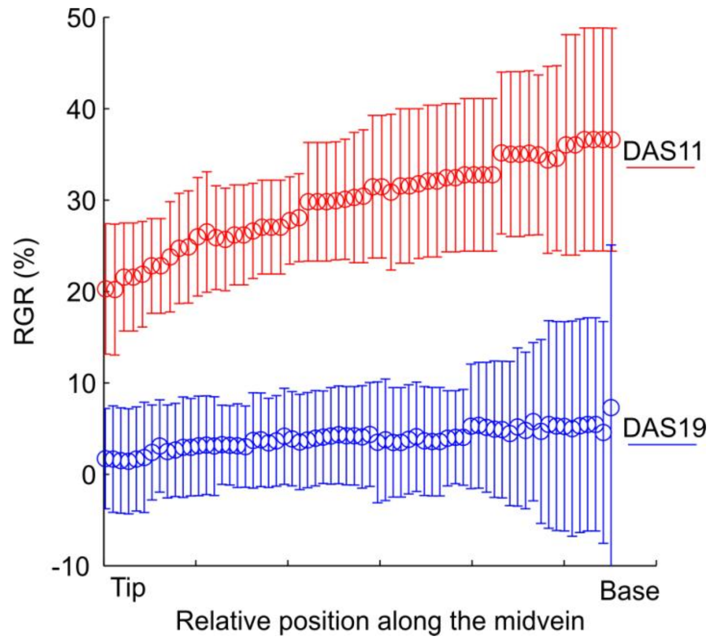

Figure 2.11: Mean ±SE of growth rates along the midvein.

Results are shown for DAS11 and DAS19 only for visual clarity. RGR is the % increase in length per day. N=20.

As growth rates along the midvein represent a linear measurement, as opposed to an areal measurement on the leaf surface, we would expect the relationship between the two measurements to be, approximately

areal surface growth rates $\cong$ (linear midvein growth rates)^2,

when growth is isotropic.

2.4.2 2D versus 3D growth measurements

Figure 17 shows a comparison of 2D and 3D measurements of the spatial maps of mean RGR for all time points. The differences between the 2D and 3D growth maps are almost imperceptible. The only discrepancy that exists is in a small region at the very base and sides of the leaf where 2D measurements tend to be slightly higher. This could be due to changing curvature of the leaf base over time – if the base region flattens out as it grows (a theory which results in Chapter 4 may support), the 2D calculations will see the flattening as additional growth. 2D and 3D growth anisotropy values are also very similar (Figure 2.13A), with anisotropy being highest at the edges and base of the leaf, and perhaps slightly higher along the midline, but quite low in most areas and declining over time. Neither 2D or 3D rotation maps showed any significant tissue rotation.

This demonstrates how the 2D approximation of the surface could be inaccurate for measurements in more highly curved leaves, but overall confirms that the 2D approximated calculations of growth as presented by Assaf et al. (in prep.) are accurate, and that this 2D method is appropriate in the case of *A. Thaliana* with a normal leaf phenotype, and thus probably other leaf species that are relatively flat.

2D and 3D growth direction values, on the other hand, are very different (Figure 2.13B). In 2D, the growth direction was found to be in the range of ±15° but close to 0° (i.e. horizontally oriented) at all regions, with no apparent spatial pattern. It would be surprising if growth was horizontally oriented, as one would expect this to cause the leaf to expand more in width than length, predominantly at the base (as this is where growth is most anisotropic), but we do not see this in the mean leaf shapes. 3D measurements show directions in the range of ±90, with a vague pattern detected at some time points: it seems that directions on the right side of the leaf have positive orientations, and vice versa, and that direction is more vertically oriented at the base and along the midline. Interestingly, the anisotropy and 3D direction maps look very similar to the vein loop elongation (Figure 2.13C) and orientation (Figure 2.13D) maps produced by R. Assaf et al. (in prep.), which may reflect the influence of growth on vein patterning.

Figure 2.12: Spatial maps of the mean relative growth rates (RGR) for the first rosette leaf of A. Thaliana.

The pair of maps shown for each DAS are the results of 2D (left) and 3D (right) measurements. RGR values are the relative areal increase as a percentage. The left pair of images (showing results for DAS11-14) are shown on a scale of 0-110% (as per the colour scale at the bottom left), and the right pair of images (showing results for DAS15-19) are shown on a scale of 0-30% (as per the colour scale at the bottom right). The means are based on data from 20 leaves, though sample coverage varies spatially. Maps are all scaled to the same arbitrary length.

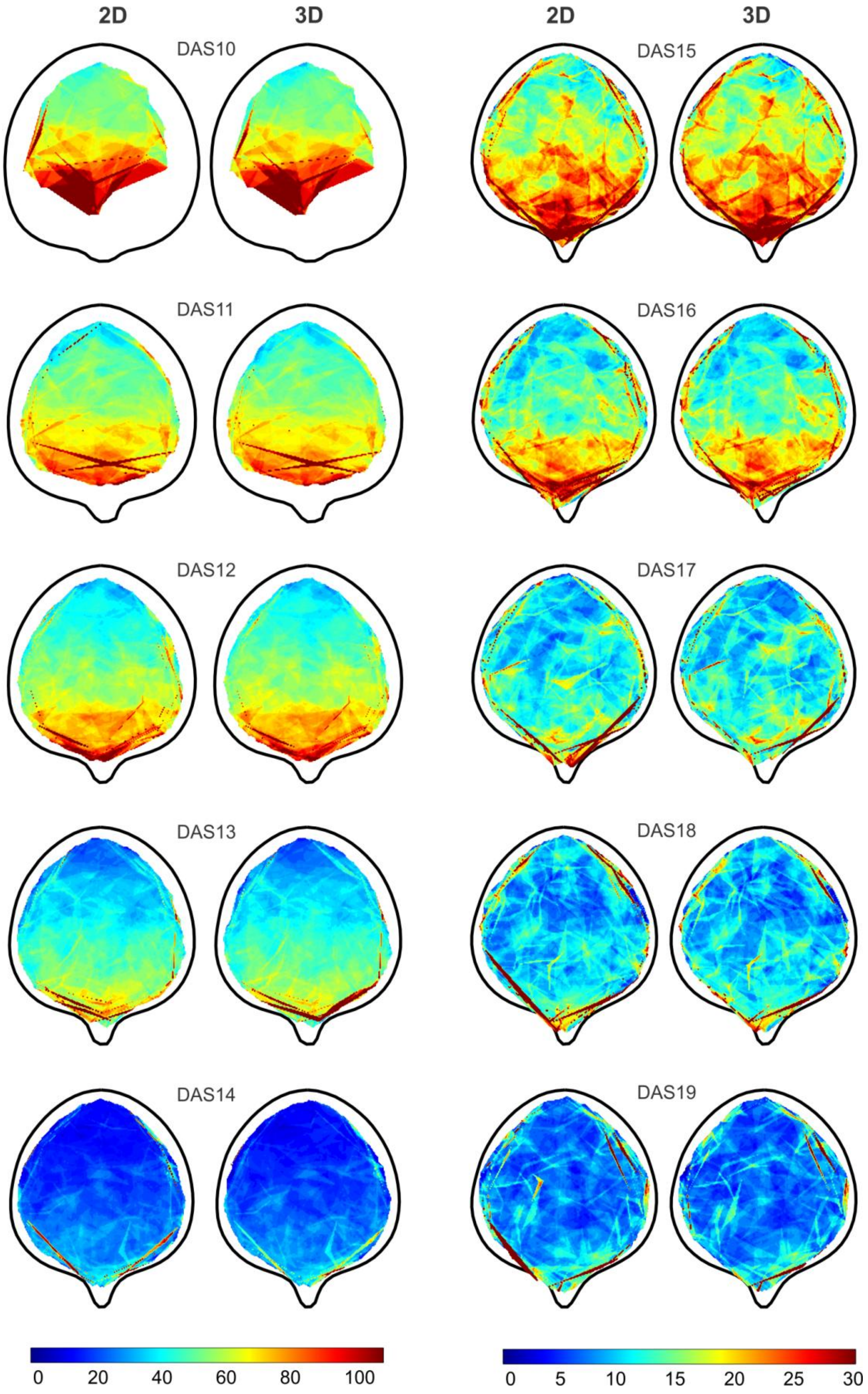

2D
3D
2D
3D
DAS10
DAS15
DAS11
DAS16
DAS12
DAS17
DAS13
DAS18
DAS14
DAS19
0
20
40
60
80
100
0
5
10
15
20
25
30

Figure 2.13: Spatial maps of directionality for the first rosette leaf of *A. Thaliana*.

(A-B) Mean anisotropy (A) and the mean direction of growth (B). The pair of maps shown for each DAS are the results of 2D (left) and 3D (right) measurements. Note that the 2D and 3D direction maps are shown on different colour scales, and that the angles are measured from 0˚ along the positive x-axis. Here we show DAS10-12 only as the similarities and differences between the two measurements become redundant, and anisotropy continues to decline to very low values.

(C-D) Mean length-width ratio of vascular loops (C) and mean vascular loop orientation (D) maps for the same data at DAS12, taken from R. Assaf et al. (in prep).

The means are based on data from 20 leaves, though sample coverage varies spatially. Maps are all scaled to the same arbitrary length.

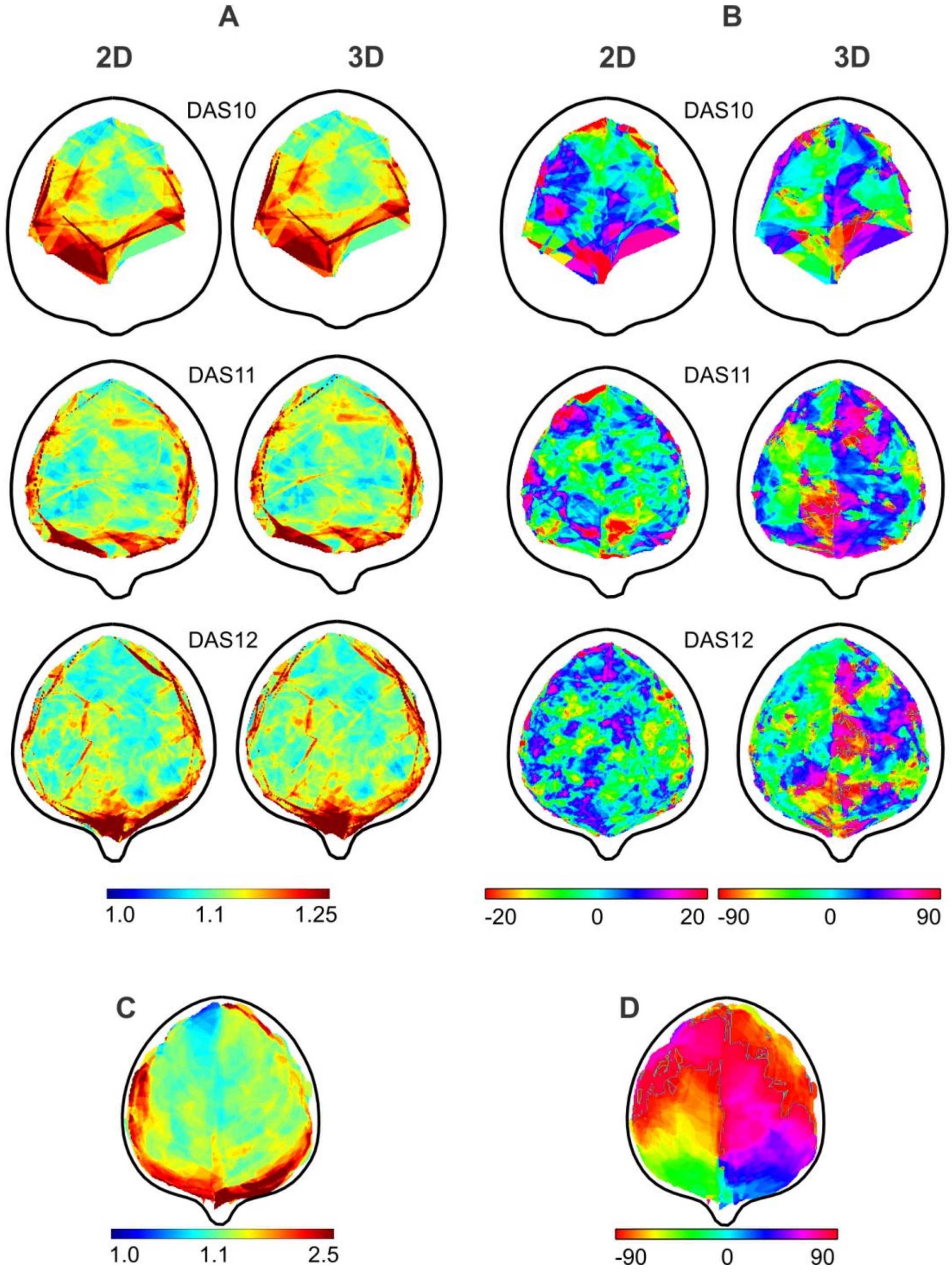
A
B
2D
3D
2D
3D
DAS10
DAS10
DAS11
DAS11
DAS12
DAS12
1.0
1.1
1.25
-20
0
20
-90
0
90
C
D
1.0
1.1
2.5
-90
0
90

2.4.3 Advantages and limitations

This method of quantifying growth from branching points of fluorescent-veined leaves provides several advantages over other methods: it allows for quantification of growth from early stages of development and now allows growth to be quantified from 3D coordinates, which means it can be applied to more complex leaf shapes. It also allows for concurrent quantification of vein patterning and growth from the same data (Assaf et al., in prep). Using vein branching points as landmarks is advantageous in most stages of development because new veins arise as the leaf grows, thereby maintaining a relatively constant density of integrated landmarks across the leaf.

There are some limitations in the use of vein branching points, however. In very early stages of development there are few branching points near the outer edges of the leaf, and none at the perimeter, so growth information can be collected only for the inner regions. This is particularly problematic for the study of leaves with altered morphology where the altered shape could be caused by changes in the shape of the gradient boundary, or growth rates around the perimeter, both of which would be difficult or impossible to measure with the current method. Spatial resolution is similarly limited by the lack of developed vasculature in early time points. The applicability of the method is also limited as it requires the use of a mutant line with fluorescent vasculature; the application of this method to study growth in mutant plants or other species is impeded by the necessity to first back-cross this feature into those plants.

2.4.4 Conclusions

Overall, we conclude that the method of calculating growth from 2D projections may be sufficiently accurate for computing growth rates and anisotropy in relatively flat leaves; however, there does seem to be a larger error in identifying the main direction of growth. We show that computing growth rates along the midvein may serve as a useful tool for assessing leaf proximodistal growth gradients.

In the following chapter we present a different approach to quantifying leaf growth with several advantages over the use of fluorescent vein branching points as landmarks, and we build upon the computational tools presented in this chapter to allow for more detailed analyses of growth patterns.

2.5 Supplemental material

2.5.1 Other improvements

We found that sometimes the mean maps contain a few triangular regions that have abnormally high or low growth values that are inconsistent with other values in the map. The triangular shape of these regions strongly suggested they arose from data from a single triangle. Further investigation revealed that this was indeed the case, and that the abnormally high or low growth rates of that triangle were due to very small and subjective discrepancies in the digitization of a point on a very narrow triangle. The growth rate of very narrow triangles can be dramatically affected by a small discrepancy in the digitization of a coordinate (as depicted in SFigure 2.1). To eliminate data prone to large errors it may be preferable to remove narrow triangles from the data set (either by removing data for that triangle, or cominbining it with an adjacent triangle to make one larger triangle).

Another possible improvement would be to automate the digitization of vascular branching points by employing software available from collaborators Mounsef and Karam (in prep). We may also be able to adapt tracking algorithms presented in the next chapter to semi-automate the tracking of branching points.

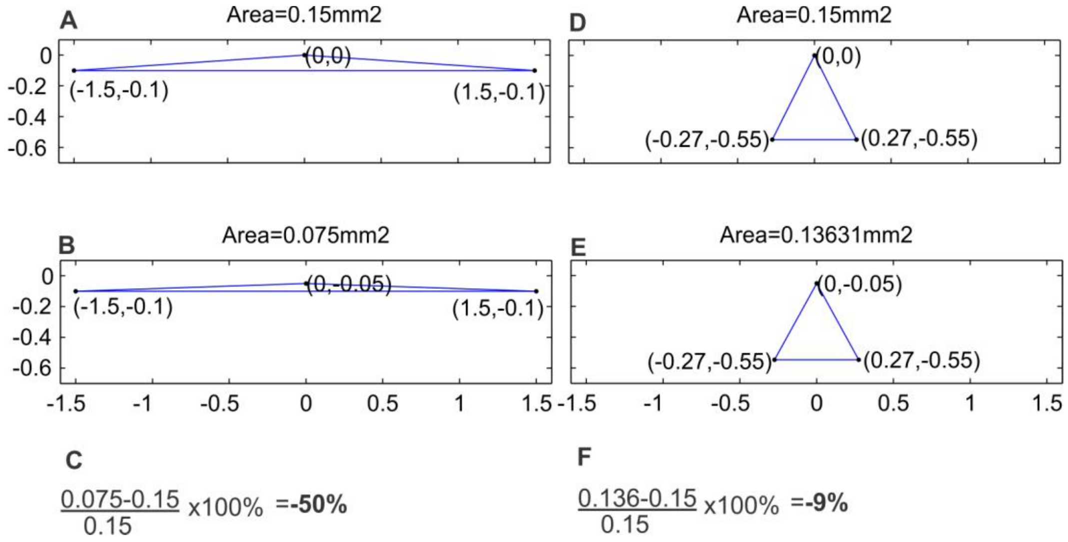

$$\frac{0.075-0.15}{0.15} \times 100\% = \mathbf{-50\%}$$

$$\frac{0.136-0.15}{0.15} \times 100\% = \mathbf{-9\%}$$

SFigure 2.1: Demonstrating how a small difference in a coordinate has a larger effect on narrow triangles.

(A and D) Digitized coordinates of two triangles at time *t*, one being very narrow (A), but both being of the same area.

(B and E) Digitized coordinates for the same triangles at *t+1.* Let us say that in reality the growth of the triangle should be zero and the coordinates should be exactly the same. However, in both cases the digitization was slightly off, and the y-coordinate of the top vertex was entered as y=-0.05 instead of 0.

(C and F) RGR calculations show that this discrepancy in the digitized position will make the narrow triangle in A-B appear to decrease in growth by 50% (as opposed to 0% as it should be in reality), while the triangle in D-E will appear to decrease in growth by 5%. Clearly a narrow triangle can be dramatically affected by a small error in the digitization of coordinates.

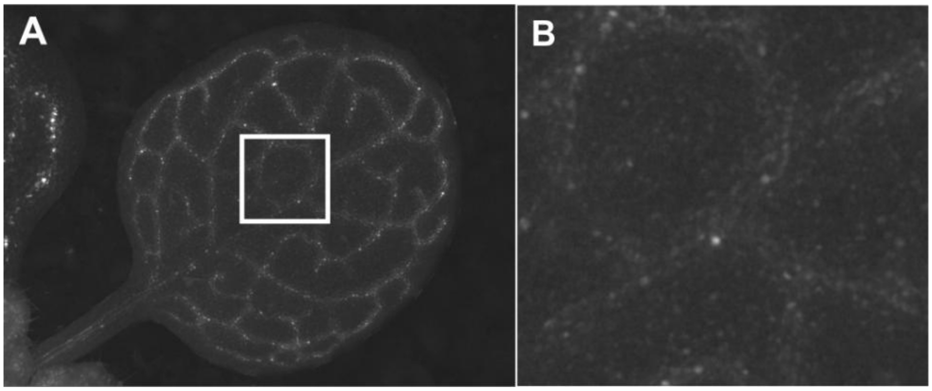

SFigure 2.2: Patchy fluorescence can make it difficult to digitize midvein branching points with high precision.

(A) A typical multifocus leaf image

(B) Magnified region in box of A, showing vein intersections at the midvein

Chapter 3: Quantifying growth patterns at the leaf surface in three dimensions

3.1 Abstract

Growth patterns vary in space and time as an organ develops, leading to shape and size changes. Quantifying organ growth in space throughout development is therefore crucial to understand how organ shape is controlled. We present a novel method and computational tools to quantify spatial patterns of growth from three-dimensional data at the adaxial surface of leaves, by semi-automatically tracking microscopic fluorescent particles applied to the leaf surface. Results from multiple leaf samples are combined to generate mean maps of various growth descriptors, including growth rates, directionality, and anisotropy. The method was applied to the first rosette leaf of *Arabidopsis thaliana*, and revealed clear spatiotemporal patterns in growth, which can be interpreted in terms of gradients in morphogen concentrations. The three-dimensional capability of the method presented makes it applicable to young leaves as they first emerge and to mutants or species with non-flat leaves. The semi-automated tools make a high throughput of data possible, and the algorithms for generating mean maps of growth will make it possible to perform standardized comparative analyses of growth patterns between wild type and mutants and/or between species. The method and software presented can therefore be useful in investigating the mechanisms of leaf morphogenesis.

3.2 Introduction

The highly regulated organization of tissues into functional shapes during morphogenesis is a crucial and intriguing process (Coen et al., 2004; Tsukaya, 2006; Strutt, 2005). The development of organ shape is driven by spatial and temporal variations in growth parameters – such as the rate and directionality of tissue expansion, and tissue rotation (see Coen et al., 2004 for review). Characterizing these growth parameters, at a sufficient spatial and temporal resolution, would be instrumental in uncovering the mechanisms responsible for the generation of organ shapes.

Leaves are a good system in which to study the process of morphogenesis, given their relatively thin structure that can be approximated as a three-dimensional (3D) surface, visual accessibility, and absence of cell migration (Cosgrove, 2005). Early efforts to measure growth across the leaf involved drawing ink dots on the leaf surface to delineate a grid of small rectangles whose deformations over time could be used to calculate regional growth rates (Avery, 1933; Richards and Kavanagh, 1943). Other studies since then have employed the same concept of quantifying growth at the leaf surface by tracking ink marks (Poethig and Sussex, 1985; Granier and Tardieu, 1998; Wang et al., 2011; Saurer and Possingham, 1970; Maksymowych, 1962), or vein intersections (Wolf et al., 1986; Walter and Schurr, 1999; Walter et al., 2003; Taylor et al., 2003; Erickson, 1966; Maksymowych, 1959). Recently, digital image sequence analysis tools have been developed to automatically track the displacement of identifiable features in successive images of a leaf (Schmundt et al., 1998; Ainsworth et al., 2005; Wiese et al., 2007).

One important limitation of existing tracking methods is that they cannot be used to study early stages of leaf development in which major growth and developmental processes occur. This is because drawing or printing ink dots on the leaf surface (Avery, 1933; Richards and Kavanagh, 1943; Poethig and Sussex, 1985; Granier and Tardieu, 1998; Wang et al., 2011; Maksymowych, 1962) or threading or clipping weights through the leaf margins as required for the digital image sequence analysis setup (Schmundt et al., 1998; Ainsworth et al., 2005; Wiese et al., 2007) require that the leaf be relatively large, and vascular features (Wolf et al., 1986; Walter and Schurr, 1999; Walter et al., 2003; Taylor et al., 2003; Erickson, 1966; Maksymowych, 1959) are not visible at early stages of development.

Another significant limitation of existing methods and computations is that they are only applicable to flat or flattened leaves. In the past decade there has been increased interest in more geometrically complex leaf shapes, such as such those with stronger curvatures, rolling, ruffling, wrinkling, and twisting, but, as many researchers have pointed out, methods to study the growth of such three-dimensional surfaces are not presently available (Tsukaya, 2006; Piazza et al., 2005; Cronk, 2009; Walter et al., 2009; Micol, 2009).

Finally, previous leaf growth studies have not been able to produce average leaf growth information at high spatial resolution. Even within leaves of the same genotype at the same developmental stage, there is variation in leaf size and growth, so in order to make quantitative comparisons of leaf growth between mutant and wild type plants, plants grown in different environmental conditions, or plants of different ecotypes, for example, it would be very useful to have a method for producing mean spatial maps of growth parameters from a number of samples.

Here, we present a novel technique and computational tools that allow for a detailed analysis of spatial growth patterns at the surface of a leaf in 3D from an early stage of development. The computational tools involve semi-automated image analysis and point-tracking algorithms, as well as programs for averaging results of several samples to compute and display average leaf shapes and spatial maps of mean growth pattern parameters. The technique may be applied to characterize growth in other organs and organisms. The algorithms we developed are available upon request.

3.3 Results

In this study we monitor the growth of the first rosette leaf in 35 *Arabidopsis thaliana* plants from 7 to 19 days after sowing (DAS). More information on the data set can be found in Supplemental Materials and Methods and SFigure 3.1A in the Supplemental Information. In the following we first present the results of the data acquisition and computational methodology, and then describe the growth parameter data obtained.

3.3.1 Using fluorescent particles as landmarks to track leaf growth

To track growth, fluorescent microparticles are applied topically to the surface of the leaves. Particles are applied as soon as the leaf surface is exposed, typically at 7 days after sowing (“DAS7”) when the leaves are as small as 500 micrometers in length. The application method is gentle, non-invasive, and does not disturb leaf development (see SFigure 3.1B). The particles settle onto the leaf cuticle and move with the leaf surface as it grows (refer to SFigure 3.1C), so leaf growth can be quantified by tracking particle divergence.

Figure 3.1: Acquiring and extracting data.

(A-D) LeicaTM LAS Montage Module images generated from z-stack images of a leaf. We use the brightfield z-stack to obtain a multifocus montage (A), a depth map (B), and a confidence map for the depth map (C). We use the fluorescence z-stack to obtain a multifocus montage image of the fluorescent particles on the leaf (D). In (D), the image was enhanced to improve visibility of the particles in the publication-sized figure, the leaf outline is plotted for clarity, and the yellow rectangle indicates the region magnified in E and F. The scale bar in (A) indicates 1mm.

(E and F) Illustration of the particle digitization algorithm. We show a zoomed-in region of the fluorescence montage image (E). The algorithm applies a k-means clustering function which sorts the pixel values into four groups: typically, the dark parts of the image (dark blue), the very faintly glowing areas around the particles (light blue), the brighter glowing areas around the particles (yellow), and finally the brightest parts of the image, the fluorescent particles (red) (F). x, y coordinates of particles, shown as green dots, are defined as the centroid of clusters of the brightest pixels (F).

(G) Digital reconstruction of the leaf surface and particles in 3D after extracting z-coordinates from the depth map. Axes units are in µm.

(H and I) Illustration of the pattern matching algorithm. We show the particles on a leaf at two successive time points, DAS10 (H) and DAS11 (I). The insets show the fluorescent montage images (rotated so that the leaves are oriented vertically) and the yellow rectangles indicate the areas shown on the main panels. The neighbour patterns of four particles are shown, with the green arrows illustrating the neighbour distances and orientation (measured relative to the axis in blue). Matches between the two time points, indicated by the numbering, are identified by the program based on these unique neighbour patterns. See SFigure 3.1 for more information.

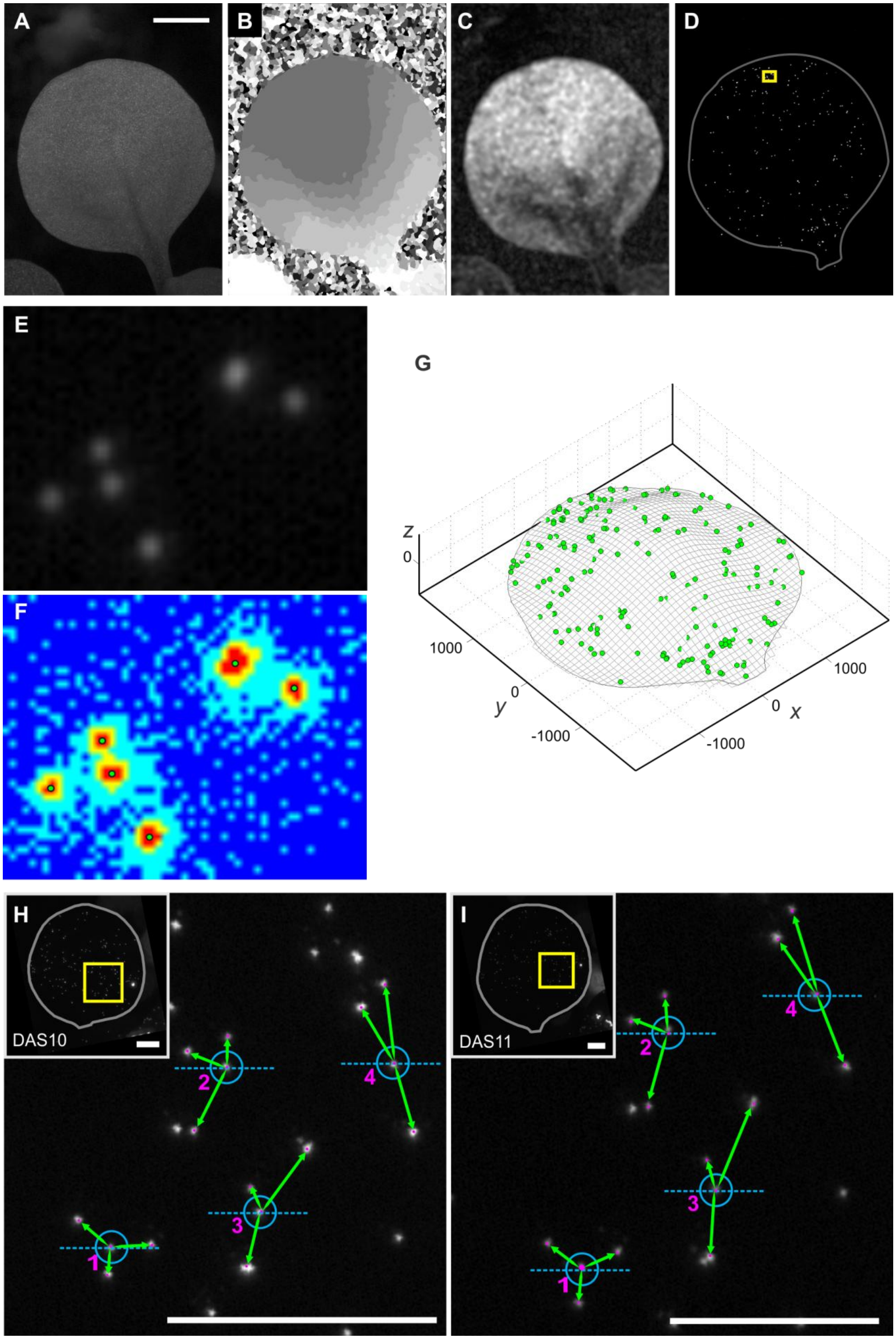
A
B
C
D
E
F
G
z
0
1000
0
y
-1000
1000
0
x
-1000
H
DAS10
1
2
3
4
I
DAS11
1
2
3
4

3.3.2 Imaging the leaf and fluorescent particles

Each leaf is imaged every 24 hours with a motorized fluorescence macroscope (see Materials and Methods for details). We first acquire a z-stack (a series of images at different focal planes) of a leaf under reflected brightfield lighting, and then a second stack under fluorescence. The microscopy software saves details such as the vertical step size between focal planes in the z-stack and the resolution of the image in .xml files. The brightfield stack is used to obtain a multi-focus montage image of the leaf (Figure 3.1A), a depth map of the leaf surface (Figure 3.1B), and a confidence map of the depth map computations (Figure 3.1C). The fluorescence stack is used to produce a multi-focus image of the fluorescent particles (Figure 3.1D). All computational steps that follow are performed using our custom-made software developed in Matlab (see Materials and Methods).

3.3.3 Extracting the 3D leaf shape

The 2D projection of the leaf outline is obtained by digitally tracing it from the brightfield multifocus leaf image. The 3D outline and topography of the leaf are then extracted from the depth map. The 3D leaf surface is recorded as a mesh fitted over the area enclosed by the leaf outline, using the depth map to determine the z-coordinates of each point on the grid. The leaf coordinates are then centered and aligned as explained in Chapter 2.

3.3.4 Digitizing particles semi-automatically

A k-means clustering function (Seber, 2008) is applied to the multifocus fluorescence image (Figure 3.1E-F) to automatically identify which pixels in the image are bright enough to be considered the fluorescence of a particle. Particle *x, y* coordinates are identified as the centroid of interconnected bright pixels. Depending on the quality of the image and distribution of particles, this will typically identify 80-100% of the particles. Any bead missed by the algorithm can be manually added by the user. The z-coordinates of the particles are retrieved from the vertical height of the 3D leaf surface at each particle's *x, y* position. Figure 3.1G shows an extracted leaf surface and its associated particles in 3D.

3.3.5 *Semi-automatic particle tracking*

Digital image sequence analysis software (Bernd, 1997) is not applicable to particle tracking in our study due to the large displacement of particles between successive images. To make our procedure capable of high-throughput, we developed a set of programs for semi-automatic tracking of points with large displacements due to growth deformations. This involves two algorithms. A pattern recognition algorithm first identifies a particle at successive time points based on the relative position of its neighbouring particles, as illustrated in Figure 3.1H-I. The pattern recognition algorithm typically matches 80-100% of the particles. These initial matches are then used by a warping and matching algorithm to estimate the tissue deformation between time points and thereby identify any remaining particles based on their relative position on the leaf. Matches need to be verified by the user, and in cases where matching is not successful, the default parameters of the matching programs can be adjusted by the user. Further details of both algorithms are provided in Supplemental Materials and Methods.

3.3.6 *Computing growth strains in 3D*

To subdivide the surface into small regions that can be tracked over time, we apply a Delaunay triangulation function to connect all of the particle coordinates on the leaf to each other through non-intersecting triangles, using the same triangulation on matched particles over successive time points. Now, instead of tracking the movement of particles *per se*, we are tracking the changes in size, shape, and orientation of triangular regions over time. Using singular value decomposition (SVD) formulas, as explained by Goodall and Green (1986), we are able to compute a variety of growth parameters. SVD allows us to calculate, for each triangle, the direction of maximal growth, the rotation, and the scaling factors p and q. p is the scaling factor along the main direction of growth, and q is the scaling factor along the minimal direction of growth, which by the laws of mechanics is oriented orthogonally to the maximal direction of growth. We compute the relative growth rate (RGR) for each triangle as the percent increase in area over the course of a day (24h):

$$RGR(t) = \frac{A(t+1) - A(t)}{A(t)} \times \frac{1}{\Delta t} \times 100\% = (p \times q) \times 100\%$$

where *RGR(t)* is the percentage increase in area from day *t* to day *t+1*, *A(t)* is the area of the triangle at day t, *A(t+1)* is the area of the triangle at day *t+1*, and *p* and *q* are the scaling factors along the maximal and minimal directions of growth over the course of one day.

Growth anisotropy, a measure of how preferentially growth occurs along the maximal directional growth, is computed from the ratio of the scaling factors (*p/q*). An anisotropy value of 1 indicates that growth is occurring evenly in all directions, and higher values indicate that growth occurs predominantly along a main direction.

The SVD calculations are not directly applicable to 3D landmarks. To compute growth strain parameters from 3D coordinates, we apply the flattening algorithm explained in Chapter 2 to first rotate the triangle coordinates onto a 2D plane, compute growth using SVD, and then reorient the results in the true 3D position by applying the inverse of the flattening rotations.

To display a given growth parameter from one time point to the next, we plot the parameter value of each triangular region on the first of the two time points using a colour map. For instance, to display leaf RGR from DAS10 to DAS11, we plot the RGR values on the DAS10 leaf. An example of a map of relative growth rates of one leaf over time is shown in Figure 3.2A. These results can be plotted and viewed in 3D, as shown in SVideo 2.

3.3.7 Making mean spatial growth maps

Because growth rates may vary between samples, we track the growth of the first leaf in several plants, and generate mean maps for each time point, by averaging the growth parameters of all samples at each 2D position of the mean map, using adaptations of programs developed by Rolland-Lagan et al. (2009). See Chapter 2 for more details.

We also compute maps of variance. For growth and anisotropy we calculate the relative standard error (RSE)

$$RSE = \frac{SE}{\overline{X}} \times 100\% = \frac{s}{\sqrt{n}} \times \frac{1}{\overline{X}} \times 100\%$$

where SE is the standard error, *s* is the standard deviation (computed with Matlab's *nanstd* function), *n* is the number of samples with data, and $\overline{X}$ is the mean, at that position on the mean leaf. We chose to display relative standard (RSE) for assessing the variance of our data due to the fact that growth rates and anisotropy vary spatially and temporally, which makes it difficult to analyze and compare the more commonly used SE values. E.g. an RGR SE of 25% at a position where the mean RGR is 200% has a different implication than an SE of 25% at a position where the mean RGR is 10%.

To illustrate the result of combining data from multiple samples, in Figure 3.2B we show the mean RGR spatial maps for the same time points (DAS7-11) and on the same size and colour scale as that of the RGR maps shown for the individual leaf sample in Figure 3.2A. Spatial averages of the scaling factors, RGR, anisotropy, and associated standard errors of the means are displayed as surface colour maps on the mean leaf shape, and angles of the direction of growth and rotation of tissue are displayed as lines, with the orientation of a line indicating the direction of growth or rotation. The number of samples used in the mean maps calculations varies in space and time (SFigure 3.2A), most areas and most time points having 12-15 samples. We only display average values on the surface maps for locations where the number of samples is greater than three.

3.3.8 Growth rates follow a tip to base gradient and decrease over time

In Figure 3.2C we show the mean maps of RGR for all of the time points analyzed. Temporally we see that the growth rates decrease over the course of development and that the changes in the mean leaf size accordingly become much smaller in later time points. To further evaluate temporal changes in leaf growth, we took the average of all the values in the top and bottom quarter of the mean spatial maps for each DAS and plotted them over time (Figure 3.3). Overall, growth appears to be declining at an exponential rate, and the decline in RGR at the leaf base is much higher than the decline in RGR at the leaf tip in earlier time points, with the difference in growth rates between leaf base and leaf tip decreasing over time.

Since the leaf size and range of growth rates change drastically over time, in Figure 3.4 we separate the growth maps into groups of 3 (DAS7 to 9, 9 to 11, 11 to 13, 13 to 15 and 15 to 18) and show growth rates for each group using a different colour scale. This shows a clear proximodistal growth gradient, with rates highest at the base and lowest at the tip for all time points. To better assess and describe the proximodistal growth gradient, we take a strip of values along the midrib of the mean RGR maps, and plot the average of the values in that strip at each position along the leaf proximodistal axis (Figure 3.5A). This shows that the slope of the growth gradient decreases significantly over time.

The scaling factors in the direction of maximal and minimal growth, *p* (Figure 3.6A) and *q* (Figure 3.6B) respectively, both follow the same trend as RGR, with the rates decreasing over time and decreasing from base to tip. *p* and *q* also decline faster at early time points, and decline by a greater amount at the base than at the tip over the course of development (SFigure 3.3A-B). The proximodistal gradients of *p* and *q* are slightly different, as *p* follows an exponential decline from base to tip (Figure 3.5B), while *q* declines more linearly (Figure 3.5C).

3.3.9 *The shape of the RGR gradient front is initially downward-curving but becomes straighter over time, and differs between p and q*

The shape of the RGR gradient front has a downward curving shape for DAS7 through to DAS10, and then in DAS11-13 appears to take on a straighter and even slightly upward curving front. From DAS13 onwards the gradient still exists but the shape of the gradient front becomes much less distinctive. The relative standard error (RSE) of the mean RGR (SFigure 3.2B) is generally higher in those later time points, ranging from 1 to 10%

for DAS7-11 and from 10 to 30% for DAS 12-18, except for areas around the leaf perimeter where the RSE is high due to lower sample coverage.

To better assess our observations about the shape of the RGR gradient front, we take a section along the width of the mean maps and plot the average of the values at each transverse position in that strip as a function of the position along the leaf transverse axis (Figure 3.5D). Here we can clearly see that the RGR gradient is downward-curving for DAS7-10, with rates highest at the middle of the leaf and lowest at the sides. At later time points it seems to be the opposite, although the difference between rates at the middle and sides of the leaf is very small. We carry out the same assessment for the maps of p and q, and find that they do not have the same gradient shape as each other. For p, the gradient appears to be very slightly downward-curving from DAS7-9 and slightly upward-curving from DAS13 onward (Figure 3.5E). The difference in q between the middle and sides of the leaf on the other hand is much more dramatic and shows a very strong downward curvature for DAS7-11 with rates at the middle being up to approximately 15% higher than the sides. From then on the gradient shape of q appears to be relatively straight (Figure 3.5F). These observed gradient shapes are statistically significant (see Table S1 and SFigure 3.3C-D).

Another interesting pattern is seen in spatial maps of q (Figure 3.6B), but not p, for DAS11-14. We see lower rates along the middle of the leaf, corresponding to the position of the midvein, and particularly in DAS13 we also see two “branches” of lower rates extending out fairly symmetrically from the midvein at about 45°.

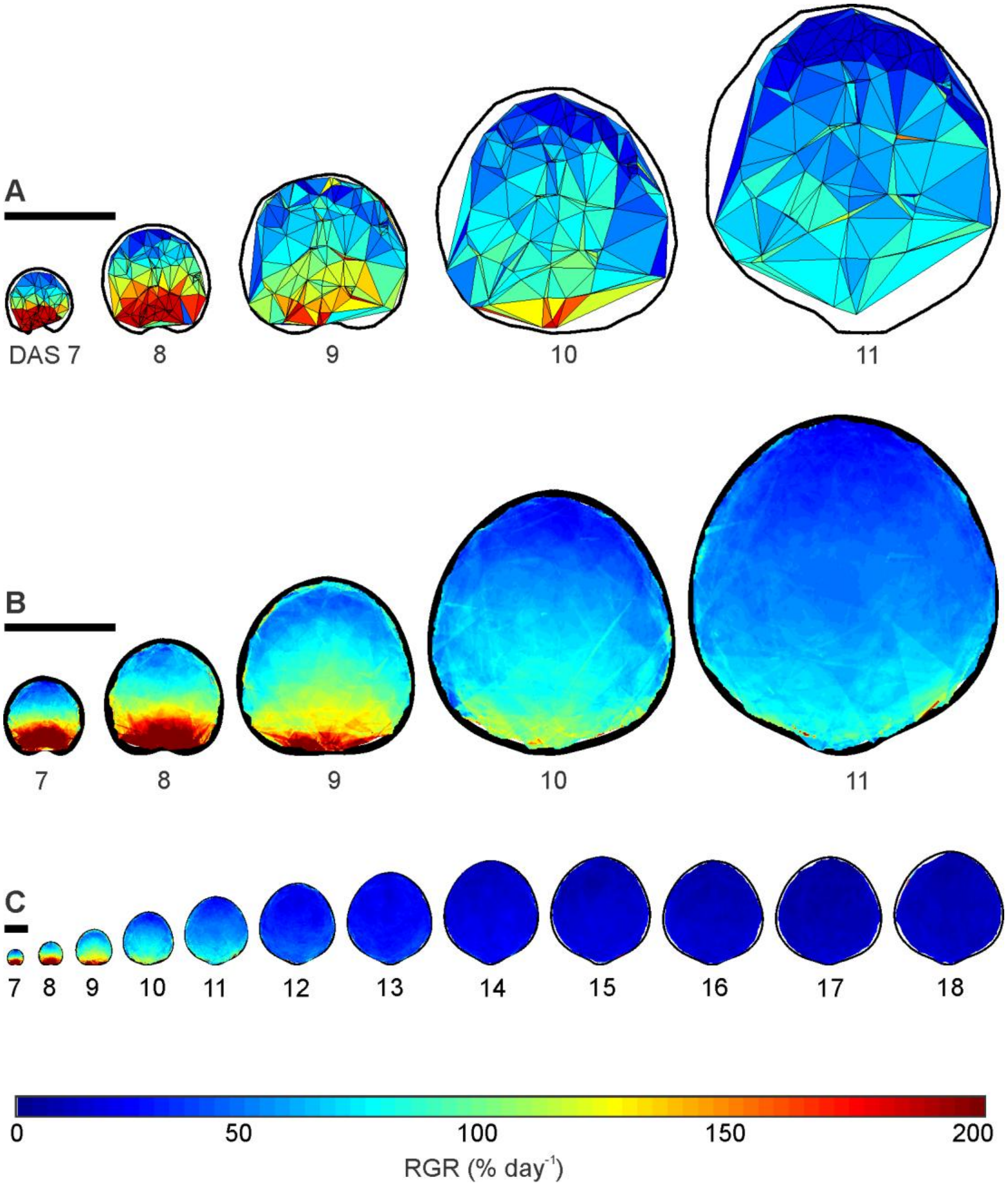

Figure 3.2: Spatial maps of relative growth rates over time.

(A) Spatial maps of RGR for one leaf for DAS7-11. The colour of each triangle indicates the percent increase in area per day (RGR day-1), according to the colour scale below.

(B) Mean spatial maps of RGR for DAS7-11 based on the average of 12-23 samples per time point.

(C) Mean spatial maps of RGR for all time points quantified in this study, DAS7-18. Scale bars indicate 1mm. See SFigure 3.2 for more information.

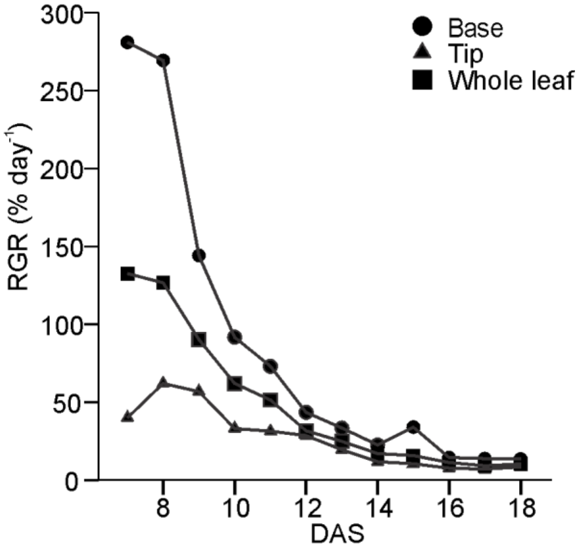

Figure 3.3: Relative growth rates of the whole leaf and leaf base and tip over time.

The values for the whole leaf are computed from the average of all the values across the mean spatial map of RGR. The values for the leaf base and tip are computed from an average of the bottom and top quarter of the mean RGR spatial map, respectively.

Figure 3.4: Mean spatial maps of RGR for DAS7-18.

Groups of time points are shown on different colour scales.RGR (% increase in area per day) values are indicated by the colour according to the colour scales shown on the right. The time points are divided into groups of 3 (with each group overlapping by one DAS), each shown on a different line on a different colour scale (right) so that the spatial and temporal patterns can be seen clearly. Scale bars on the left indicate 1mm.

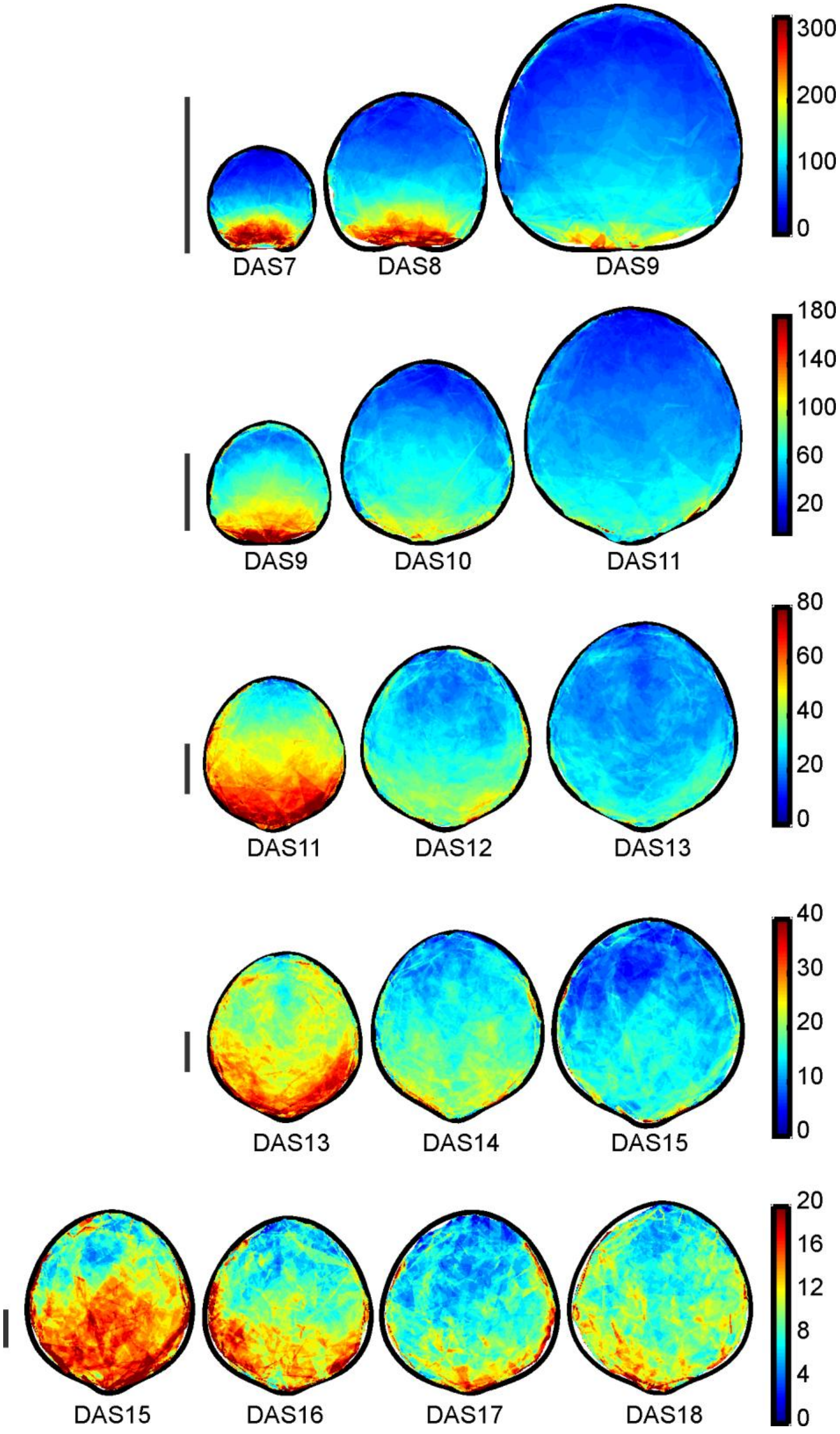
DAS7
DAS8
DAS9
300
200
100
0
DAS9
DAS10
DAS11
180
140
100
60
20
DAS11
DAS12
DAS13
80
60
40
20
0
DAS13
DAS14
DAS15
40
30
20
10
0
DAS15
DAS16
DAS17
DAS18
20
16
12
8
4
0

Figure 3.5: Proximodistal and transverse patterns of growth parameters.

(A-C) Proximodistal gradient of RGR (A), p (B), and q (C). As illustrated in the diagram below the graphs, we take a strip of values along the midline of the mean spatial maps (in grey), and plot the average of the values in that strip at each position along the leaf proximodistal axis (i.e. averaging occurs along the direction of the black lines within the grey strip).

(E-F) Transverse gradient shapes of RGR (D), p (E), and q (F). As illustrated in the diagram below the graphs, we take a strip of values across the width of the mean spatial maps (in grey), and plot the average of the values in that strip at each position along the leaf transverse axis (i.e. averaging occurs along the direction of the black lines within the grey strip).

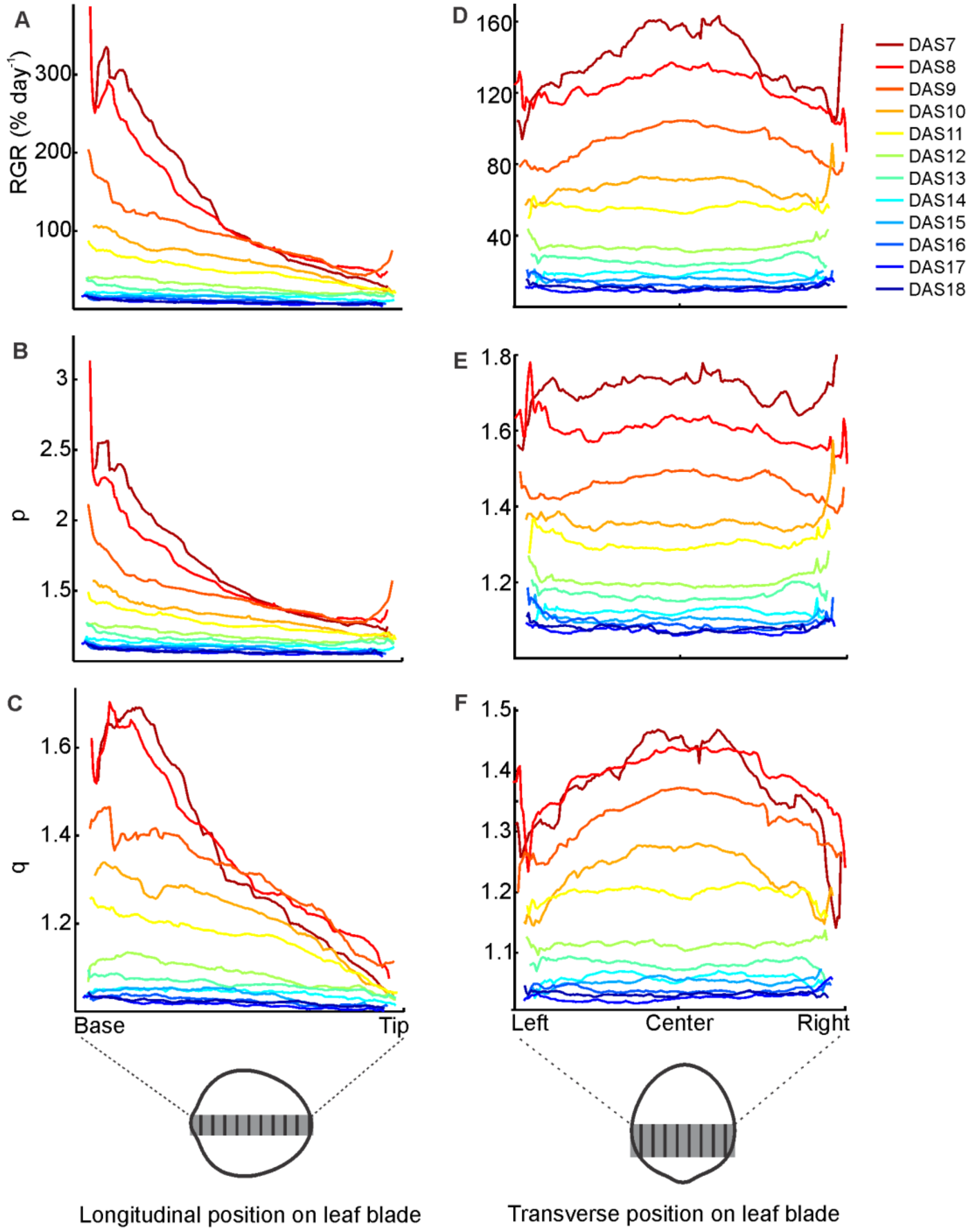
A
RGR (% day^{-1})
300
200
100
B
p
3
2.5
2
1.5
C
q
1.6
1.4
1.2
Base
Tip
Longitudinal position on leaf blade
D
160
120
80
40
E
1.8
1.6
1.4
1.2
F
1.5
1.4
1.3
1.2
1.1
Left
Center
Right
Transverse position on leaf blade
DAS7
DAS8
DAS9
DAS10
DAS11
DAS12
DAS13
DAS14
DAS15
DAS16
DAS17
DAS18

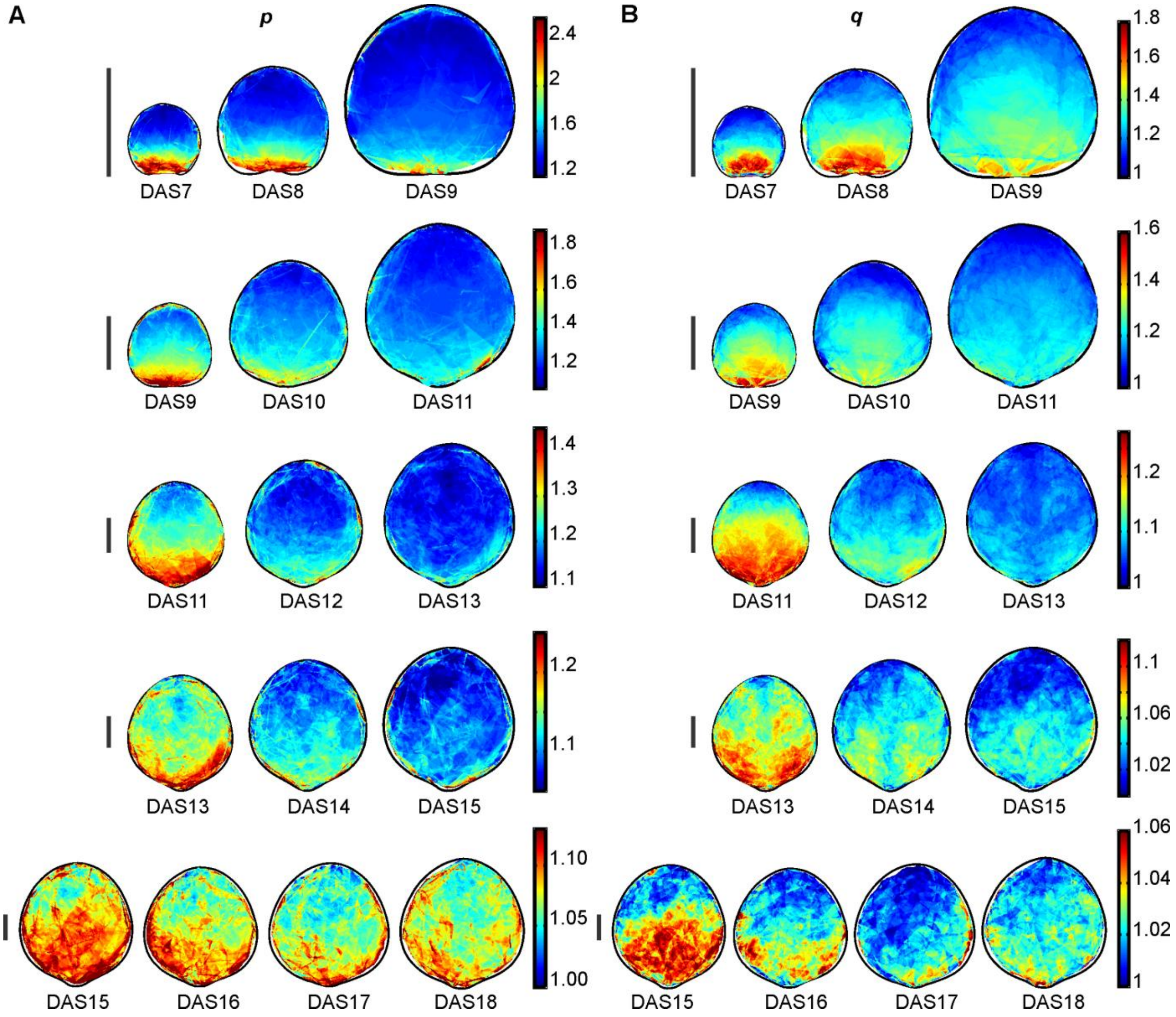

Figure 3.6: Mean spatial maps of scaling factors along the maximal and minimal directions of growth, respectively.

Colour scales indicate the scaling factor along the maximal (A) or minimal (B) direction of growth over the course of a one day interval. The time points are divided into groups of 3-4 days (with each group overlapping the previous group by one day), each shown on a different line on a different colour scale (right) so that the spatial and temporal patterns can be seen clearly. The maps are scaled to the relative mean leaf sizes for each DAS, with the scale bars on the left indicating the length of 1mm. See SFigure 3.3 for more information.

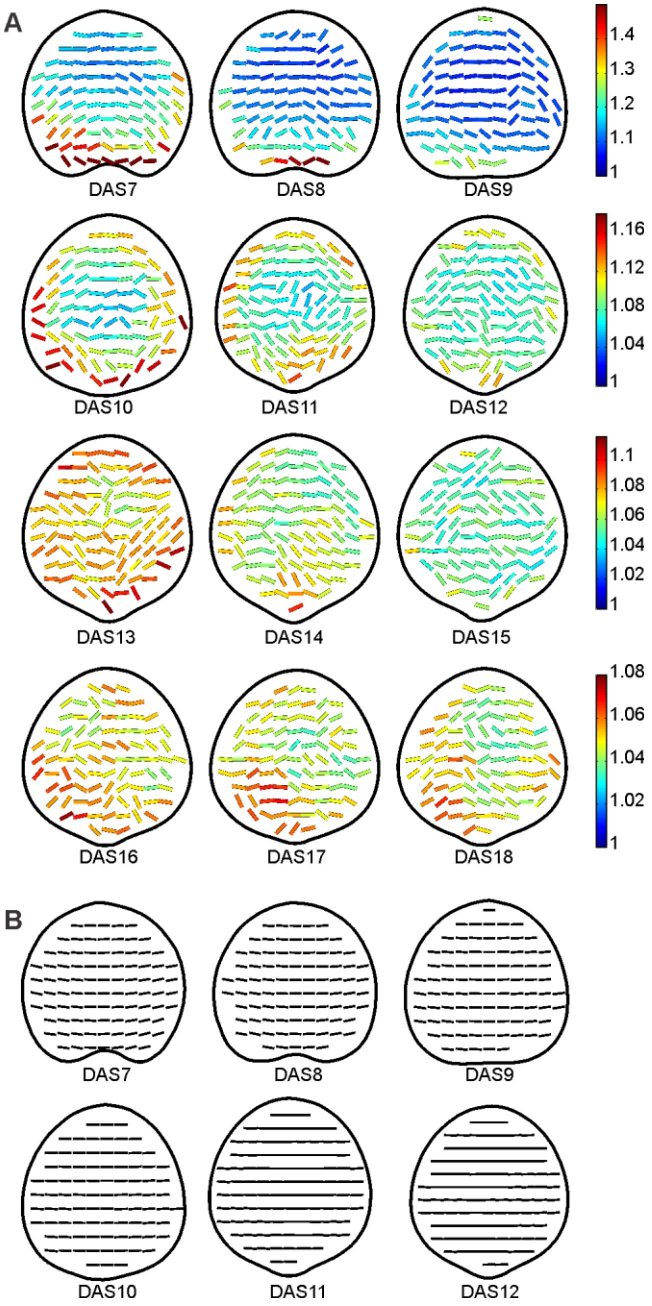

Figure 3.7: Mean spatial maps of growth directionality and tissue rotation.

(A) Mean spatial maps of anisotropy and main growth direction for DAS7 to DAS18. The orientation of each line represents the direction of maximal growth at that point and the colour of the line indicates the growth anisotropy (*p/q*) as per the colour scales on the right.

(B) Mean spatial maps of tissue rotation for DAS7-12. The orientation of the lines represents the rotation of the tissue measured from the positive x-axis, with horizontal lines corresponding to no rotation (0 degrees). See SFigure 3.4 for more information.

3.3.10 Anisotropy is strongest at the leaf base and leaf perimeter and decreases over time

Figure 3.7A shows spatial maps of the angles of the maximal direction of growth, coloured according to anisotropy.

Like growth rates, growth anisotropy values also decrease over time. Spatially, growth anisotropy appears to follow a gradient where the values are highest at the base and perimeter of the leaf. However the base and perimeter also correspond to the areas with higher relative standard errors (up to 15%) in the earlier time points (SFigure 3.4A). This gradient becomes less distinctive after DAS12, while the relative standard error of anisotropy is very low, generally under 2%.

3.3.11 The main direction of growth varies in space

The maximal direction of growth seems to follow a gradient where it is fairly horizontal in central regions of the leaf, and bends in outer regions to be more in line with the angle of the nearest leaf margin, with the exception of areas where the leaf margin is parallel to the proximodistal axis of the leaf, in which case the angle of principal direction is oriented perpendicularly to the leaf margin. Another exception to this rule appears to exist from DAS11-14 where the main direction of growth along the midline of the leaf seems to align more closely with the proximodistal axis of the leaf. At DAS13, the main direction of growth is also aligned along two branches extending at about 45 degrees on each side of the leaf midline. In order to assess the variability in growth directions at each point of the leaf, we can calculate circular variance. Circular variance provides a measure of the spread of angles, ranging from 0 to 1, with values close to 0 indicating a tighter clustering of the values around the mean (Zar, 1996). The circular variance of the mean growth directions is fairly high (SFigure 3.4B), with most values in the range of 0.2-0.8 at DAS7, 0.4-0.8 at DAS8-9, and 0.6-0.8 in the remaining time points.

3.3.12 Tissue rotates upward at the outer edges of the leaf by an angle that decreases over time

Mean spatial maps of the rotation of tissue are shown in Figure 3.7B. Tissue at the leaf tip and along the center does not rotate, while tissue on the left rotates slightly clockwise and tissue on the right rotates slightly counter-clockwise. The amount of rotation decreases over time, with rotation of up to ±15° at DAS7, ±12° at DAS8, and ±10° at DAS9. In later time points the angles of rotation become very small. The circular variance of the rotation angles is very low (mostly in the range of 0-0.05) for all time points (SFigure 3.4C).

3.4 Discussion

In this paper we have presented a novel technique for quantifying leaf growth patterns in vivo over several days without disturbance to the plant. Growth can be followed from a much earlier stage of development than has previously been possible, and various growth parameters can be computed from 3D coordinates of landmarks. Leaf growth phenotypes can be quantified relatively quickly using several semi-automated custom computational tools, and mean spatial growth maps can be generated to analyze and compare the average leaf growth patterns of several groups of plants. In the following we discuss our results on leaf growth patterns, as well as the method itself.

3.4.1 Changes in the growth gradient shape over time support the existence of a growth promoting morphogen originating at the leaf base and a growth inhibiting morphogen originating at the leaf tip

Our results showed that the relative growth rates across the leaf decrease over time, and have a very distinct proximodistal gradient with rates highest at the base and lowest at the tip. In early time points, this growth gradient has a very clear downward-curving pattern. This suggests that the signal that gives rise to the gradient is a growth promoting/maintaining morphogen originating from the leaf base. At approximately DAS11, the shape of the gradient becomes straighter or even upward curving. This change in gradient shape over time may reflect interplay between a growth promoting morphogen originating from the leaf base from early time points onwards and a growth inhibiting signal originating from the leaf tip at later time points. Interestingly, the *KLUH* gene has been shown to be expressed at the leaf base during early development, and was proposed to generate a proximodistal concentration gradient of a mobile growth factor in the leaf (Kazama et al., 2010; Anastasiou et al., 2007a). On the other hand, the cell division patterns in leaves of the snapdragon (*Antirrhinum*) *cincinnata* mutant support the existence of a growth repressing signal originating from the leaf tip (Nath et al., 2003).

The shape of the growth gradient can affect the 3D curvature of the leaf. A downward curving growth gradient indicates that at any point along the proximodistal axis of the leaf, the sides of the leaf grow slower than the center. This should lead to an increased curvature of the leaf across the transverse axis during the days where the gradient is clearly downward-curving; this concept is exaggerated in the Arabidopsis *peapod* mutant, whose dome-shaped leaf phenotype is explained by excess growth of the lamina but not the perimeter (White, 2006). By the same token, as the growth gradient becomes straighter or upward-curving, the leaf transverse curvature should decrease. Relations between growth gradients and leaf shape, including leaf curvature, will be discussed in more details in a related paper (Remmler and Rolland-Lagan, in prep.).

3.4.2 *Differences in the patterns of p and q support the hypothesis that expansion in the maximal and minimal directions of growth are regulated independently*

The proximodistal gradient and the shape of the gradient front differed between the scaling factors p and q, with p having a more exponential decline in growth rates from base to tip compared to the more linear decline of q, and p having a relatively straight gradient front throughout development in comparison to the very strongly downward curving gradient front of *q* in early development. Since *p* and *q* are directly implicated in the calculation of the growth rate and anisotropy, the patterns we observe in *p* and *q* may simply be the result of mechanisms controlling growth and anisotropy. However, such differences in their patterns could also indicate that *p* and *q* are under the control of different signals that diffuse at different rates in the leaf and originate from different positions. This offers support to Baskin's hypothesis that expansion in the maximal and minimal directions are regulated by distinct molecular mechanisms (Baskin, 2005).

Based on narrow leaf mutants with reduced cell expansion in the mediolateral axis and short leaf mutants with reduced cell elongation in the proximodistal axis, Tsuge et al. (1996) have similarly proposed that leaf expansion involves independent processes controlling cell elongation along the leaf length and leaf width. However, our results on the anisotropy and direction of growth show that growth orientation varies spatially and does not occur distinctly along the length and width axes of the leaf. Therefore it may be more appropriate to consider effects on expansion in the maximal and minimal growth directions, like Baskin, rather than along the leaf width and length specifically. It would be interesting to quantify the growth patterns in these mutants to see how those differ from the wild type in terms of growth direction, *p*, and *q*.

3.4.3 A polarizing substance may control growth directionality

Kennaway et al. (2011) recently outlined three possibilities regarding the control of growth directionality in developing tissues. The first possibility is that directions of growth are defined in the leaf tissue early in development and remain fixed locally, in which case any change in the pattern of growth directions at the whole organ level would reflect rotation of the tissue within the organ. Alternatively, growth orientation could be set globally through external information, such as gravity. In this case the pattern of growth directions at the whole organ level would remain the same as the organ develops. Lastly, growth direction may be governed by a polarizing substance which continues to diffuse through the tissue throughout growth. If this were the case, it would be impossible to predict the growth directions pattern without knowing details such as the source and diffusion coefficients of the proposed substance. Our results do not support the first two possibilities, because changes in growth orientation patterns do not correspond to tissue rotation (refer to SFigure 3.4D), and although there are some general trends in the direction of growth that remain consistent, the pattern does not remain exactly the same over time. Our results are therefore more consistent with the idea that growth direction is governed by a polarizing substance. Growth directionality may also be influenced by mechanical forces in the leaf, which is discussed in the next section in the context of the vascular system.

3.4.4 Growth patterns suggest growth differences between vascular and non-vascular tissue

Digital image sequence analysis studies have reported lower RGR values in leaf vascular tissue compared to surrounding non vascular tissue (Wang et al., 2011; Christ, 2005). Moreover, it has been suggested that there are tensile stresses along veins (Corson et al., 2009; Bohn et al., 2002), and that growth direction can be dictated by mechanical stresses in the tissue (e.g. Hamant et al., 2008). It is therefore likely that growth in vascular tissue is oriented along vascular paths. In our study we did not quantify growth at a sufficiently high spatial resolution to clearly distinguish vascular regions in individual samples, and since venation patterns vary, the vascular and interveinal regions of the different samples would not be perfectly aligned in the making of the mean spatial maps. However, at DAS11-14 q (but not p) values are lower along the midvein and along two lines extending out on each side of the midvein, which may correspond to the position of secondary veins. Maps of anisotropy and growth direction further show that the maximal direction of growth tends to be oriented along those same presumed vein positions. Those results therefore suggest that once veins have differentiated (Scarpella et al., 2006) growth in the vasculature occurs preferentially along vascular paths, and that growth along vein width is reduced compared to growth along the minimal direction of growth in surrounding tissue.

3.4.5 Applicability and ease of use of the method

The method presented here can be applied to young leaves as soon as their surface is exposed. In this study we used a line of plants lacking trichomes to make it easier to extract the leaf surface and particle 3D-coordinates, but the method can also be applied to leaves with trichomes, as we have tools to digitally crop trichomes out of the depth map (see Supplemental Materials and Methods) and can still detect most particle *x, y* coordinates on leaves with trichomes (personal observation). Thus, leaf growth can be quantified in a wide variety of species, ecotypes, and mutants.

The data acquisition period will depend on which developmental time points the researcher wishes to follow, with each imaging session of 15 leaves taking roughly two hours. Running through the programs, from image analysis to generation of mean spatial maps, for 15 leaves at 10 time points would take approximately one additional work week. This short processing time, along with our software for creating mean spatial maps, makes this a good tool for high-throughput phenotyping of spatiotemporal leaf growth patterns.

3.4.6 Accuracy and reliability

The nearly perfect bilateral symmetry of the growth patterns we observed provides strong evidence for the accuracy and reliability of this method. Moreover, the growth patterns we observed are consistent with other leaf growth analyses, that have shown a similar proximodistal gradient in growth rates in Arabidopsis (Wiese et al., 2007), as well as in other species, such as tobacco (Avery, 1933; Poethig and Sussex, 1985; Walter and Schurr, 1999; Walter et al., 2003), sunflower (Granier and Tardieu, 1998), grape (Wolf et al., 1986), spinach (Saurer and Possingham, 1970), cocklebur (Erickson, 1966; Maksymowych, 1959), ivy (Wang et al., 2011), and poplar (Taylor et al., 2003). An exception to this pattern was shown in soybeans (Ainsworth et al., 2005), where no spatial gradient was observed, leading the authors to conclude that the mechanisms of leaf growth in soybean may be different from other species. The soybean study followed growth from when the leaves were already 30mm in length. It would therefore be interesting to see whether a growth gradient is detectable in the soybean leaf in earlier time points, as our results show that the proximodistal growth gradient in Arabidopsis leaves becomes less steep as they mature.

To our knowledge, measurements of growth directionality and anisotropy have not been provided in leaf growth studies since Richards & Kavanagh (1943) and Erickson (1966). These measurements were made at relatively late stages of development when growth was nearly isotropic, though Richards and Kavanagh (1943) did show that leaf growth becomes more isotropic over time, which concurs with our findings.

While a spatial pattern is still discernible in the mean RGR maps for the later stages, it is less clear and standard error values are higher. This could reflect more variation in growth rates across samples in the later time points, as we also see that the leaf sizes diverge more as they mature. However, when we look at spatial maps of individual samples, we also see much “patchier” patterns at later time points, with regions of high growth rates interspersed with regions of lower growth rates, compared to relatively clear gradients in the earlier time points. This patchiness has also been noted to some extent in other leaf growth analyses (Wiese, et al., 2007; Christ, 2005). Christ (2005) hypothesized that this could be associated with patchy stomatal conductance, as spatial variation in stomatal openings could result in small spatial heterogeneities in turgor pressure, and thus growth. We propose that this increased patchiness in later time points could also be associated with the differentiation of cells as the leaf matures, as different cell types may have different cell wall properties which could respond differently to growth cues. This theory is supported by a recent study showing that stomatal guard cells follow substantially different growth dynamics than those of neighbouring epidermal pavement cells (Kheibarshekan Asl, et al., 2011). Changes in the flux or position of growth signal sources in the leaf blade over time (see Aloni, et al., 2003, for example) could also play a role.

3.4.7 *Other applications of the method*

Many aspects of the methodology we presented here could be used together or independently for other studies. For example, the software we developed for computing growth could be used to compute growth parameters from 3D data generated from other methods, such as confocal microscopy, optical projection tomography, or selective plane illumination (see Ntziachristos, 2010 for review). The tracking and growth-computing software could also be adapted to follow fluorescent particles or other distinguishable markers on growing tissues in other organs or organisms. The programs for generating mean spatial growth maps could also be adapted for use by researchers using other growth quantification techniques.

3.4.8 *Limitations and future improvements*

Although the method we describe makes it possible to quantify surface growth in 3D, using z-stacks for data acquisition means that landmarks must be visible from one vantage point. Thus our microscopy setup could not be used to quantify growth in severely wrinkled leaves or those that have curved under themselves, although, depending at which stage the leaf curling/wrinkling occurs, it may be possible to at least identify the alterations in growth patterns that lead to the curvature/folds.

The leaf shape and surface extraction, particle digitization, and particle-tracking algorithms have been mostly automated, but we note that they do need to be visually verified by the user, and in some cases manually adjusted.

3D length and width measurements follow a logarithmic curve similar to what has been observed in other studies. A slight drop in leaf size at DAS16 appears to be due to the fact that the leaves of our secondary data set, collected a few weeks after the original data set (see Supplemental Information), continued to grow from DAS14-15 at a higher rate than the original data set. Although temperature and air pressure is controlled in our laboratory, it has been shown that even small variations in growing conditions and handling of plants can lead to significant differences in leaf growth phenotypes (Massonnet et al., 2010). Therefore in order to compare growth patterns from datasets collected at different times, we would suggest to always grow a set of wild type plants along with the set of plants analyzed. Simple 2D measurements of leaf area or leaf width from those wild type plants over the course of development could then be used to generate a reference growth curve to be compared between experiments for calibration purpose.

3.4.9 Conclusion

The method outlined in this paper makes it possible to describe average spatiotemporal growth patterns at the 3D surface of leaves. Mean spatial maps of growth parameters from multiple samples show clear spatiotemporal patterns, which may reflect the influence of morphogenetic signals. For instance, if a signal promoting or restricting growth is produced at a given position on the leaf and during a given time, any disruption to its localization or timing will be reflected in the leaf growth patterns. Generating mean growth maps from multiple samples will make it possible to perform standardized comparative analyses of growth patterns between wild type and mutants and/or between species. Such comparative analyses may shed light on the morphogenetic mechanisms controlling leaf growth and shape. Similar approaches to the ones presented in this paper could also be applied to explore the control of morphogenesis in other organs and organisms.

In the following chapter we will use the same data to link the growth patterns to 3D changes in shape during leaf development.

3.5 Material and methods

3.5.1 Plant materials and growth conditions

In this study we use *Arabidopsis Thaliana* ecotype Landsberg *erecta* Ler-0 *glabra1-1*, available from the Arabidopsis Biological Resource Center as seed stock number cs64. We follow the growth of one of the first two rosette leaves on each plant, chosen randomly, as is standard practice (see Scarpella et al. 2006 for example) since they develop almost simultaneously.

Seeds are surface sterilized and imbibed at 4˚C in the dark for 4 days, then sown in autoclaved Pro-Mix® potting soil (Premier) with 5 plants per 3”x3” pot, and grown in the lab at 22˚C under an ArabiSun™ lighting system (Lehle Seeds), with 16 hour light cycles, watering as needed to keep the soil moist. Plants with similar germination times and sizes are used for analysis. We use one group to track growth from DAS7 to DAS12, a second to track DAS12-18, and a third set to obtain additional information for DAS10-14 (see Supplemental Materials and Methods for further details).

3.5.2 Particles and application technique

We use the 6.2μm and 29.6μm SPHERO™ Fluorescent Yellow Particles (Spherotech), using the former on smaller leaves (up to DAS14) and the latter on larger leaves. We start by making a strong and weak dilution of the particles in distilled water: approximately 2μL/mL and 10μL/mL for the 6.2μm particles, and 40μL/mL and 200μL/mL for the 29.6μm particles. If let to sit for several minutes, the particles will fall to the bottom of the solution, at which point most of the water can be removed from the top and replaced with fresh water, to help remove any chemicals present in the original particle solution. After this, the solutions are vortexed frequently before and during application to prevent settling and clumping of the particles. A syringe with a 28-gauge needle is used to apply the particle solution to the leaf surface, starting with the weaker solution. If the desired leaf can be fully covered by a spherical droplet of the solution, the particles are left to settle on to the leaf surface (approximately 20 minutes). At this time the droplet of water can be removed by touching it with a piece of tissue or drawing off with the syringe, and allowing any remaining water to evaporate. More information about the particle application technique can be found in the Supplemental Materials and Methods.

3.5.3 Microscopy and image acquisition

Z-stack images are obtained with a Leica Z16 APO AMacroFluo motorized fluorescent macroscope using a Leica DFC350 camera (Leica Microsystems). The Leica Application Suite Montage Module (Leica Microsystems) is used to generate the multifocus images and depth map. To visualize the fluorescent yellow particles we use a GFP filter cube (excitation filter BP 470/40, dichromatic mirror 500, suppression filter BP 525/50), with the intensity of the fluorescent light source kept as low as possible. Further details on image acquisition settings are available in the Supplemental Materials and Methods.

3.5.4 Computations

All custom written programs were developed in Matlab (The Mathworks Inc.), using many Matlab built-in functions as well as functions from the Matlab Image Processing Toolbox and Statistics Toolbox. Statistical analyses were performed using IBM SPSS 18 (IBM) software. Further details on the software we developed can be found in Supplemental Materials and Methods.

3.6 Acknowledgements

We thank Rebecca Assaf for sharing data from a sister project used for early development of some computational tools, Mona Hosseini-Abardeh for her participation in early stages of this work, Alice Szymanski for assistance with collection of a preliminary data set, and R. Stadler and N. Sauer (University of Erlangen, Germany) for providing seeds of the AtSuc2prom:GFP plants used for SFigure 3.1C.

3.7 Supplemental Figures

SFigure 3.1: Controls and validation of methods.

Further details on data set and validation of methods to show that imaging and bead application does not disturb plant growth and that beads do stick to the leaf surface.

(A) 3D leaf width over time of all samples in the data set. The green and blue lines represent the original batch of plants that were imaged, with a set of plants being imaged from DAS7-12 (green lines) and a set of plants being imaged from DAS12-19 (blue lines). The orange lines represent a secondary batch, grown a few weeks later in the same conditions. The data from this secondary batch was matched to the growth curves of the original data set (see Supplemental Materials and Methods for more information).

(B) To investigate the effect of daily imaging on leaf growth, we compared the 3D width of leaves that underwent bead application at DAS7 and daily imaging under brightfield and fluorescent light until DAS12 (N=14), to DAS12 leaves grown concurrently in the same conditions that had not been previously imaged (N=12). Error bars represent the 95% confidence interval. A Mann-Whitney U test reveals that there is no significant difference in the leaf width of the two groups (U=67.0, Z=-0.874, P=0.382), confirming that particle application and imaging does not disturb leaf growth.

(C) Fluorescent particles were applied to the leaves of a strain of Arabidopsis that has green fluorescent vasculature (AtSuc2prom:GFP), and were imaged at two time points two days apart. Here we show three samples, and highlight the position of a few beads from one time point to the next by coloured circles. The particles remain in the same relative positions compared to the vasculature, demonstrating that they remain fixed to the leaf surface and move with it as the tissue expands. We used fluorescent red beads which still fluoresced weakly under the GFP filter, since the vasculature fluorescence was very weak compared to and overpowered by the yellow fluorescent beads. Scale bars represent 1mm.

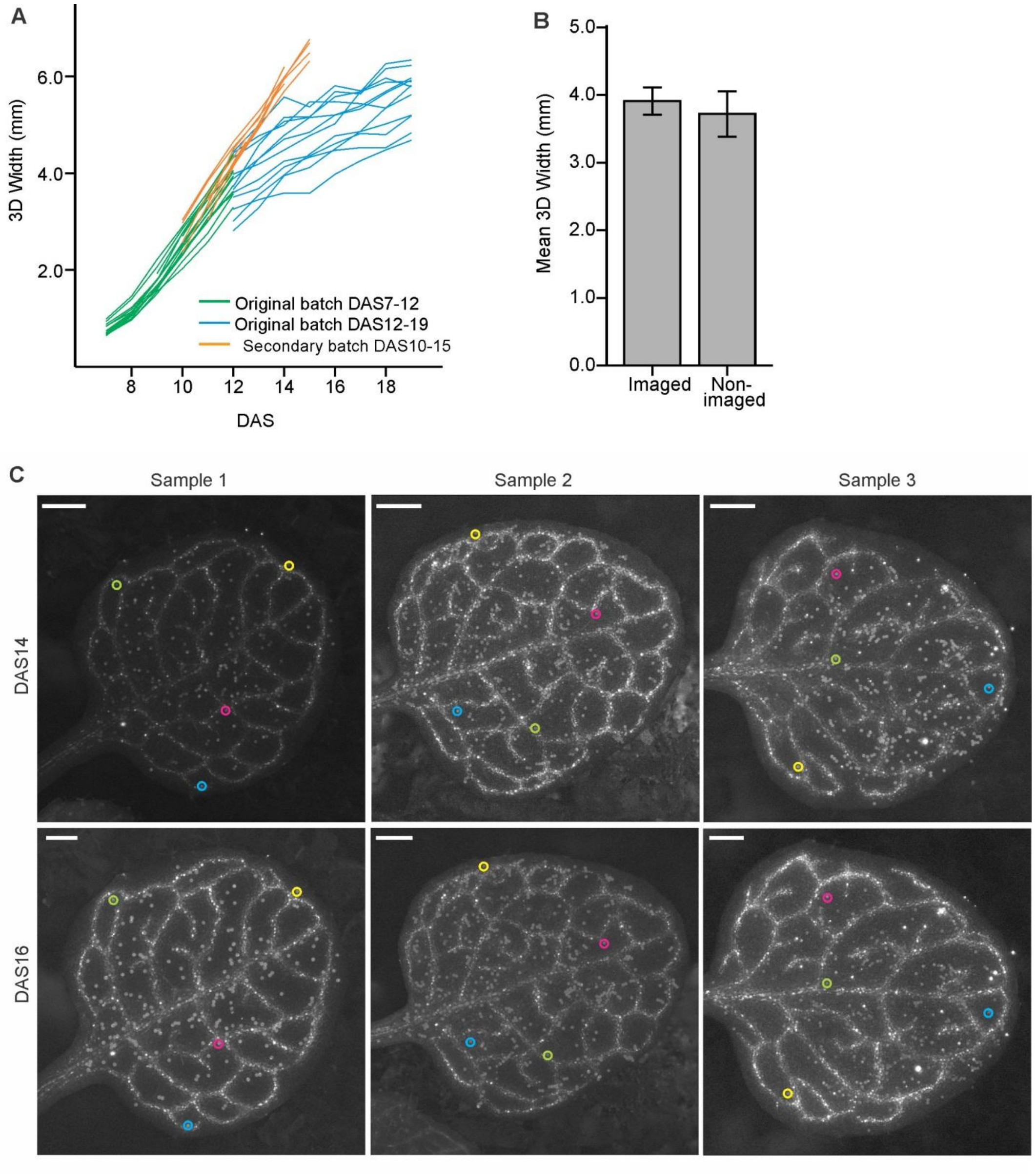
A
3D Width (mm)
6.0
4.0
2.0
8
10
12
14
16
18
DAS
Original batch DAS7-12
Original batch DAS12-19
Secondary batch DAS10-15
B
Mean 3D Width (mm)
5.0
4.0
3.0
2.0
1.0
0.0
Imaged
Non-imaged
C
Sample 1
Sample 2
Sample 3
DAS14
DAS16

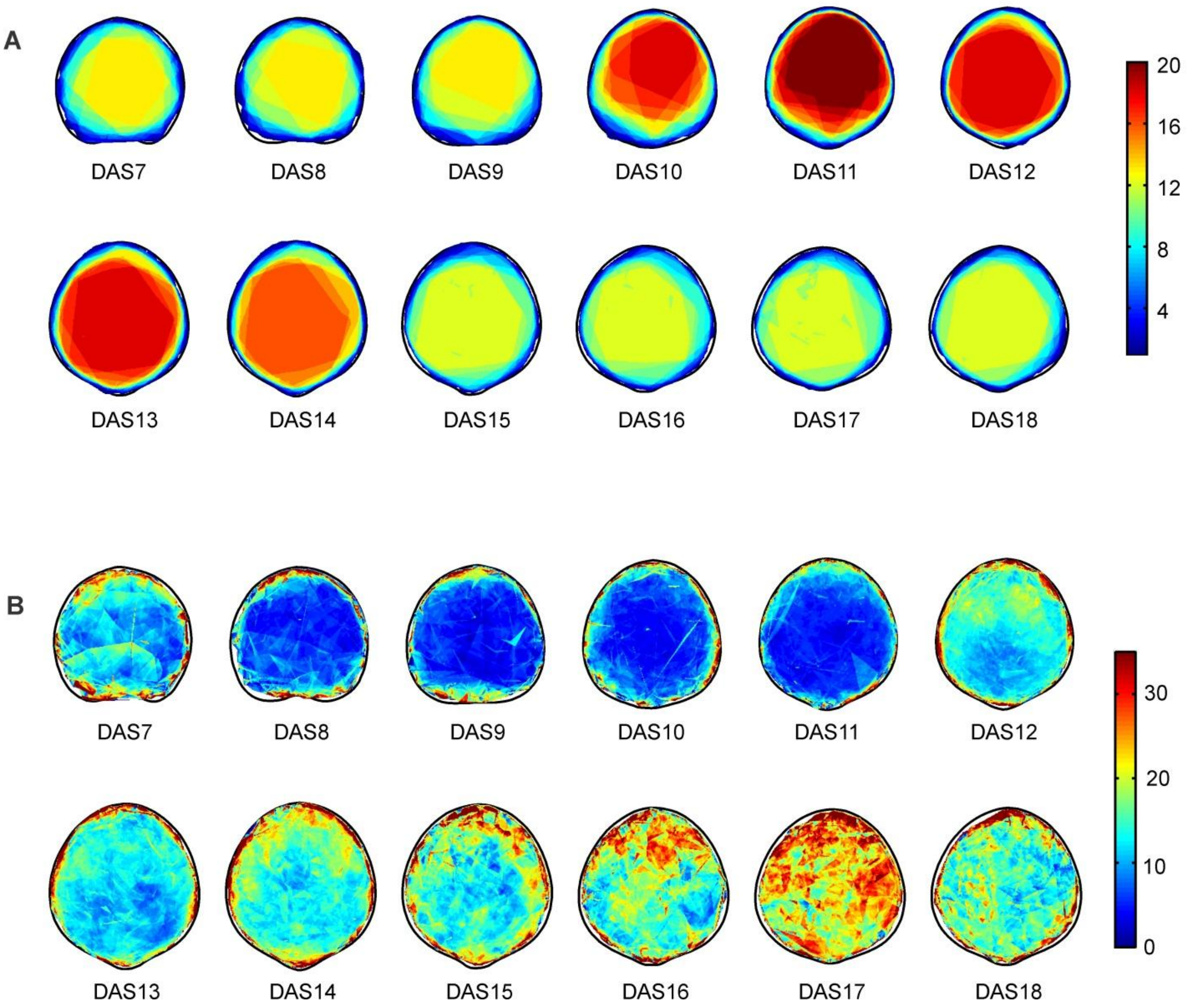

SFigure 3.2: Sample number and RSE maps for RGR.

(A) Number of samples used to compute the mean values at each point on the mean spatial maps, coloured according to the scale shown on the right.

(B) Relative standard error (RSE) of the mean RGR maps, coloured according to the scale shown on the right. RSE is expressed as a percentage, e.g. if the error at a point is 30% RSE and the mean growth at the same point is 20% RGR, the RGR at that point is 20±6% (30% of 20% is 6%).

SFigure 3.3: Further analyses of spatiotemporal patterns and error of *p* and *q*.

(A-B) To illustrate patterns in the scaling factors *p* and *q* at the leaf base and tip over time, we compute and plot the average of the values in the bottom and top quarter (as shown in the diagram) of the mean spatial map of *p* (A) and *q* (B) for each DAS.

(C-D) We assess the gradient shapes by comparing the values of *p* (C) or *q* (D) in a small window at the center to those in a small window at the same lateral position at the side of the spatial map of each sample (as illustrated in the diagram). If the gradient has a downward curving shape, the values in the center will be higher than those at the sides, and the center-to-side ratio will thus be greater than one, with more strongly curving gradients having higher center-to-side ratios, and vice versa. N=12-20. Error bars represent the 95% confidence interval.

(E-F) Spatial maps of the relative standard error (RSE), expressed as a percentage, of the mean maps of *p* (E) and *q* (F). RSE values are plotted by colour according to the colour scales on the right.

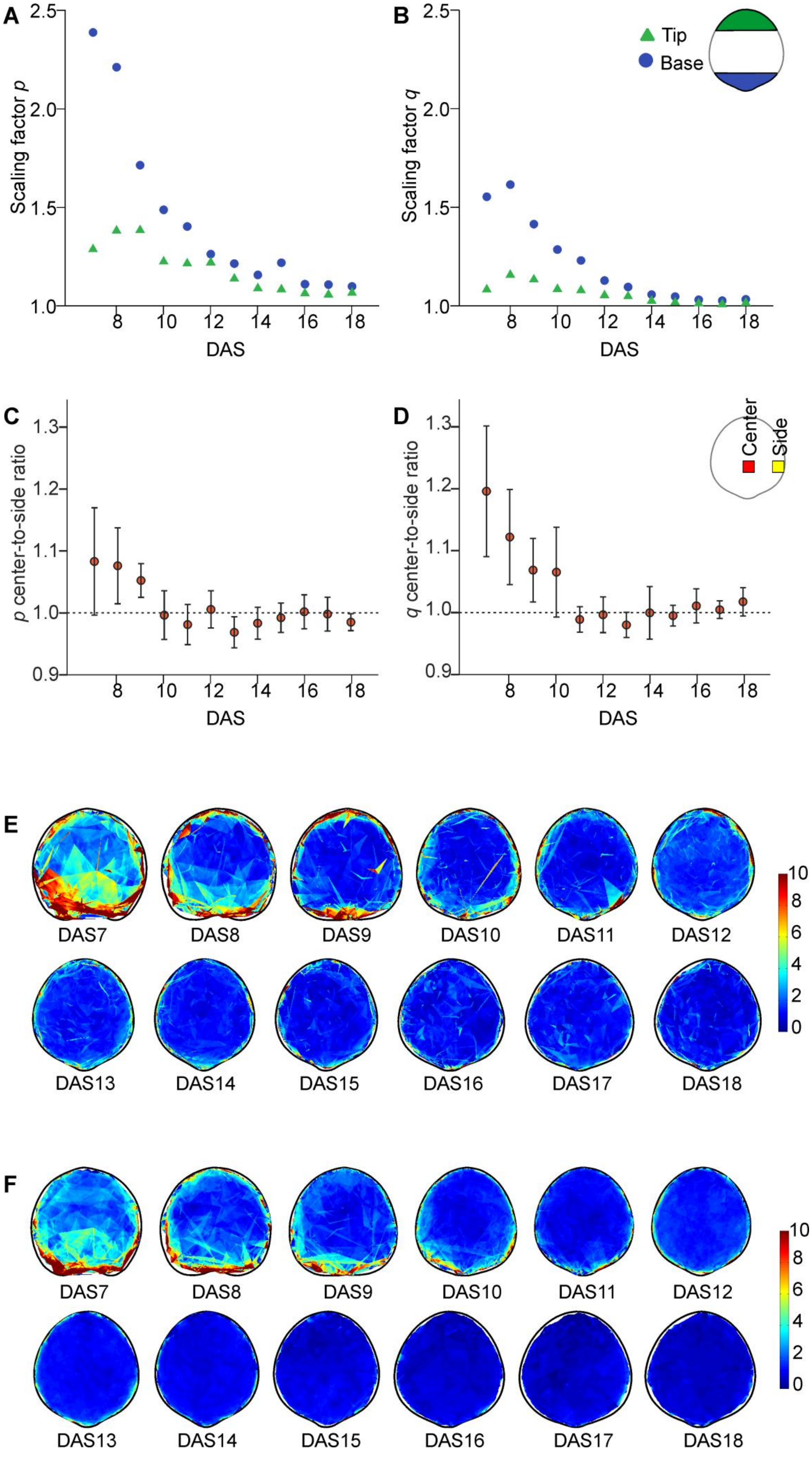
A
Scaling factor p
2.5
2.0
1.5
1.0
8
10
12
14
16
18
DAS
B
Scaling factor q
Tip
Base
C
p center-to-side ratio
1.3
1.2
1.1
1.0
0.9
D
q center-to-side ratio
Center
Side
E
DAS7
DAS8
DAS9
DAS10
DAS11
DAS12
DAS13
DAS14
DAS15
DAS16
DAS17
DAS18
10
8
6
4
2
0
F

SFigure 3.4: Error and variance maps of anisotropy and growth direction, and maps of the rotation of growth direction with associated error maps.

(A) Spatial maps of the relative standard error (RSE) of the mean maps of anisotropy, where RSE values are expressed as a percentage and plotted according to the colour scale on the right.

(B-C) Circular variance maps of the mean direction of growth (B) and angles of tissue rotation (C), where the circular variance values are plotted according to the colour scales on the right. Values closer to zero represent low variance and values closer to 1 represent high variance.

(D) To assess if or how the maximal direction of growth rotates within the tissue over time, we compare the direction of growth within a piece of tissue at two successive periods of growth while taking into account changes in the orientation of the tissue itself. We calculate this by $\theta_{t2\text{ to }t3} - \theta_{t1\text{ to }t2} - \Psi_{t1\text{ to }t2}$, where $\theta_{t2\text{ to }t3}$ is the direction of maximal growth from time *t2* to *t3,* $\theta_{t2\text{ to }t3}$ is is the direction of maximal growth from time *t1* to *t2,* and $\Psi_{t1\text{ to }t2}$ is the rotation of the tissue from time *t1* to *t2.* Thus, in the maps shown, the lines represent how the maximal direction of growth rotates within the tissue in that area compared to growth over the previous time period. A horizontal line indicates zero rotation, i.e. that the maximal direction of growth remains fixed within the tissue.

(E) Circular variance maps of the mean angles of rotation of the direction of growth (C), where values closer to zero represent low variance and values closer to 1 represent high variance. Circular variance values are plotted by colour according to the colour scales on the right.

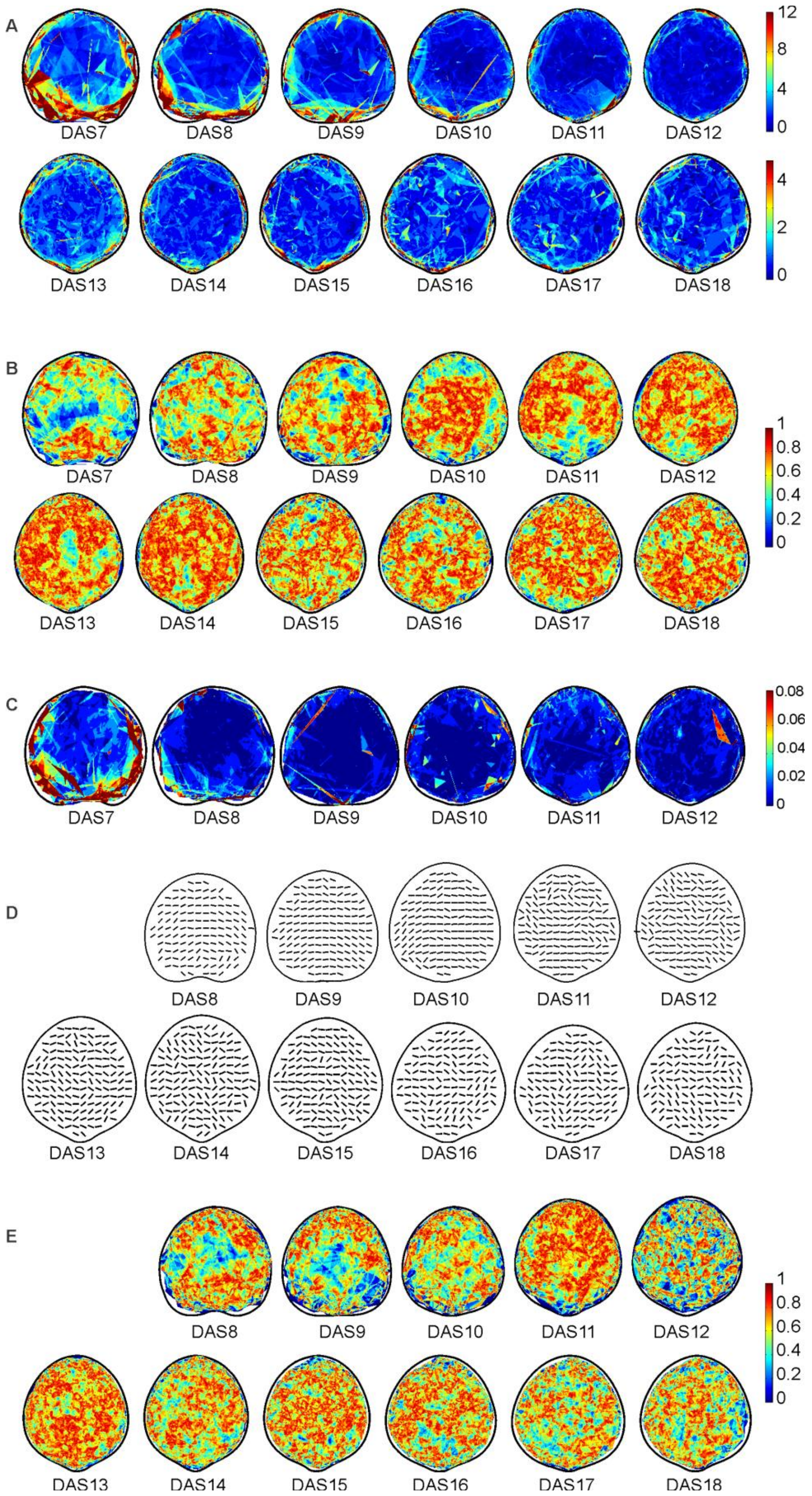
A
DAS7
DAS8
DAS9
DAS10
DAS11
DAS12
12
8
4
0
DAS13
DAS14
DAS15
DAS16
DAS17
DAS18
4
2
0
B
DAS7
DAS8
DAS9
DAS10
DAS11
DAS12
1
0.8
0.6
0.4
0.2
0
DAS13
DAS14
DAS15
DAS16
DAS17
DAS18
C
DAS7
DAS8
DAS9
DAS10
DAS11
DAS12
0.08
0.06
0.04
0.02
0
D
DAS8
DAS9
DAS10
DAS11
DAS12
DAS13
DAS14
DAS15
DAS16
DAS17
DAS18
E
DAS8
DAS9
DAS10
DAS11
DAS12
1
0.8
0.6
0.4
0.2
0
DAS13
DAS14
DAS15
DAS16
DAS17
DAS18

DAS	Test statistic	RGR	p	q
7	Z	-4.633[a]	-4.165[a]	-6.838[a]
	Sig.[c]	.000	.000	.000
8	Z	-5.147[a]	-4.589[a]	-6.713[a]
	Sig.[c]	.000	.000	.000
9	Z	-5.470[a]	-5.376[a]	-7.129[a]
	Sig.[c]	.000	.000	.000
10	Z	-2.544[a]	-.631[a]	-6.204[a]
	Sig.[c]	.011	.528	.000
11	Z	-1.791[b]	-2.770[b]	-2.342[b]
	Sig.[c]	.073	.006	.019
12	Z	-.559[b]	-1.059[b]	-.789[b]
	Sig.[c]	.576	.290	.430
13	Z	-3.297[b]	-5.679[b]	-3.667[b]
	Sig.[c]	.001	.000	.000
14	Z	-.614[b]	-1.611[b]	-1.113[b]
	Sig.[c]	.539	.107	.266
15	Z	-.366[a]	-.906[a]	-2.545[a]
	Sig.[c]	.714	.365	.011
16	Z	-3.115[b]	-2.961[b]	-2.662[b]
	Sig.[c]	.002	.003	.008
17	Z	-.749[b]	-.640[b]	-1.600[b]
	Sig.[c]	.454	.522	.110
18	Z	-1.619[b]	-3.432[b]	-1.210[b]
	Sig.[c]	.105	.001	.226

a. Based on negative ranks.
b. Based on positive ranks.
c. Asymptotic 2-tailed significance

STable 3.1: Testing the gradient shapes of RGR, *p*, and *q* at each time point

To statistically assess the gradient shapes observed for RGR, *p* and *q*, we compared the values in a small window at the center to those in a small window at the same longitudinal position at the sides of each single sample leaf spatial map (refer to diagram SFigure 3.3C-D), with a Wilcoxon signed-rank test. If the observed curvatures of the gradients are significant, the difference between the values at the center will be significantly different from the values at the sides.

3.8 Supplemental Materials and Methods

3.8.1 Further details on plant materials and growth conditions

This method can be applied to fully-opened wildtype leaves, but to make it easier to visualize the particles and to simplify extraction of the 3D leaf surface, we use a line of *Arabidopsis Thaliana* ecotype Landsberg *erecta* that lacks trichomes (L*er*-0 *glabra1-1*, available).

We find it best to sow many more seeds than required for the data set for a few reasons. The first and most obvious reason is that some of the seeds may not germinate. Furthermore, of those that do germinate, there will be some degree of variation in germination time, and we want to be able to select from this a subset that are at approximately the same developmental stage. For this study we selected the group of plants to be used according to those which showed fully opened cotyledons on DAS3. In this subset we would still like to have more plants than required for the data set as some may be discarded in the particle application step.

3.8.2 Further details and techniques on particle application

If the droplet of particle solution does not fully cover the leaf surface, this can be resolved by adding a small amount of the more concentrated solution to the droplet, and then overlaying it with a tiny piece of tissue, which will break the spherical shape and force the solution to spread out across the leaf; the tissue is removed after it has dried (approximately 60 minutes).

We generally apply the particles to both of the first two rosette leaves of the chosen plants, and then select the leaf with the best particle coverage for further imaging. If the dispersion or concentration of particles is not ideal, the particles can be pushed around on the leaf surface with a small piece of wet tissue to improve dispersion, blotted with the tip of a moist tissue to remove some particles in concentrated areas, or blotted with the tip of a tissue dipped in the more concentrated solution to add particles to sparse areas. However, because mechanical stimulation is known to affect growth

(Chehab et al., 2009), these manipulations are kept to a minimum, and if good particle coverage is not easily achieved, the plant is discarded

3.8.3 Details on settings for microscopy and image acquisition

There are several settings on the microscope and camera (Leica DFC350) that can be adjusted to optimize the images obtained. As over-exposure to light could potentially alter plant growth, we are always conscious of choosing settings that also minimize the intensity and duration of light exposure. We use the lowest levels of brightfield light intensity, adjusting the brightness as needed, from 10 to 30, and the lowest level of fluorescent light intensity, adjusting the brightness from 6.3 to 100%. The 2.0x objective lens is used for smaller leaves (up to around DAS15) and the 1.0x lens is used for the larger leaves.

The z-stack is acquired by taking a series of images at regular vertical intervals within the focal range of the specimen, which is set manually by setting the bottom of the range to where the lowest point of the leaf is just out of focus and the top end to where the highest point of the leaf is just out of focus. The regular vertical interval size is referred to as the step size, and is optimal when it is small enough to capture the leaf curvature and shape in 3D .(which is important for generating a clear montage image and accurate depth map) without being redundant and causing unnecessary longer exposure of the plant under the microscope lights. A visual assessment of the depth map quality is made from the confidence map, in which grayscale values ranging from black to white represent 0-100% accuracy (Figure 3.1C). The step size can be set automatically by the Leica software's "Optimize step size" option, which adjusts with the 2D size (zoom) of the specimen, or it can be entered manually to obtain the desired vertical resolution. For fluorescence images (for which the depth map is not used), the step size can be increased to shorten the leaves' exposure to the fluorescent light, since we do not use the depth map of the fluorescence stack.

To visualize the fluorescent yellow particles we use a GFP filtercube (excitation filter BP 470/40, dichromatic mirror 500, suppression filter BP

525/50), with the intensity of the fluorescent light source kept as low as possible. The camera settings for fluorescent images need to be determined on a case-by-case basis, as the best settings depend on the density of particle coverage, and the apparent brightness of the particles. The latter depends on the size of the particles and the relative size of the leaf; for example, a 29.6μm particle appears quite large and bright on a leaf at DAS15, but will appear much smaller and fainter (until the camera settings are adjusted) at DAS21 when the leaf is comparatively much larger. We find the lowest levels of fluorescent light intensity to be sufficient, with exposure times ranging from 700-900ms, and gamma correction and gain usually set around 0.55 and 3.2x respectively. The same camera settings can usually be used for the brightfield images as well.

3.8.4 Computational details of the particle tracking algorithm

For each particle on a leaf at time *t1*, the pattern-matching algorithm computes and records a “neighbour pattern” based on the *n* closest neighbouring particles; the default number of neighbours used in the pattern is three, but this can be changed by the user if desired. A 2D coordinate system is centered on the particle in question, and we compute the polar coordinates (radius, θ) of the *n* neighbouring particles within that coordinate system, through the Matlab *cart2pol* function (built-in Matlab functions are cited in italics throughout). We use the radius to compute the relative distance of each neighbour from the particle in question as the radius divided by the 2D length of the leaf. θ gives the angle of the neighbour relative to the the particle in question. We store the relative distances of the neighbours in one matrix (D_{t1}) and their orientations in another (O_{t1}); each matrix has the dimensions *p* by *n*, where *p* is the number of particles on the leaf, and *n* is the number of neighbouring particles for which we store data. Each row *p* of D_{t1} contains the relative distances of the *n* closest neighbours to particle *p,* and the corresponding indices of O_{t1} contain their orientations. Data for neighbours is always stored by increasing distance from left to right; i.e. data for the closest neighbour is in the 1st column, data for the second closest neighbour is in the 2nd column, etc.

This is repeated for all particles at *t2.* Now the neighbour pattern of each particle at time *t1* is compared to the neighbour pattern of each of the particles at *t2*, based on the ratio of the relative distances and difference in orientation of the closest neighbours. Because growth is not uniform, we do not expect the pattern to remain exactly the same and we allow for some discrepancy. The default discrepancy permitted is 30% for the distance ratio and 0.15 radians for the angle difference, but these can be adjusted by the user if need be. When the neighbour pattern of a particle at *t1* (*p1)* is sufficiently similar to the neighbour pattern of a particle in at *t2 (p2),* it is recorded as a potential match. I.e.

```
FOR p1 = 1 to the number of particles on the leaf at t1
    FOR p2 = 1 to the number of particles on the leaf at t2
        FOR n = 1 to the number of neighbours used
            $dD(n)=D_{t1}(p1,n) / D_{t2}(p2,n)$
            $dO(n)=abs(O_{t1}(p1,n)-O_{t2}(p2,n))$
        EndFOR
        IF $max(dD) < 0.3$ AND $max(dO) < 0.15$
            Particle p1 and p2 are recorded as a potential match
        EndIF
    EndFOR
EndFOR
```

Additional checks at the end of the program will remove any matches where more than one potential match was identified, and otherwise saves the best match.

It is usually possible to match an estimated 80-90% of the particles with this algorithm, with 100% accuracy most of the time. However, matches should be verified by the user, and if an insufficient number of matches were found, or an erroneous match found, there is an option to add or delete particles manually.

Once most of the particles have been matched, their change in coordinates between the successive time points can be used to warp all of the *t1* coordinates to *t2* using piecewise transformations. The matched particles are grouped into vertices of non-intersecting triangles using Matlab's *delaunay* triangulation function (built-in Matlab functions are cited in italics throughout). For each of these triangles, an affine transformation matrix is calculated based on the change in the vertex coordinates from time *t1* to *t2* using the *cp2tform* function, and is applied to the *t1* particles making up the triangle and any that lie within it via the *tformfwd* function. This is repeated for all triangles, and a second-order polynomial function, derived from all of the matched points, is applied to remaining particles around the perimeter that do not lie within any of the triangles (again using the *cp2tform* and *tformfwd* functions). If necessary, additional matches can be manually added in areas that are crowded or not well aligned

The result is perfect alignment of the matched particles and usually a very good alignment of the remaining un-matched particles on the leaf at *t2*. The remaining particles can now be matched according to the alignment, by finding the warped *t1* particle which is the closest to each *t2* particle. There are again a few checks in place that can be adjusted by the user if desired to increase the number of matches or increase the accuracy, including the maximum distance allowed between particles in order for them to be considered a match, and a minimum distance allowed between the top two matches (i.e. if there are potentially two matches for a particle, no match will be recorded). There is also an option to consider a match when it is not within the minimum distance but if there are no other possible matches nearby.

3.8.5 Additional discussion and validation of use of beads for tracking growth

We do not know what physical interactions occur between the leaf surface and the particles, as we are unable to clearly see where the particles rest on the epidermis at a cellular scale with our microscope, but it appears that they perhaps settle in grooves between cells. This postulation is also supported by the behaviour of particles on petiole tissue: when part of a cotyledon petiole is covered by the particle solution during application to the emerging leaves, we observe a concentrated quantity of particles adhering to the petiole in parallel lines along its axis, which corresponds with the arrangement of the long rectangular cells of the petiole (see the scanning electron micrographs of McConnell and Barton, 1998). They may also rest at other places on the leaf at small ridges that can be seen on the leaf cuticle (see the scanning electron micrographs of Jenks et al., 1996), or perhaps even stick to the wax. At the small scale of a 6.2μm polystyrene particle, even weak intermolecular forces could be sufficient to hold it in place.

Particles do not fall off the leaves when the pots they are in are moved around, and although they can sometimes be moved on or removed from the leaf by wetting the leaf and blotting with tissue, we have found that some particles will stick to the surface so securely that no amount of rinsing or wiping will remove them

3.8.6 *Shifting data using leaf area as an indicator of developmental stage*

Days after sowing may not necessarily reflect the growth stage of a leaf, as not all plants germinate at the same time. In order to group the data as accurately as possible, we sowed approximately 100 seeds, and of those that germinated, selected 24 which had fully opened cotyledons at DAS4 and first leaves of approximately the same size at DAS7, and randomly divided these into two sets. One half was followed from DAS7 to DAS12, and the second was followed from DAS12 to DAS19. Since the imaging did not affect the leaf growth, we are able to combine the two data sets to create a continuous standard growth curve of a 2D projection of the leaf areas.

As leaves from the first data set grew, particles in fast growing areas became further apart, leading to less particle coverage at the base of DAS10-12 leaves. We therefore sowed an additional set of plants, which were imaged from DAS10 to DAS14. Due to variations in germination times, we used a program that automatically aligned each plant to the standard growth curve according to a weighted least squares fit of the leaf areas over time.

Chapter 4: Quantifying tissue deformation: the link between growth patterns and morphogenesis

---

4.1 Summary

The formation of an organ's shape in development is the product of spatial and temporal patterns of tissue growth. Quantification of these patterns is therefore useful for determining the underlying morphogen actions that are responsible for generating shape. In Chapter 2 we presented a novel method to quantify growth patterns in three dimensions at the surface of leaves. However, as growth is a complex process, it can be difficult to intuitively predict the outcomes of growth patterns on shape development. In this chapter we present novel computational tools to quantify 3D shape changes and tissue deformation growth over the course of leaf development, from data acquired with the method we used to quantify growth. The results show that although central regions of the leaf expand more due to higher growth rates, the lateral regions are counterbalanced by the addition of new tissue due to tissue displacement, and leaf curvature thus remains within a narrow range throughout development. This highlights the importance of quantifying deformations for proper analysis of shape mutants, as expansion alone is not sufficient to explain 3D changes in shape.

4.2 Introduction

The shape of virtually any organ is essential for its proper functioning. In the case of leaves, the primary importance of shape is to optimize photosynthetic surface, while balancing other factors such as offsetting water loss, improving convective cooling, or increasing resistance to gravitational or physical environmental forces (see reviews by Cronk (2009) or Tsukaya (Tsukaya, 2006)).

Qualitative analyses have identified a multitude of leaf mutants with altered shapes. Several advanced computational methods have been developed to quantitatively characterize these leaf morphologies in terms of their outline shapes (e.g. Backhaus et al., 2010; Bylesjo et al., 2008; Langlade et al., 2005; Weight et al., 2008) and their 3-dimensional (3D) curvatures (e.g. Kaminuma et al., 2004; Liu et al., 2010).

These methods are useful for identifying and qualitatively describing mutant shape phenotypes, but do not provide information about what disruptions to the underlying spatial and temporal patterns of growth occurred to give rise to the shape differences. Our lab recently developed a novel technique for quantifying these patterns in leaves (Chapter 3). Unique features of this method include the ability to track growth from an early stage of development, to compute growth from 3D coordinates, and to combine data from multiple samples to describe mean growth patterns. This information will be useful in investigating the mechanisms of leaf morphogenesis by making it possible to analyze developmental differences in growth patterns of various leaf shape mutants. However, as growth is a complex process, involving multiple parameters occurring over time and in three-dimensional (3D) space, it can be difficult to conceptualize how growth patterns relate to shape development.

To visually describe the movement and deformation of tissue over time, we follow in the steps of D'Arcy Thompson's grid transformations (1917). In this revolutionary work, Thompson showed how a grid of points defining the adult morphology of one species could be warped to produce the adult morphology of a related species through relatively simple affine transformations. This surprising and intriguing result was, however, left without a sound biological explanation. In reality, these deformations reflect the accumulation of shape differences between two species over the course of their development. To understand the underlying mechanisms that give rise to these different shapes would thus require an analysis of the morphologies over various stages of growth (Arthur, 2006). In the following, we present novel computational tools that allow us to compute and display tissue deformation and shape changes occurring over the course of leaf development, from data acquired with the method we used to quantify growth. Together with spatial growth information, these tools will make it possible to investigate and better understand the effects of growth patterns on shape outcomes in leaves.

4.3 Results

Our method for quantifying leaf growth involves tracking topically applied fluorescent microparticles on the leaf surface over time in 3D (Chapter 3). This was applied to the first leaves of a number of *Arabidopsis Thaliana* plants such that we had growth data for 12-23 samples per day, from 7 days after sowing ("DAS7") through to DAS18 when growth has nearly stopped. Using custom software, we combined growth data from all samples at each time point to create mean spatial maps of growth parameters. Refer to Chapter 2.

In the following we present the results of additional computational tools, written by our lab in Matlab (The Mathworks, Inc), applied to this same dataset, for quantifying tissue deformation and shape changes.

4.3.1 Making mean leaf growth velocity and displacement maps

The simplest way to assess tissue movement during growth from our data is by computing tissue displacement. In Chapter 3, the 3D coordinates of tracked particles were used to subdivide the leaf surface into small triangular regions; based on the change in area, shape, and orientation of these triangles over time, we were able to compute various parameters of leaf growth. We also compute the displacement of each triangle's centroid, in the x, y, and z axes. We then combine this spatial displacement data from all leaf samples (N=12-23) for each time point analyzed to produce mean displacement maps, using the algorithms previously described (Chapter 2). Displacement data such as this is more commonly represented through velocity vectors, shown in Figure 4.1. These are helpful for visualizing the directions of displacement and spatial patterns within each map, but it can be difficult to interpret the temporal changes since the leaf size and velocities change too dramatically over time to show them all on the same scale. Also it is only possible to see displacement in the x and y dimensions, but not z. For these reasons, we also make mean spatial maps of displacements using colour maps (Figure 4.2).

In the x-axis, we see that the outward displacement of tissue is always higher in areas closer to the leaf base in early time points, but gradually evens out by approximately DAS12. In the y-axis, vertical displacement is stronger at the center of the leaf in early time points, but also evens out by approximately DAS12. Z-displacement will be addressed later in our analysis of leaf curvature.

We note that one should be cautious about interpreting the direction of the velocity vectors and the sign of the displacement values in terms of moving left or right (x), up or down (y), or higher or lower (z), as these are dependent upon the reference point from which they are measured. Also, they are difficult to relate to local tissue expansion, since the displacement of any point includes the cumulative displacement of all tissue between it and the reference point.

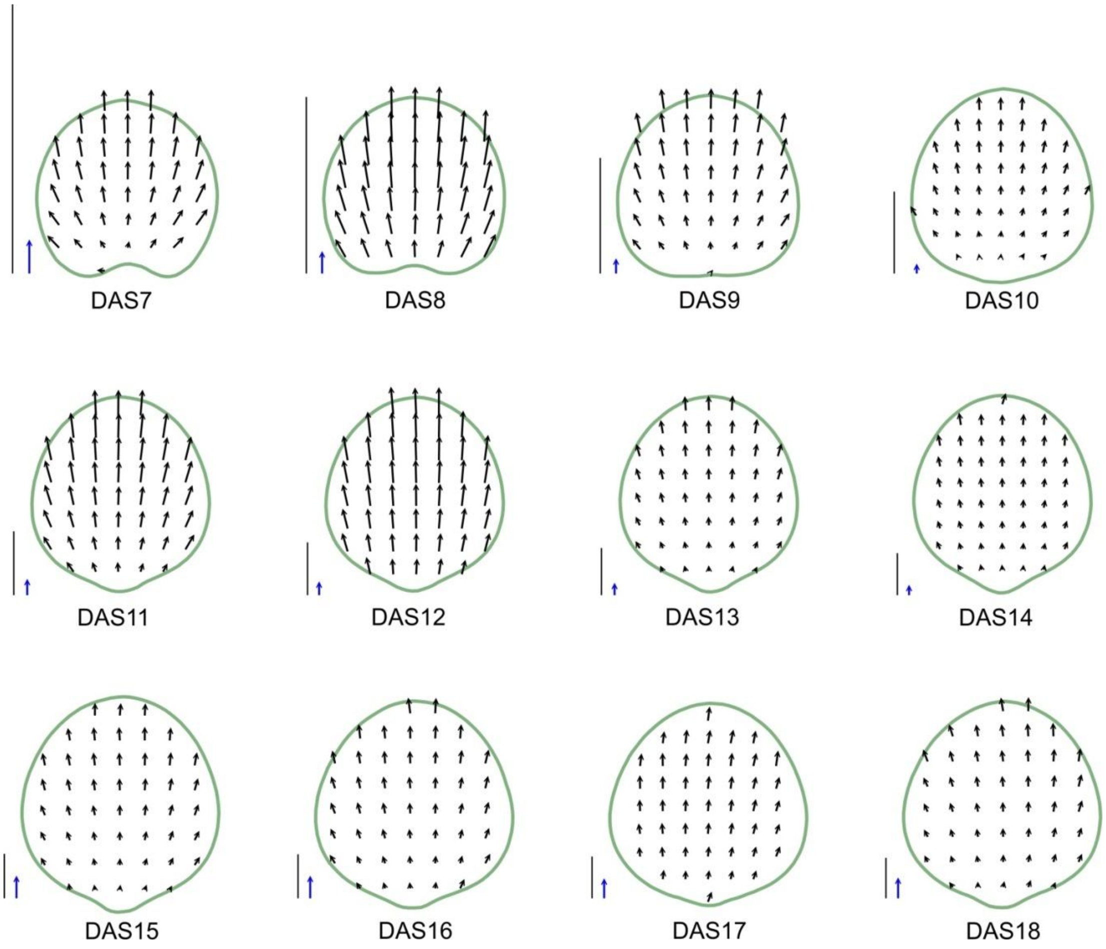

Figure 4.1: Mean velocity vectors of tissue displacement.

Velocity, measured from the petiole (the center of the leaf base) for DAS7-18. All maps are scaled to the same size for better visibility. Scale bars to the left of each map represent 1mm, and the blue arrows represent a velocity of 500µm day^{-1}. The mean leaf outlines and velocities are computed from N=12-22 samples at each time point.

Figure 4.2: Mean spatial maps of tissue displacement in the x (A), y (B), and z (C) axes. Units are in µm day^{-1}. x displacement is measured from the center, y displacement is measured from the leaf base, and z displacement is measured relative to the middle of the leaf.

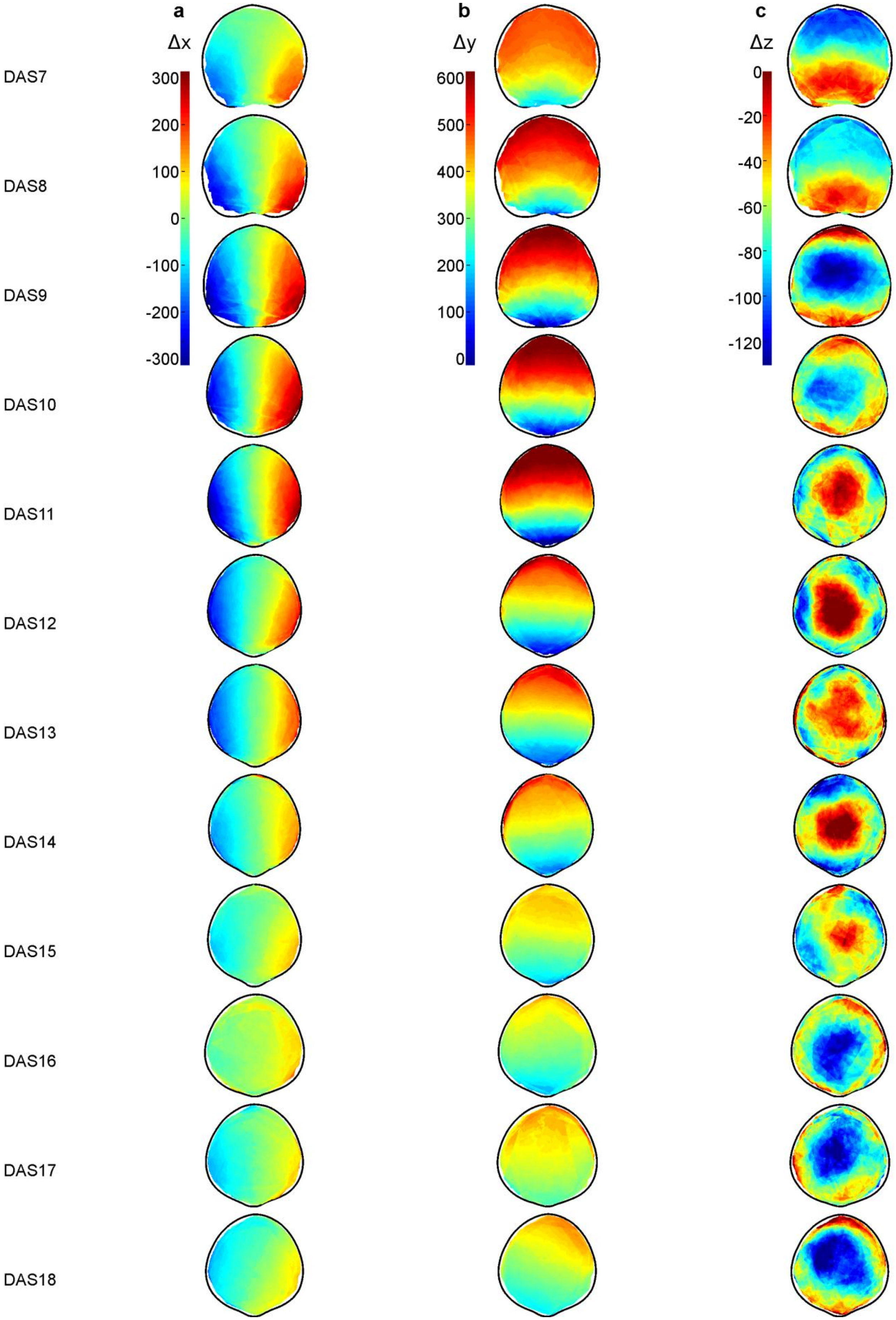
a
Δx
300
200
100
0
-100
-200
-300
b
Δy
600
500
400
300
200
100
0
c
Δz
0
-20
-40
-60
-80
-100
-120
DAS7
DAS8
DAS9
DAS10
DAS11
DAS12
DAS13
DAS14
DAS15
DAS16
DAS17
DAS18

4.3.2 Illustrating tissue movement through displacement of grid points

To illustrate movement of tissue in a way that can be more intuitively related to tissue growth parameters, we show the deformation of a grid. We make a mesh roughly in the shape of our leaf at the starting point (the mean DAS7 leaf outline), and then simulate growth by applying to each grid point the x y and z displacement values from the corresponding position on the mean displacement maps (see Supplemental Material for more information). The results for DAS7-12 are shown in Figure 4.3.

Squares at the base expand more than those at the tip, reflecting a proximodistal gradient in tissue expansion which is in agreement with relative growth rate patterns (Chapter 3 Figure 3.4). Tissue bends with a slightly upward curving shape, and, consistent with what we see in the mean y-displacement maps (Figure 4.2B), tissue near the leaf base moves outward more than tissue near the tip.

Unfortunately this tool does not allow us to show tissue deformation right to the leaf edges, since we do not have displacement data along the margins (see sample coverage maps of Chapter 3); this is more problematic for the leaf base, since tissue moves rapidly away from the base and by DAS11 the grid points are more than one-third of the way up the leaf. To show deformation of the whole leaf, or better yet, a full square grid across the leaf, would require extrapolation of the displacements beyond our sample coverage. This will be addressed in the following model.

4.3.3 Modeling growth deformations through warping

Using the displacement of all particles from all samples at each time point, we derive a polynomial transformation that describes the deformation of the leaf from one time point to the next. We fit a grid of square points to the leaf at the first time point (DAS7) and apply these transformations successively to the grid points. More details are provided in Supplemental Material. The results are shown in Figure 4.4, as well as in SVideo 3. Here we see a distinctive radial deformation of the leaf, with tissue bending in a slightly upward curving shape, and tissue near the leaf base moving outward more than tissue near the tip. The curvature of the grid deformation is more pronounced in the proximal parts of the leaf, and we again see a declining base to tip gradient in overall tissue expansion. By DAS19, tissue that was close to the base of the leaf at DAS7 has moved more than half-way up the leaf.

The major deformations appear to occur in earlier time points, particularly from DAS7 to DAS10. This can be better determined by looking at single-day grid deformations, produced by warping a square grid drawn on each mean leaf to the next time point only, to see how much deformation occurs in that period of growth alone. This is shown in Figure 4.5. We see substantial expansion and deformation in the growth from DAS7-8, 8-9, and 9-10, all with the upward-curving deformation, with tissue stretching outward more strongly at the base, and overall tissue expansion increasing from tip to base. Both deformation and expansion decrease over time, with deformation being hardly detectable after DAS11, and expansion being very minimal beyond DAS14. Qualitative and statistical assessment of these grid transformations can be found in the Methods section.

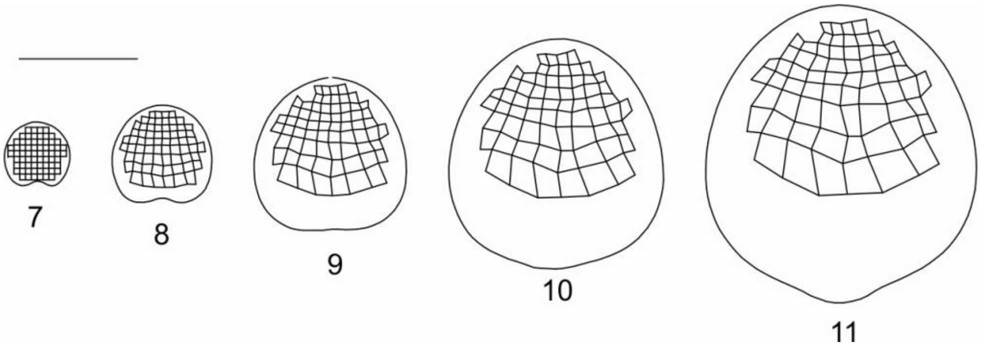

Figure 4.3: Simulation of tissue movement within a leaf over growth from DAS7 to DAS11, via displacements applied to grid points.

The displacements applied are obtained from mean displacement maps, computed from data of 12-20 leaf samples. Note that some grid points are deleted over time if their new position on the mean displacement maps was computed from fewer than 5 samples. Scale bar shows 1mm.

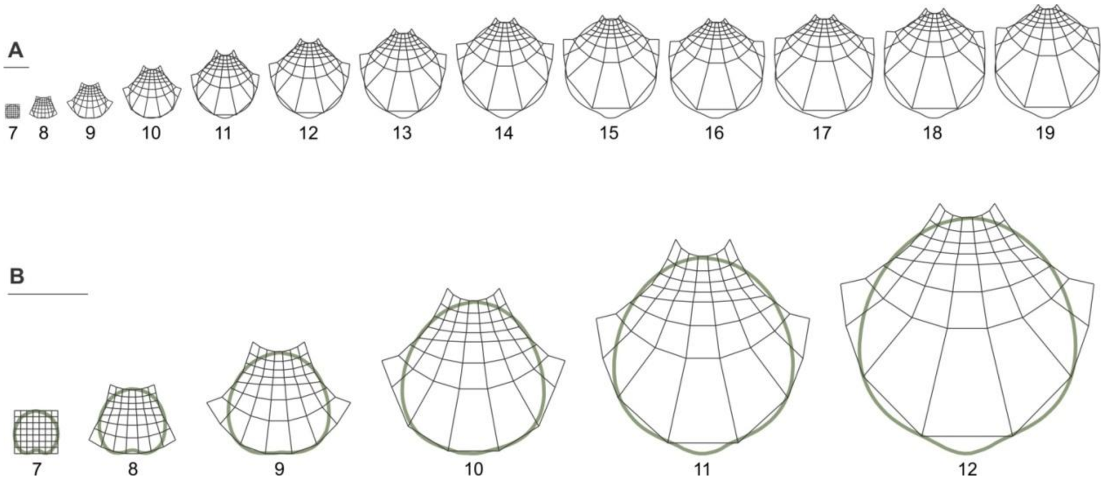

Figure 4.4: Polynomial transformation based simulation of tissue movement within a leaf.

Polynomial transformations are derived from the displacement of all particles (N=873-3374) from all leaf samples (N=12-22) for each time point to a grid fit across the mean DAS7 leaf. (A) shows the deformation over the course of all time points tracked,DAS7 to DAS19. The DAS7-12 grid point deformations magnified in (B). Scale bars represent 1mm.

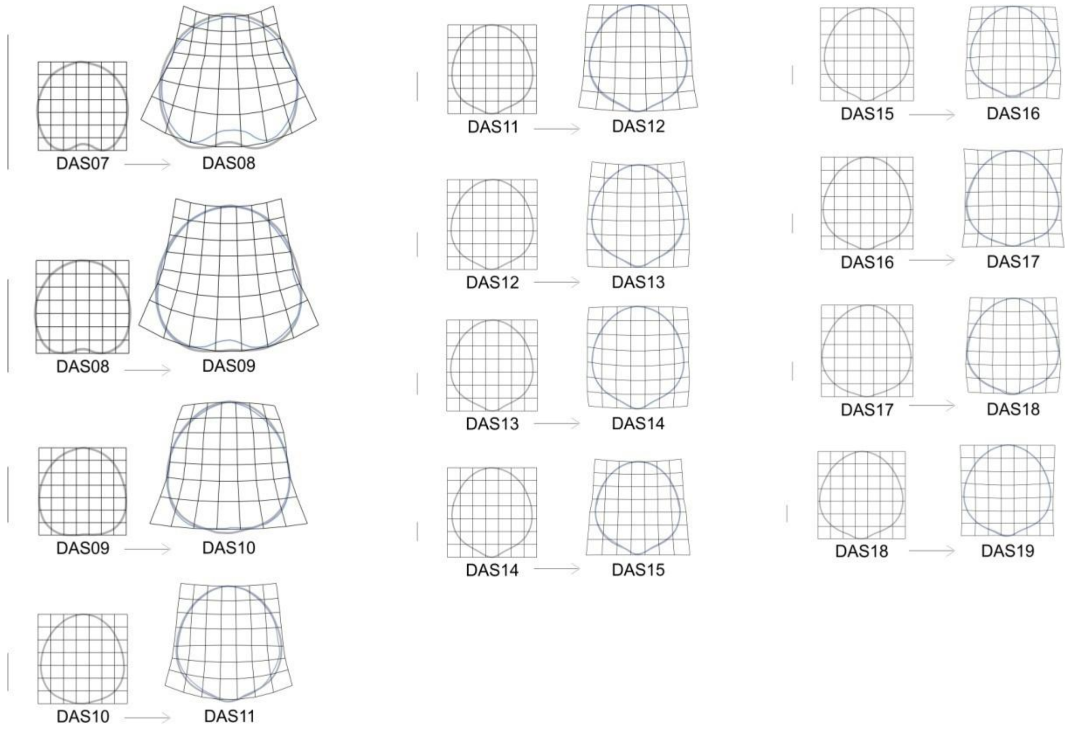

Figure 4.5: Single day grid deformations.

The deformation of a square grid over the course of 24 hours of growth for DAS7-18. The deformation is applied through a polynomial transformation derived from the displacement of all particles (N=873-3374) from all leaf samples (N=12-22) at that time point. Each pair of figures (i.e. before and after) is shown on the same scale, with scale bars to the left indicating 1mm. Blue lines show the deformed leaf outline.

4.3.4 3D leaf shape

Our new methodology for quantifying leaf growth involves an imaging system that produces for each leaf a multifocused image, a depth map, and focal plane information, from which we are able to reconstruct the leaf in 3D as a mesh surface (refer to Chapter 3); see Figure 4.6 or SVideo 4. In the following we present a tool which can be used to quantify leaf surface 3D shape from this data.

4.3.4.1 Leaf dimensions

We compute the dimensions of our leaf by making a line of 100 points along the middle of the leaf from the base to tip (longitudinal axis) for the leaf length, and across the broadest part of the leaf from side to side (transverse axis) for width. 2D length and width are computed from the 2D length of these lines. Using the surface mesh points we interpolate the z-coordinate of each point, and then compute 3D leaf length and width from the sum of the 3D lengths of all segments defined by points along the lines as depicted in Figure 4.6.

Both leaf length and leaf width are strongly correlated with leaf area, and thus serve as a reliable and more easily measured approximation of leaf size. Figure 4.7A shows the mean growth curve of the 3D leaf length and width over time. Both follow the same logarithmic curve, with the leaf being slightly smaller in length than in width. In both cases the variation in size increases over time and the size difference between successive days decreases.

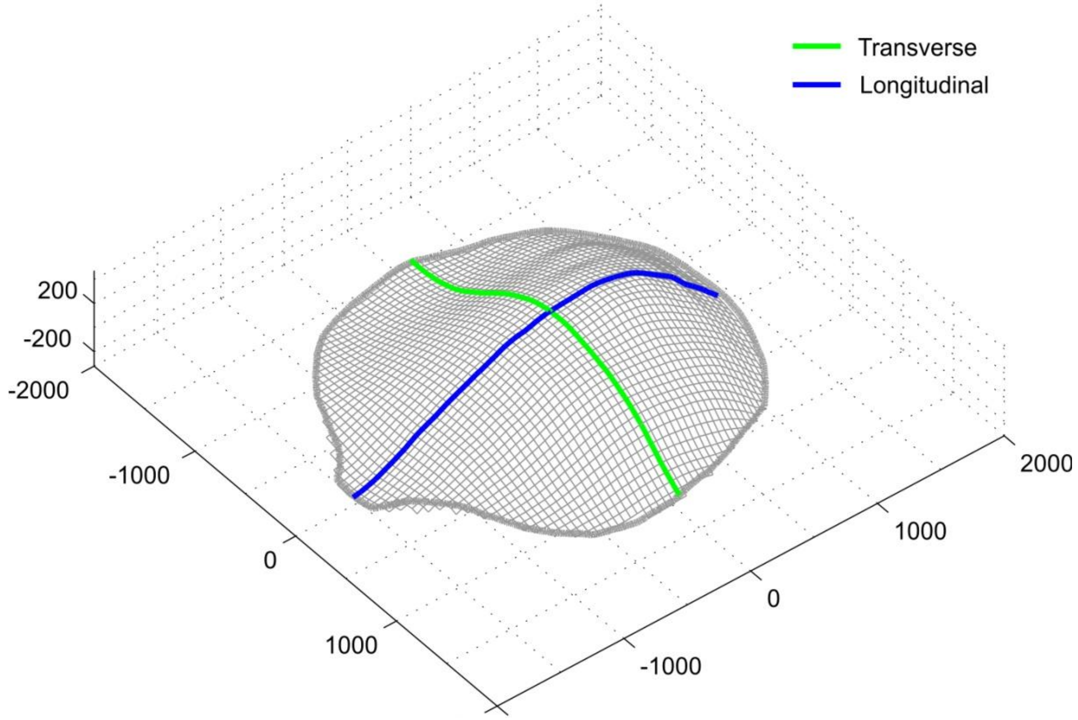

Figure 4.6: Transverse and longitudinal cross-sections of a 3D leaf mesh reconstruction.

Axis units are in µm. A DAS10 leaf is shown.

4.3.4.2 Leaf index over time

While size or area measurements of leaves can vary significantly within a species as a result of environmental or physiological factors, the length-width ratio usually remains fairly constant (Tsukaya, 2002). The ratio between the length and width of a leaf, sometimes referred to as the leaf index (LI), is thus a practical and often used measurement in studies of species classification and leaf shape analysis.

The 2D length-width ratios plotted in Figure 4.7B show a bell-shaped curve, with the LI around 1.0 for DAS7-9, increasing to approximately 1.12 over DAS10-14, then declining back to 1.06 by DAS19. This corresponds with the leaf shapes of our mean maps in which the leaf appears to be quite round from DAS7-9, then slightly elongated from DAS10-14, and then more rounded in the later time points.

We also plot the 3D length-width ratio in Figure 4.7B. The 3D LI remains relatively close to 1.0 over all days (mean leaf index for all DAS's of 0.975, SD 0.014). This would indicate that the leaf actually remains round throughout the developmental stages analyzed.

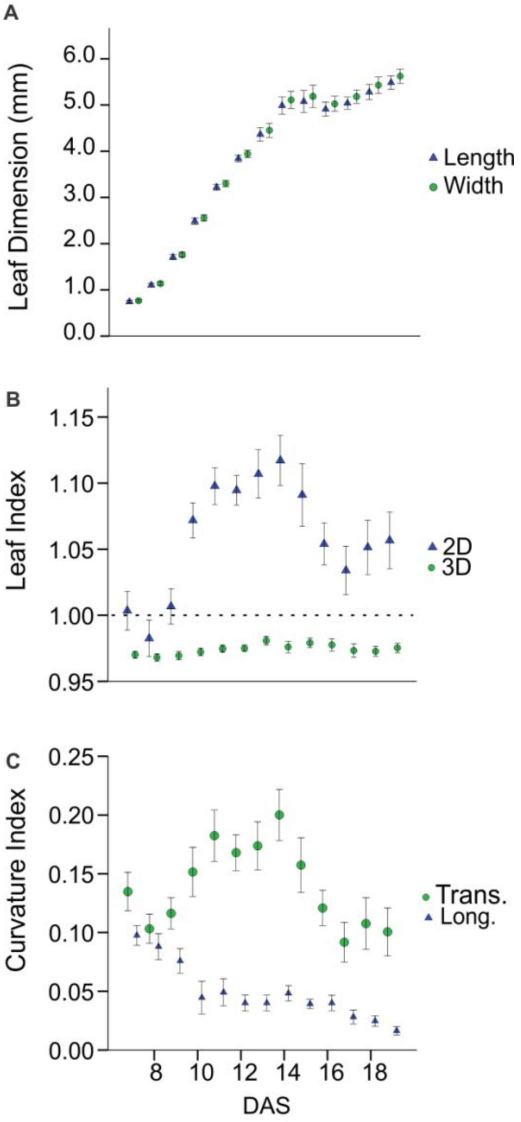

Figure 4.7: Leaf size, shape, and curvature over time.

(A) Mean 3D leaf length and width.

(B) Mean leaf index (length-to-width ratio) in 2D and 3D.

(C) Mean curvature index (CI), or 3D-to-2D ratio, along the longitudinal (Long.) and transverse (Trans.) axes of the leaves.

Error bars represent SE. N=12-34.

4.3.4.3 *Leaf curvature*

The discrepancy between the 2D and 3D leaf index is the result of leaf curvature. Although the leaves of wild type Arabidopsis are often considered to be relatively flat, a vast number of mutants with abnormally curved leaves can be found in the literature (e.g. White, 2006; Nath et al., 2003; Palatnik et al., 2003; Kee et al., 2009; Zhao et al., 2001), and in recent years, tools to thoroughly quantify 3D leaf shapes have been presented (Kaminuma et al., 2004; Liu et al., 2010). Our data allows us to also describe the 3D leaf shape, and how it varies over the course of development.

To illustrate the curvatures along the longitudinal (proximodistal) axis and transverse (mediolateral) axis of the leaf, we show the curvatures for all leaf samples in Figure 4.8; these are also represented in SVideo 5 and SVideo 6. We found that at some developmental stages the 3D shape varies too dramatically between samples for an average curvature to be valid. For example, at some points the curvatures of some leaves are concave while others are convex. This difference in orientation does not necessarily reflect dramatic differences in the physical structures of the leaves, since in either case, they can be inverted through manual manipulation. However, averaging the z-positions of these values would result in an unrealistically flat leaf, and due to spatial variation in leaf curvature, average z-values get smoothed out and are not representative of a typical leaf. For this same reason, we found that leaf curvatures are not well represented by polynomial functions (such as in Kaminuma et al., 2004). To assess the mean curvature along these two axes over time, we decided to use a curvature index CI based on the ratio between the 3D and 2D measurements, similar to the conventions of Wu et al. (2007) and Liu et al. (2010). We compute a leaf curvature along the transverse axis (CI_{trans}) and longitudinal axis (CI_{long}) as

$$CI_{trans} = \frac{\text{width3D} - \text{width2D}}{\text{width2D}}$$

$$CI_{long} = \frac{\text{length3D} - \text{length2D}}{\text{length2D}}$$

such that a CI of 0 represents complete flatness and increasing values represent increasing curvature.

The results are plotted in Figure 4.7C. Curvature along the proximodistal axis begins with a CI of 0.097 (SE 0.008) at DAS7 and declines to 0.016 (SE 0.003) by DAS19. From Figure 4.8 it appears the leaf is initially quite curved, then begins to flatten out from the leaf base. Mean curvature along the transverse axis follows a quadratic curve (y = -0.002x2 + 0.026x + 0.082, R^2 = 0.606), starting with a CI of 0.134 (SE 0.016) at DAS7 and increasing to a maximum of 0.200 (SE 0.022) at DAS14, then dropping back down to 0.100 (SE 0.020) at DAS19. From Figure 4.8 it appears that the increase in curvature from DAS7-13 corresponds to the rise of a bump along the midrib and slight curling along the leaf edges. The subsequent decline in leaf curvature seems to be the result of further blade expansion and flattening of the edges. This corresponds to the mean z displacement maps in Figure 4.2C which shows tissue rising in the center and lowering at the sides for DAS11-15.

This data tells us the typical leaf shape at different developmental stages, but, as seen in Figure 4.8 there is fair amount of variation in curvature in different leaf samples. Therefore, we also look at the change in curvature within individual samples over time. We computed total leaf curvature as

$$\mathrm{CI_{total}} = \frac{(\mathrm{width3D} + \mathrm{length3D}) - (\mathrm{width2D} + \mathrm{length2D})}{(\mathrm{width2D} + \mathrm{length2D})}$$

and found that while the curvature of all samples for any given DAS typically can have a wide range, the curvature of any given sample remains within a much tighter range over the time points followed (usually 6 days), and that it seems to fluctuate from higher to lower values on a daily phase. To better show this, we compute the relative curving rate (*rcr)* over time for each sample as

$$rcr(\mathrm{t}) = \frac{\mathrm{CI_{total}}(t+1)}{\mathrm{CI_{total}}(t)}.$$

This is plotted in Figure 4.9, with some data shifted by one DAS so that the fluctuations are synchronized .

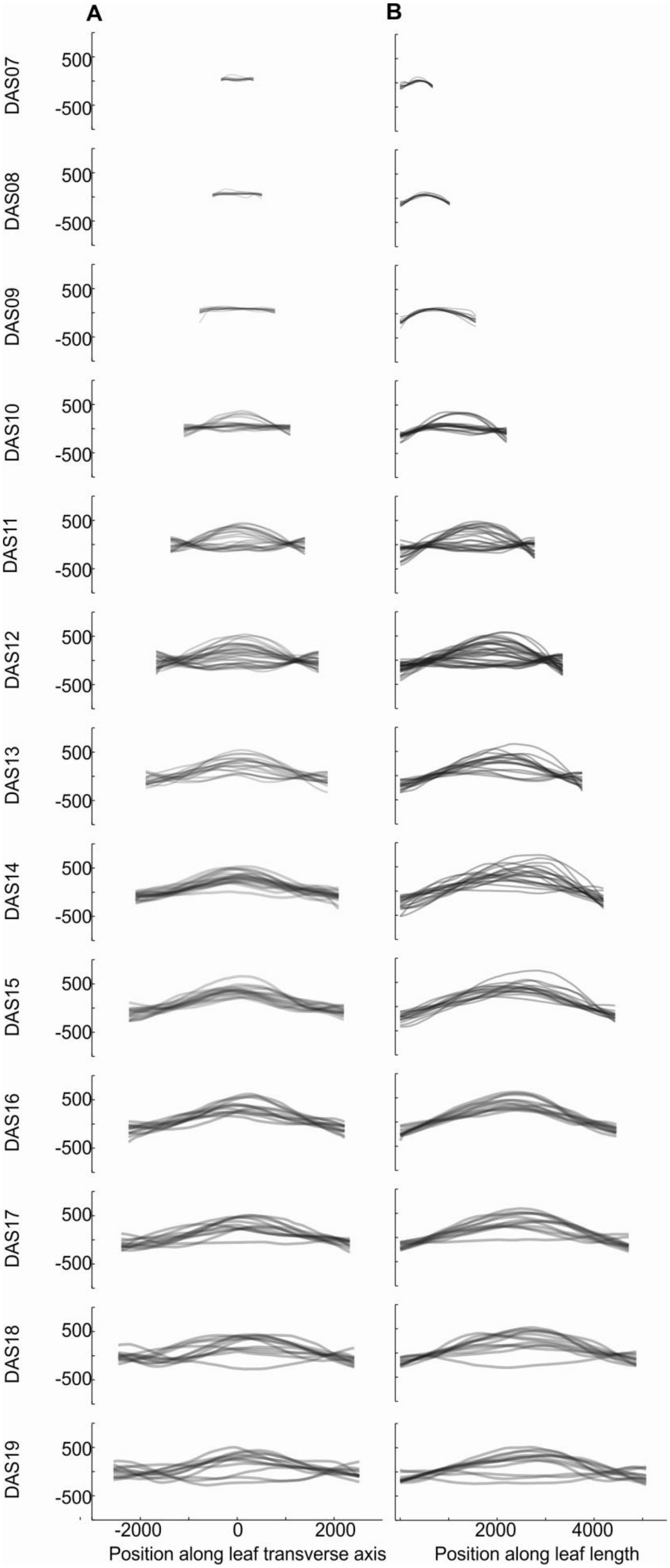

Figure 4.8: Transverse and longitudinal cross sections of all leaf samples at each DAS. Transverse (A) and longitudinal (B) cross sections are extracted as per the illustration in Figure 4.6. Each cross section was scaled to the mean 2D leaf width (A) or length (B) for its DAS. Lines are plotted with 60% transparency so that more frequent, overlapping curvatures are more visually dominant and outliers are less so. Axis units are in µm.

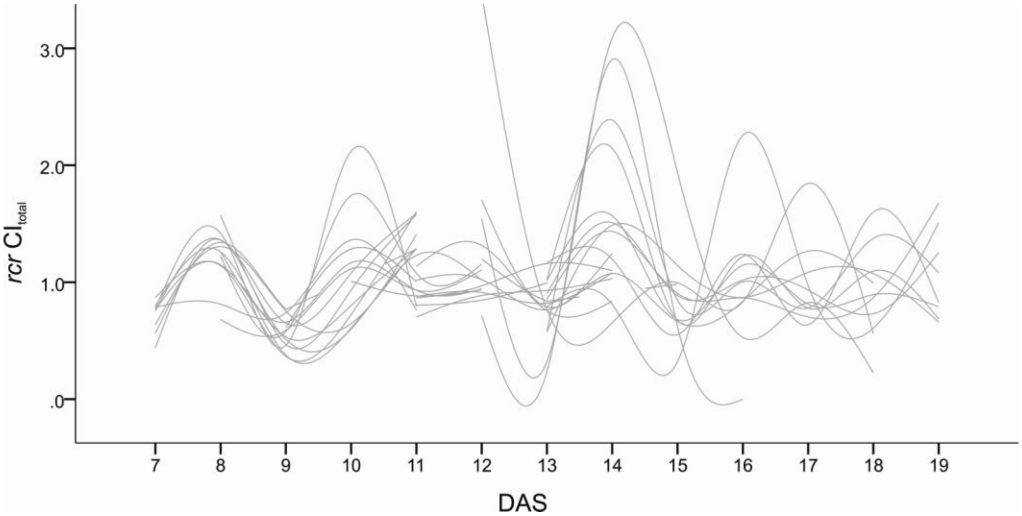

Figure 4.9: Relative change in leaf total curvature index of all leaf samples. Each sample is plotted with spline curves fit through all data points. Some samples were shifted by one DAS so that declining curvatures (CI rate <1) coincide with odd DAS's and vice versa, to align the phase of the CI fluctuations.

4.4 Discussion

4.4.1 Grid deformations are consistent with spatial growth patterns

The purpose of the grid deformations is to more clearly illustrate how tissue deforms during growth, but the results should fit with the patterns of other parameters of growth we measured. These include not only the tissue displacement but also the growth rates, growth anisotropy, direction of growth, and rotations of tissue (see Chapter 1, or refer to Goodall and Green (1986) or Coen et al. (2004)).

The grid cells closer to the leaf base expand more that those at the tip, which is consistent with the proximodistal gradient observed in our spatial maps of relative growth rates (Chapter 3 Figure 3.4). Tissue bends in a slightly upward and outward near the edges, which is consistent with the mean displacement and velocity vectors, and also agrees with our mean maps of anisotropy and growth orientation (Chapter 3 Figure 3.7A). These show that anisotropy is usually highest near the base and lower sides of the leaf; at the base this anisotropic expansion is usually in a horizontal orientation, while at the sides it tends to be angled towards the tip (i.e. the growth orientation points downward at the sides). However due to growth, the tissue at the sides rotates such that it bends upward at the sides (Chapter 3), which is reflected in the upward-curving shape of the grid deformations. The fact that we see the most significant deformation in the first few time points also fits with what we see in our growth maps. In the case of the relative growth rates, the gradient becomes less steep (Chapter 3 Figure 3.5A) in the proximodistal axis and less curved (Chapter 3 Figure 3.5D) in the transverse axis over time, and anisotropy becomes very low after the first few days (Chapter 3 Figure 3.7); this shows that growth becomes more homogenous across the leaf over time, which would explain why we see little deformation in the later time points.

4.4.2 The link between growth patterns and shape

The results produced in this grid deformation study are an excellent demonstration of how the interaction between spatial patterns in growth and the development of shape is not always intuitive.

Firstly, our 3D leaf measurement data show that there is little change in the dimensions of the leaf during the period of development analyzed; based on this alone one may have hypothesized that the leaf shape is laid out early in development and expands homogenously. Here we have shown that this may be true in later time points, but that there is actually significant deformation occurring in the earlier time points analyzed, particularly DAS7-10. The fact that the overall leaf shape remains similar throughout development despite significant deformation of the tissue shows that, in the case of the first rosette leaf in Arabidopsis, there is an intricate process that is responsible for maintaining a relatively constant leaf shape, despite dramatic deformation and spatial variation in growth patterns.

Secondly, our growth maps show an increasing tip-to-base gradient in the growth rates with a gradient front that is primarily downward curving in the early time points. We see in our grids the same increasing tip-to-base gradient in tissue expansion as we would expect. However, one may initially be surprised to discover that the leaf tissue actually deforms in a distinctly upward curving manner, contrary to the shape of the growth gradient. Upon further consideration one will realize that there is no reason to assume that the deformation and growth patterns would necessarily have the same shape, possibly due to unmeasured mechanical constraints (for example, adhesion between cells or rigidity of marginal cells in different parts of the leaf), as well as spatial differences in anisotropy and directionality of growth. Ultimately, there are a number of factors that would influence the resulting grid deformation, making it difficult to predict without the use of computational modeling. In this case it seems that although growth rates are higher in tissue at the center of the leaf, the way that this tissue expands causes leaf tissue to be pushed upward and outward to more lateral positions of the leaf. Thus, although central regions of the leaf may expand faster due to higher growth rates, the lateral regions are compensated by the addition of new tissue due to tissue displacement.

4.4.3 Quantifying tissue deformation is important for proper analysis of shape mutants

The link between growth and shape has been considered before in the context of mutant plants with spatial heterogeneities in growth. One might expect that if central areas of the leaf were expanding more than the lateral areas, this would lead to a curvature in the transverse axis; for example consider the Arabidopsis *peapod* mutant, which has abnormal dome-shaped leaves, due to presumed excess expansion of the lamina but limited expansion of the perimeter (White, 2006). On the other hand, if the lateral areas were growing faster than the central regions of the leaf, the leaf edges could become droopy or curled with excess tissue; one might consider the *Antirrhinum cincinnata* mutant for example, whose crinkled leaf shape has been linked to excess marginal growth (Nath et al., 2003).

Based on the above example, we might expect that the downward curvature of the growth gradient would be responsible for the establishment of a stronger transverse curvature in the leaf, because at any point along the proximodistal axis of the leaf, the sides of the leaf grow slower than the center. The straightening and slight upward curving shape of the growth gradient at later stages would then coincide with a flattening of the leaf.

However, curvature measurements indicate that the leaf remains relatively flat throughout development, and that curvature fluctuates in ways that seem unrelated to the shape of the growth rate gradient.

When considering not only growth rates but also tissue displacement, we can see that although lateral regions grow slower than central regions, tissue in lateral positions gets pushed upwards. This must therefore compensate for the slower growth rate, and maintains a relatively flat leaf shape.

Our study on the link between growth patterns and grid deformations therefore shows that one should be cautious of linking simple measurements of growth patterns to shapes. A measurement of expansion alone is not a full description of growth (nor are measurements of cell division, which do not necessarily even necessarily reflect growth) and is not sufficient to explain 3D changes in shape.

4.4.4 Future directions

The most obvious future application of this method will be to compare leaf shape and growth deformations between wild type and mutant plants in combination with our method for quantifying spatial growth patterns. In doing so, we will be better able to understand the connection between differences in growth patterns and the resulting shape differences. This tool will also help to identify at which developmental stage the leaf shapes of two variants begin to diverge. If we reset the grid at this time point, the differences in the transformations from this point onward will reflect the differences in growth deformations, which can provide clues on the underlying molecular mechanisms giving rise to the shape differences.

As noted previously, the Arabidopsis leaf has a relative simple shape that does not change significantly over development, yet we still see a surprisingly significant deformation of the tissue. In addition to mutant plants, it may also be interesting to quantify grid deformations in plant species with more complex leaf morphologies that undergo more dramatic shape changes over development.

The grid deformations presented here are essentially simulations of leaf growth. Instead of modeling growth deformation of a grid by applying mean displacement values to grid point coordinates, we could instead apply growth transformations to small regions delineated by grid points (based on values from our mean growth parameter maps presented in Chapter 3). This would allow us to test specific hypotheses by investigating the effects of altering these parameters and comparing the results to known mutant phenotypes. For example, would decreasing anisotropy produce the characteristically narrow leaves seen in *angustifolia* mutants? Or is this phenotype better represented when anisotropy remains the same but the orientation of growth has been altered?

Finally, the computational tools presented here could easily be adapted to show grid deformations for any form of tracked landmark data, including 3D volumetric deformations.

4.4.5 Conclusion

While growth patterns may help uncover the underlying morphogen actions in development, we cannot simply link the patterns of growth to shape outcomes, as there are physical constraints that dictate how tissue will be displaced within the organ and thus how these growth properties will affect the final shape. The grid deformations we have presented here provide a key piece of information necessary to understand the link between growth and shape.

4.5 Computational details

4.5.1 Illustrating tissue movement through displacement of grid points

The pseudo-algorithm for this procedure is shown below, in Text Box 1.

First we first fit a grid across the mean leaf outline of the first time point (DAS7) and store these coordinates as *GP*. To find the coordinates corresponding to GP on the mean maps, we shift and scale the *GP* coordinates based on the difference between the width of the leaf outline and the width of the map (refer to explanation of maps in Chapter 2). Now for each *GP* grid point, we take the values from the corresponding position on the mean maps of x-, y-, and z-displacement, and add these to the x, y, z coordinates of the grid point. This gives us the deformed coordinates of the grid at the next time point.

We repeat this procedure on these new grid point coordinates using the displacement map data for the next time point

Should a grid point come to a position on the mean maps that was computed from fewer than five samples (see sample number maps in Chapter 3 SFigure 3.2), the point is discarded from the grid at the next time point. This is due to the fact that the grid deformations we show are meant to represent the average deformation, from many leaf samples (N=12-22), but some areas of the mean maps (mainly near the edges) are not covered by all samples. We found that the displacements applied to grid points in these areas sometimes led to grid deformations that are not consistent with the mean leaf shape.

```
Make a square grid of points across the mean 2D leaf shape for day t=1. We will store these
grid points in GP{t=1}.

FOR day t=1 to t=end-1

Load the day t grid points (GP{t}).

Make another set of grid points by scaling and shifting the GP{t} coordinates to the day t
to obtain corresponding grid point positions on the spatial map. We will store these
coordinates in Gm.

Load the day t spatial maps of mean x-, y-, and z- displacement (dx{t}, dy{t}, and dz{t})
and sample numbers (N{t})

FOR each grid point in GP{t}

   Use the Gm coordinate to retrieve the value from the corresponding position of N{t}

   IF the number of samples at that point is >4

      Use the Gm coordinate to retrieve the value from the corresponding position of dx{t},
      dy{t}, and dz{t}, and add these to the x-, y-, and z-coordinates of the grid point.
      This gives the coordinates of the grid point at the next time point, and is stored as
      GP{t+1}.

   ENDIF

ENDFOR

ENDFOR
```

Text Box 1: Psuedo-algorithm for simulating grid deformation of a leaf by applying mean displacement values to grid points.

4.5.2 Modelling growth through polynomial transformations

The pseudo-algorithm for this procedure can be found below, in Text Box 2.

For the first DAS, we fit a square grid of points across the average 2D leaf shape. We then load the particle coordinates from all leaves that have data for this time point, *t*, along with all of the corresponding particles at the next time point, *t+1.* In both cases, we warp the coordinates to the mean leaf shape of their respective DAS using the method explained in (Chapter 3). We use the Matlab built-in *cp2tform* function to compute a third-order polynomial transformation based on the change in particle coordinates between the two time points; this transformation describes the mean leaf deformation. Using the built-in *tformfwd* function, we apply this transformation to the grid coordinates to produce the deformation of the grid from *t* to *t+1*.

We also apply the transformation to the mean leaf outline to obtain the corresponding deformation of the leaf shape at the next time point, and to the particle coordinates to project their positions at the next time point. The difference between warped outline and real leaf outline at time t+1, and the difference between warped particle coordinates and true particle coordinates at time t+1 can both be used to analyze the accuracy of the method (see section 4.5.3).

We repeat the warping procedure for all of the following time points. In the case of the single-day deformations, we redraw the square grid on each DAS and warp those coordinates once only. For the cumulative grid deformation, we store the new coordinates of the grid after each deformation, and successively apply the transformations to the deformed coordinates.

```
    Make a square grid of points across the mean 2D leaf shape for day t=1. These grid
    coordinates will be stored in G{t=1}.

FOR day t=1 to t=end-1

   FOR each leaf that contains data for day t to t+1

      Load the matched bead coordinates on the leaf at day t and t+1. Coordinates are
      warped to the mean leaf shape of their respective DAS

      Concatenate the coordinates of the beads at day t into a list, B1. B1 will contain
      coordinates of all beads on all leaves at day t

      Concatenate the coordinates of the beads at day t+1 into a list, B2. B2 will
      contain coordinates of the same beads at the next time point. I.e. each bead has
      the same row number in both lists.

   ENDFOR

   Load the coordinates of the grid at day t

   Divide the leaf into two sections, horizontally (top half and bottom half)

   FOR each section

      Find all rows of B1 containing coordinates that lie in that section. Store the
      beach coordinates from these rows in B1S

      Using cp2tform, derive a 3rd-order polynomial transformation that describes the
      deformation from day t to t+1 based on the displacement of all beads lying in that
      section, B1S to B2S.

      Apply this transformation to any day t grid points that lie within this section to
      project the coordinates of the grid at day t+1. Store in G{t+1}.

      Apply this transformation to any day t outline points that lie within this section
      to get the deformed outline at day t+1. Store in LW{t+1}.

      Apply this transformation to the day t B1s beads to project the coordinates at day
      t+1. Store in B1W.

   ENDFOR

   Make the grid symmetrical across the mediolateral axis of the leaf

   Scale the deformed leaf outline LW{t+1}, grid points G{t+1}, and beads B1W to the
   mean leaf outline, based on the difference between the sides or tip of the real mean
   leaf outline and the projected LW{t+1} outline

   Compute the root mean square error (rmsd) by comparing the warped B1W coordinates to
   the actual bead coordinates in B2.

   IF any grid points have been warped outside the mean leaf outline

      Adjust the coordinate of the grid point so that it cannot go outside the outline

   ENDIF

ENDFOR
```

Text box 2: Psuedo-algorithm for modelling growth through polynomial transformations derived from the displacement of particles over time.

4.5.3 *Assessment and adjustments of the grid transformations*

We can make a qualitative judgment about the accuracy of the grid deformations by successively applying each of the transformations to the leaf outline, and comparing the resulting warped leaf outlines to the real mean leaf outlines. SFigure 4.1A-B shows the final accumulated error of warping the DAS7 outline through to DAS19. It seems to fit the mean outline fairly well (see caption for explanation of base), except that it gives a slightly pointy leaf tip. We know there are spatial patterns in the growth parameters, and so different areas of the leaf are deforming differently. Therefore, computing and applying a separate transformation for different parts of the leaf will allow the transformations to fit the data better.

In SFigure 4.1C we show the resulting grid and outline deformation produced from two separate transformations, one for the top half and another for the bottom half of the leaf; this leads to an improvement in the leaf tip shape. Dividing the leaf into more than two sections for warping does not seem to further improve the grid deformation (SFigure 4.1D); therefore, we used two transformations only.

The accuracy of the grid deformations can also be assessed quantitatively. By applying the transformations we computed for the grid deformations at each time point to all of the particle coordinates at that time point, we obtain theoretical positions of those particles at the next time point, t+1. We can correlate the accuracy of the grid deformations by measuring how well these theoretical t+1 particle coordinates match the actual coordinates of the same particles at t+1. This is done by computing the root mean square distance (*rmsd*), given by

$$rmsd = \sqrt{\frac{\sum d^2}{N}}$$

where *d* is the 2D distance between the warped and actual coordinate of a particle, and N is the number of particles. This is conceptually similar to standard deviation.

The *rmsd*'s of two separate transformations are consistently lower than the *rmsd*s of a single transformation (STable 4.1) by a small amount (1-2μm). Dividing the leaf into more than two sections for warping had almost no effect on the *rmsd*.

We also warped the mean leaf outline of each DAS in our single day deformations (Figure 4.5); here we see that from one day to the next the discrepancies are very small or undetectable, which indicates that the difference between the mean DAS19 leaf outline and the final deformation of the DAS7 outline results from the accumulation of smaller errors over time. In order to offset these errors, we perform three additional modifications to the resulting warped grid point coordinates at each time step.

First, we scale the grid points according to the difference between the warped outline and the mean outline at the sides or tip (not the base, since we know our warped outline moves up the leaf due to the fact that the outline we see in later stages is not visible at the leaf base in the early time points when the leaves are first emerging); we use whichever difference is smaller, so as not to push points outside of the actual outline. This improves the fit around the edges, although it actually increases the *rmsd* by a very small amount in some cases (2µm on average). The reason for this is likely due to the fact that the particle coordinates used to compute the transformations are less dense around the leaf edges, and so the transformation will be biased toward accommodating the deformation of inner regions. This scaling procedure likely improves the *rmsd* at the outer edges, which is important for obtaining the proper shape.

We also make the grid points symmetric across the mediolateral axis, as we know that Arabisopsis leaves are symmetric. If we take all of the grid points on the left half of the leaf and mirror them onto the right half, and vice versa, each half of the leaf now has a set of two corresponding grid points. Our symmetric grid coordinates are computed from the average of each corresponding pair of grid points.

Lastly, we found that the transformation would sometimes result in grid points that are below the leaf outline to become further below the leaf outline. This is because there are no data in this area (i.e. there are no particles outside of the leaf outline) from which to compute exactly how these points would move. However, reality dictates that it is not possible for tissue to move outside of the leaf margin and so we do not allow points to move outside of the leaf outline.

With these modifications, the *rmsd* for each growth deformation ranges from 75µm to 223µm with a mean of 148µm across all DAS's. In interpreting this, one should keep in mind that the leaf size also increases over time, from a mean width of 765µm at DAS7 to 5624µm at DAS1; thus, relative to the leaf size the *rmsd* actually decreases. However, since our deformations are applied continuously to one grid from the first time point to the last, the error is cumulative; the accumulated *rmsd* at DAS19 is 1781µm.

4.6 Supplemental figures and data

SFigure 4.1: Cumulative error of the deformations using three different methods of warping.

(A) The mean DAS7 outline and the initial square grid. In (B-C), the mean DAS7 outline deformed to DAS19 remains the same colour of blue, and the actual mean DAS19 outline is in black.

(B) How the mean leaf outline and a square grid of points across the leaf at DAS7 will be deformed over the course of development to DAS19, using one transformation for the whole leaf at each time point, and no scaling adjustments.

(C) How the mean leaf outline and a square grid of points across the leaf at DAS7 will be deformed over the course of development to DAS19 with two separate transformations applied at each time point – one for grid points in the top half of the leaf, and one for grid points in the bottom half of the leaf - and the scaling adjustment.

(D) How the mean leaf outline and a square grid of points across the leaf at DAS7 will be deformed over the course of development to DAS19 with three separate transformations applied at each time point, for the lower, middle, and top thirds of the leaf.

Note that the fact that the lower portion of the deformed outline in (B-C) curves upward at the center instead of downward is not unexpected, since our starting mean leaf outline at DAS7 has this same indentation (A) due to the fact that the petiole was not traced in the DAS7 outline as it was not yet visible. The lower portion of the deformed outline is also far above the real mean DAS19 outline, but this again is not surprising since we cannot see the entire base of the DAS7 leaf and we know that the tissue moves distally as it grows.

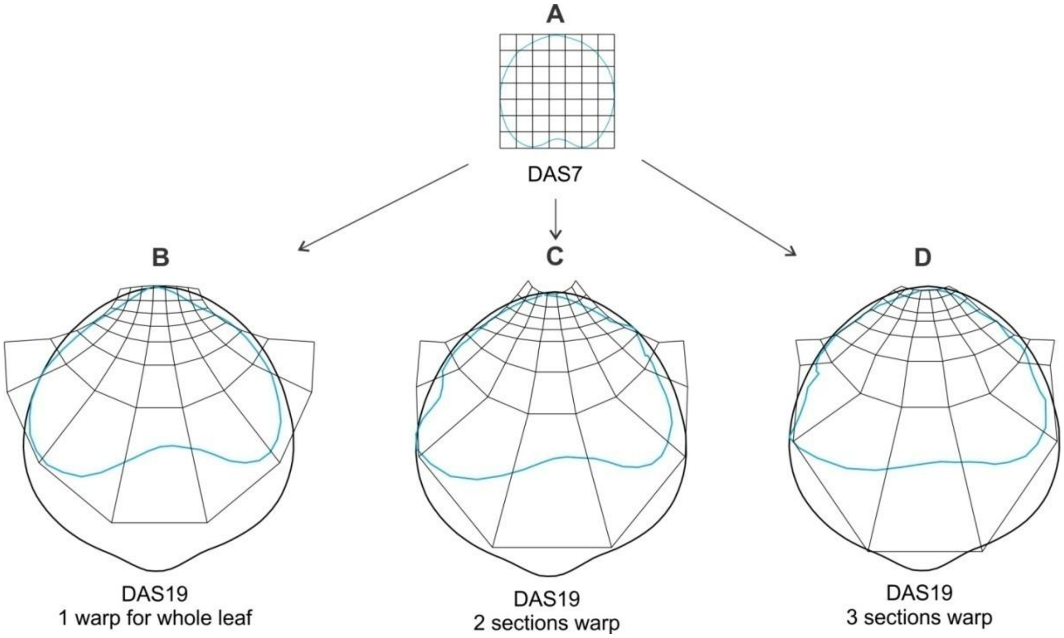
A
DAS7
B
C
D
DAS19
1 warp for whole leaf
DAS19
2 sections warp
DAS19
3 sections warp

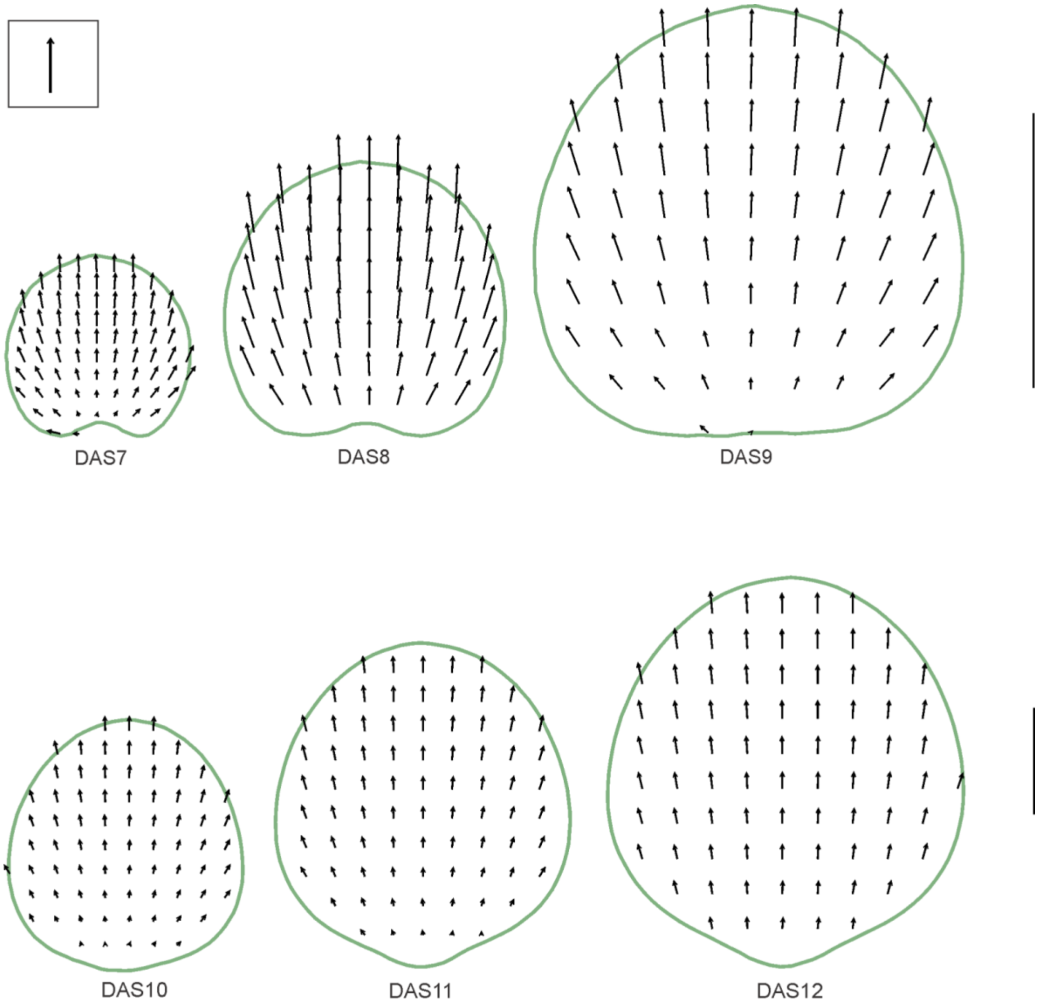

SFigure 4.2: Mean velocity vectors for DAS7-12, with each row on the same scale and velocity vectors on the same scale.

The arrow vector in the box represents 1000μm day^{-1}, and the scale bars at the right represent 1000μm.

DAS	**Number of leaf samples**	**Total number of particles tracked**	***rmsd***			**Cumulative *rmsd***		
			Single transformation	Two separate transformations	Two separate transformations and scaling	Single transformation	Two separate transformations	Two separate transformations and scaling
7	13	873	75	74	75	75	74	75
8	13	1039	79	78	81	154	152	156
9	13	1179	99	96	99	253	248	255
10	18	2115	150	148	148	402	396	403
11	22	2806	163	162	162	565	558	565
12	18	3324	166	166	167	731	724	732
13	18	3374	147	147	147	878	870	879
14	16	2773	222	222	223	1100	1092	1102
15	12	2071	149	149	154	1250	1241	1256
16	12	2057	154	154	157	1404	1395	1413

STable 4.1: *rmsd* and cumulative *rmsd* of grid deformations.

rmsd and cumulative *rmsd* of warping from one time point to the next based on the change in particle coordinates over time, in the making of the grid deformations, using three different methods (refer to
SFigure 4.2).

Chapter 5: General discussion and conclusions

5.1 Global summary of thesis projects

In this thesis we have presented a number of novel computational tools as well as a new method for computing 3D shape changes and growth in developing leaves.

The project began by adapting existing software to make it possible to quantify leaf surface growth from 3D coordinates of vein branching points, as part of another project on the quantification of vein patterning in leaves (Assaf et al., in prep). The method made it possible to relate vein patterning to growth (Assaf et al., in prep), and was used as a foundation for the main project of this thesis, which involved the development of a new technique for quantifying leaf growth using topically applied microscopic fluorescent particles.

Tracking growth using fluorescent particles has several advantages over the tracking of vein branching points: vein branching points occur in relatively low densities, and tracking vein branching points requires transgenic plants with fluorescent vasculature. On the other hand, fluorescent particles can be applied to the leaf surface of any plant, and in any desired concentration, providing high spatial resolution. The high number of beads to be tracked led us to develop algorithms to semi-automate particle identification and tracking. There are commercial image analysis software packages that can be used to identify particles, but their use is not flexible, and we needed a unique particle-tracking algorithm, as the points we track change position significantly over time, with a spatially irregular displacement.

Once the techniques and tools were developed, we proceeded to apply it to a data set of wild type leaves to validate the method. The results from the wild type leaf shape study were in themselves interesting, revealing new information about leaf growth. Aside from showing a proximodistal gradient in growth, which is consistent with what has been observed in other leaf growth studies, it also showed that this gradient becomes less steep in the proximodistal axis over time, and that this gradient has a distinctively downward curving shape in early time points but becomes straighter over time. This latter observation might support the idea that growth is controlled by a growth promoting substance from the leaf base at early time points that later interacts with an inhibiting signal originating from the leaf tip. The data showed patterns in growth directionality, and also revealed differences in the patterns of the scaling factors in the directions of maximal and minimal expansion, which supports existing hypotheses that they may be controlled by different mechanisms.

As we analyzed the results we questioned whether the data could reveal information about how tissue growth attributes are set and controlled. For example, does the direction of anisotropic growth remain in the same orientation locally within tissue as the leaf grows? In answering such questions we realized it would be helpful to show the displacement of tissue during growth, so that we could follow the changes (or consistency) in growth parameters within specific regions of tissue over time as they moved throughout the leaf.

This ultimately led to the idea of showing movement of tissue within the leaf through the deformation of a grid. These grids also showed important information about how tissue deforms over the course of development, which we realized could be related to the 3D shape of the leaf, and thus set out to quantify that as well. The grid deformations show that tissue deforms in an upward and outward manner, in contrast to the downward curving shape of the relative growth gradient front, and that leaf curvature fluctuates within a small range. This seems to demonstrate that the lower growth rates of lateral regions of the leaf are counterbalanced by the addition of new tissue due to tissue displacement, and the leaf thus remains relatively flat throughout development.

Results illustrated that although there are significant spatial heterogeneities in growth patterns and significant deformation of the leaf tissue, especially at early developmental stages, the overall leaf shape remains similar throughout the developmental period analyzed. This brings the thesis project full-circle, by illustrating the importance of quantifying growth in early stages, and the importance of quantifying growth and deformation in leaf shape mutants, as the link is not always clear or intuitive.

5.2 Future studies

The results generated from this study will be very useful for assessing the processes that result in different leaf phenotypes. We, and other researcher who follow our method, can proceed to study numerous interesting leaf growth subjects, from mutant plants with altered growth, effects growth hormones, or the impact of various environmental conditions. A few examples are discussed below.

5.2.1 Hormones

There are several phytohormones that are well-known to play an important role in leaf development, including auxin, brassionsteroids, cytokinins and gibberellins. However the connection between growth patterns and hormone concentrations, distributions, and transportation within the leaf is not clear. This can be investigated by quantifying and analyzing leaf growth patterns in various hormone mutant phenotypes, in plants grown with exogenous hormones, or in leaves with localized exogenous hormone applications (see Figure 5.1A-B).

Auxins: The first obvious hormone candidate to link to growth patterns would be auxin, which has been demonstrated to have a central role in growth of many organs, including leaves. However, it is unknown exactly how auxin affects leaf growth or where its sites of synthesis are within the leaf. On one hand, auxin has been temporally associated with more rapidly expanding leaves and spatially correlated with sites of higher rates of cell division (Ljung et al., 2001). Topical auxin treatments have also been shown to increase adaxial leaf growth (Keller, 2007), and stimulate leaf blade outgrowth (Koenig et al., 2009). On the other hand, various auxin over-producing mutants display small epinastic leaves (Zhao et al., 2001; Fujino et al., 2008; Boerjan et al., 1995), and topical application of auxin to the leaf surface has also been shown to cause growth inhibition (Keller, 2007). As (Koenig et al., 2009) stated, controlled local application of auxin to developing leaves is necessary to determine the direct relationship between hormone and morphological outcome. Quantifying growth pattern disruptions across a leaf following localized exogenous auxin applications (as in Figure 5.1) could be helpful in proposing a possible mechanism of its effects on leaf growth and development.

Brassinosteroids: Another class of plant hormones which would be interesting to link to leaf growth patterns and leaf shape are brassinosteroids. These are a more recently identified group of phytohormones that are becoming increasingly recognized as important regulators of growth and development. This is clearly illustrated in brassinosteroid defective mutants, which display slow growth rates, and small, rounded leaves (Choe et al., 1998). Two recent studies have indicated that the role of brassinosteroids in controlling leaf shape and size is complex and tissue-specific. One shows that brassinosteroid presence in the epidermis may be important for regulating overall growth and final size, but not shape (Savaldi-Goldstein et al., 2007), while the other shows that brassinosteroid expression in the leaf margin is essential for proper leaf shape development, but not size (Reinhardt et al., 2007). This latter finding is interesting given the expression of the auxin-inducible reporter construct DR5::GUS that has been observed in the leaf margin (Aloni et al., 2003), which has been assume to represent important sites of auxin sources. However, DR5 can also be induced by brassinosteroids (Nakamura et al., 2003). It is possible that brassinosteroid expression and localization may play a more important role, in conjunction with auxin, than previously thought. Precisely how its interplay with auxin sources in the leaf margin and localization within the leaf regulate leaf morphogenesis has yet to be determined. Thus, quantifying growth patterns in brassinosteroid mutants, as well as in leaves with local applications of exogenous brassinosteroids, and combinations thereof, may bring important insights in the control of leaf size and shape by this hormone.

5.2.2 Mutant analysis

This method will be useful to researchers interested in investigating the role of various gene products in leaf morphogenesis, by providing a link between molecular data and growth patterning. Once published, the software presented here will be available to other researchers interested in using this method to support molecular, genetic, and anatomical studies. There is a vast array of leaf shape mutants that would be interesting to study. For example, the recently identified *KLUH* mutant displays smaller leaf organs, perhaps through a role on the timing of growth arrest (Anastasiou et al., 2007b). Quantitative analysis of the growth of *KLUH* leaves would make it possible to test this hypothesis. It would also be interesting to quantify growth in the *cincinnata* (Nath et al., 2003) and *PEAPOD* (White, 2006) mutants, which have ruffled and dome-shaped leaves, respectively, to validate the assumptions about the differences in leaf growth and the resulting 3D shape change.

Figure 5.1: Possible effects of localized hormone applications on growth patterns.

(A-B) In a pilot study, we applied a lanolin paste mixed with synthetic auxin (10mg NAA per g) to the leaves of young plants (A). 24hrs after application the leaves are severely epinastically curled (B). This shows that auxin does indeed affect leaf growth and morphology, although this auxin concentration is too severe and would need to be optimized in future work.

(C-H) Illustrating possible growth pattern disruptions that localized hormone applications may have. Note that these are just a few of many possible outcomes, and these show effects on growth rates only, yet hormones could just as likely disturb leaf shape through disruptions to anisotropy or signals that orient growth direction.

(C) The wild type growth pattern.

(D) Local application of a hormone to the side of a leaf causes a local gradient of growth radiating from the site of application, possibly suggesting that the hormone plays a role in promoting growth.

(E) Distal application of a hormone changes the proximodistal growth gradient, possibly suggesting that the hormone has disrupted a natural morphogen gradient.

(F) Local application of a hormone to the side of a leaf causes a localized increase in growth and an outgrowth of the leaf at the site of application, possibly suggesting that the hormone plays a role in promoting growth by creating a local gradient.

(G) Distal application of a hormone changes the shape of growth gradient, possibly suggesting that the hormone plays a role in inhibiting growth, or in sensitizing different regions of the leaf (medial versus lateral) to a growth inhibiting signal.

(H) Local application of a hormone to the side of a leaf causes a change in the growth gradient along that side of the leaf, possibly suggesting that the hormone levels are important for growth and the hormone diffuses from base to tip.

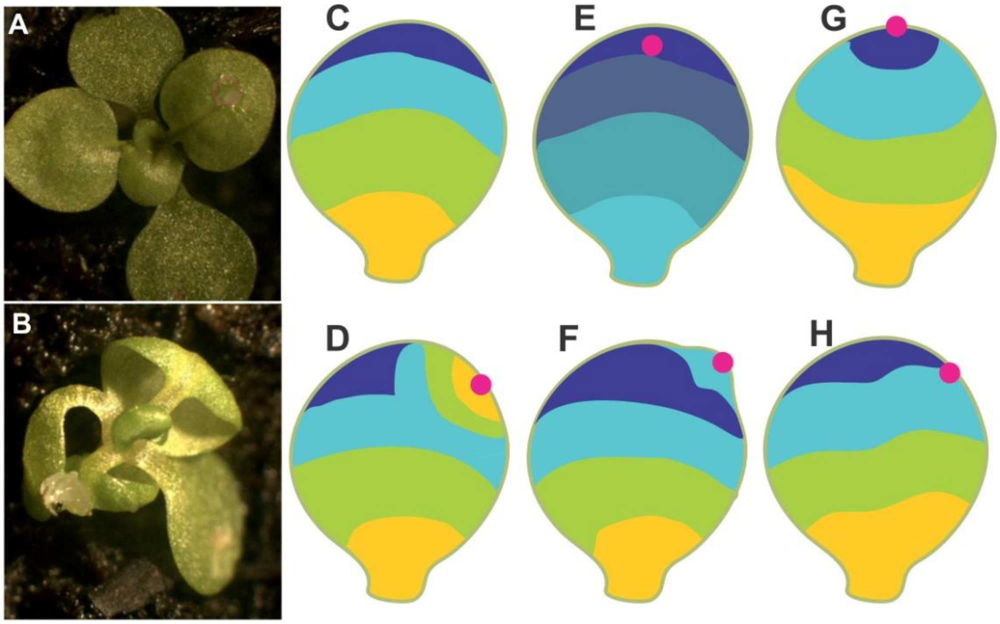

5.2.3 *Leaf wounding responses*

Plants are frequently exposed to mechanical wounding from physical environmental forces such as wind and rain, as well as herbivory by animals and insects. Such wounding not only damages the plant tissue and increases risk to pathogenic infection, but also decreases plant growth and organ size (Zhang and Turner, 2008). This concept is applied in pruning of bushes or trees to control their size, seen most exaggeratedly in the ornamental bonsai, which is miniaturized to 5% of its usual size by frequent trimming. Despite its consequences in reducing plant growth in crops and its deliberate application in horticulture, the basis of the effect is not well understood (Zhang and Turner, 2008). Studies on the effect of the wound response in young leaves that have not fully developed have not, to our knowledge, been published.

A pilot study where leaves were wounded by puncturing a small hole in with needle at a very young stage of growth shows that this causes a noticeable difference in the shape of the mature leaf (Figure 5.2), in a manner that seems to be dependent on the position of the wound (Szymanski et al., unpublished). Quantifying the growth patterns of wounded leaves may help uncover how growth patterns are altered around the wound, and would therefore provide some insights into how the wound affects morphogen gradients, what kind of response originates from the wound site, and how it influences the growth and morphology of the leaf.

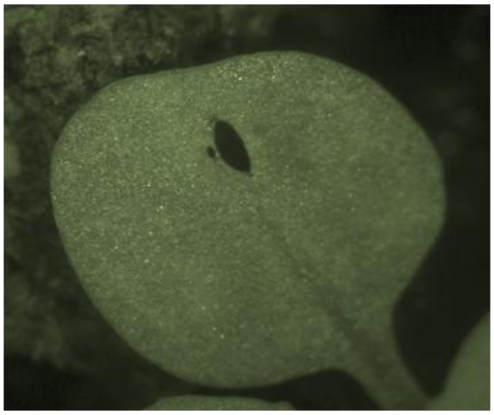

Figure 5.2: Pilot study of leaf wounding. A DAS17 leaf, one week after puncturing a small hole in the lamina, shows an asymmetric difference in leaf growth.

5.2.4 *Environmental conditions*

Crop species are frequently exposed to environmental conditions, such as salinity, heat stress, cold stress, and drought, that detrimentally affect their growth. Various mutants and hormones are known to increase or decrease tolerances to these conditions, but the mechanisms remain unclear. For example, characterizing growth patterns in plants grown in reduced watering conditions with exogenous brassinosteroid could shed light on how these hormones increase tolerance to drought conditions (Kagale et al., 2007).

5.2.5 Interaction between growth and vein patterning

In Chapter 3 we found that growth parameters differed along paths that appeared to coincide with likely positions of primary and secondary veins. As our lab also has methods for quantifying vein patterning *in vivo* by tracking fluorescent veins of transgenic plants (Assaf et al., in prep), growth could be monitored at a high spatial resolution at and around veins using a concentrated particle solution. This would make it possible to see whether there are localized growth patterns in rates or directions of growth that coincide with vein development. We could also further explore the apparent similarities between tissue growth anisotropy and vein loop elongation, and tissue growth direction and loop orientation (as noted in Chapter 2).

Since auxin plays an important role in both leaf vascular development and growth, it would also be interesting to investigate both of these processes using the same combination of techniques, under conditions of increased or decreased auxin levels or localized auxin applications.

5.2.6 Ecotype and species comparisons

The techniques and tools presented in Chapter 3 provide a quick way to quantify growth patterns, which could be applied to a variety of plant species, to identify the various growth patterns that give rise to various types of leaf shapes.

Soybean leaves are an interesting candidate. The proximodistal gradient of growth seems to be a common feature of leaf growth, having been observed in virtually all plant species that have been studied, except soybeans (Ainsworth et al., 2005). It would be interesting to quantify growth in soybean leaves with our method at earlier time points, to see whether this is in fact true. If it is, we could apply our method to identify more species lacking this growth gradient, which will provide additional data which molecular biologists can use to further investigate the underlying cause of this difference.

5.2.7 Modeling leaf development

Computational morphodynamics research is a new and important field in developmental biology, which seeks to understand morphogenesis through an integration of live imaging, image processing, and computational modeling. As reviewed by Chickarmane et al. (2010), such models are useful for visualizing and exploring the complex and multi-faceted processes of development, and allow researchers to test and generate hypotheses about mechanisms driving growth. Our results provide data that could be used to develop or optimize leaf morphogenesis models that realistically represent growth processes.

We could also use a combination of our growth data and grid deformations to model growth, and along with other morphogen modelling software (Rolland-Lagan, in prep) to further investigate the apparent straightening of the growth gradient shape; i.e. could this be a result of an interaction between a growth promoting morphogen from the leaf tip which later interacts with a growth inhibiting morphogen originating from the leaf base, and/or does tissue deformation itself play a role in changing the shape of the gradient? It would also be interesting to explore through simulation modeling if the oscillations in leaf curvature are linked to growth patterns, or circadian rhythms (e.g. see Edwards and Millar, 2007).

5.3 Other applications of the method

Many aspects of the methodologies we presented here could be used together or independently for other studies.

In theory, the method could be applied to any growing surface that can be imaged under the microscope, from organs, to cells, to bacterial colonies, to non-living materials studied in the physical sciences. The use of the particles is, however, limited to surfaces to which the particles adhere and are not disturbed during growth, although, it may be possible to obtain a particle with a ligand that will bind it to the tissue in question, or to use a line in which a fluorescent marker is expressed in certain cell types that are distributed across the surface (in this case the software will simply be tracking cells or clusters of cells instead of particles). Thus the tracking and growth computing software could be used or adapted to follow fluorescent particles or other distinguishable markers on any growing tissue.

The z-stack acquisition and 3D surface reconstruction software could be used to quantify shapes, dimensions, and curvatures of any 3D surface, along with tools we developed for computing the mean lengths and widths, and mean 3D shapes and mean proximodistal and mediolateral curvatures (not presented) from several samples. This could be useful for evaluating changes in morphology over the course of development, or as a way to quantify, compare, and/or classify shape phenotypes of any organ(ism)s that can be viewed as a 3D surface.

Finally, the software we developed for computing growth and deformation could be used to compute growth parameters from 3D data generated from other methods.

5.4 Broader relevance of results

The results of our study are not limited to understanding the mechanisms of morphogenesis in Arabidopsis leaves. As mentioned previously, the same spatial and temporal trends we observed in the Arabidopsis leaf have been demonstrated in the leaves of other species, which suggests that the mechanisms of growth discovered in Arabidopsis may translate to other economically important species. The relevance of studying growth in Arabidopsis is also supported by the fact that several genes and hormones that increase growth in Arabidopsis have been shown to also promote growth in crop species such as potato, tomato, and rice (as reviewed in Gonzalez et al., 2009).

Also, as many lateral plant organs, such as bracts, spines, petals, stamens, and sepals, are actually modified leaves, one would assume that they are under control of similar growth mechanisms. Indeed, many mutant leaf phenotypes are reported to exhibit the same effect on petals (e.g. *an1* and *rot3* (Tsuge et al., 1996)*, KLUH* (Anastasiou et al., 2007a)*, ARL* (Hu et al., 2006)). So, mechanisms of leaf morphogenesis may also be involved in the development of other plant organs.

Finally, as Donnelly (1999) observes, similarities between leaf phenotypes in Arabidopsis mutants and organ phenotypes in mutants of other model organisms, such as *Drosophila* wings for example, suggests that there may be commonalities in the mechanisms of organogenesis across species in the plant and animal kingdoms.

5.5 Final words

The results of applying our new methods and tools for quantifying growth and shape to the first rosette leaf of *A. thaliana* reveal clear spatiotemporal patterns in growth rates and directionality. Grid deformations of tissue movement illustrate the outcome of these growth patterns on leaf shape, which furthermore allows us to relate growth data to 3D shape changes.

The methods we present fill a void in the current selection of techniques available for quantifying leaf growth. The most exclusive features are the capability to track growth in very small leaves, and to quantify growth from 3D-coordinates. The former makes this method capable of tracking leaf growth from much earlier stages of development than has previously been possible, when major shape and growth changes are occurring. The latter makes it the first method suitable for tracking growth in species and mutants with 3-dimensional (curved, curled, ruffled) leaf surfaces.

Most of the results shown in this thesis are novel approaches to answering scientific questions, and may be useful as a guideline for computing, displaying, and analysing other kinds of spatial data in the future. A particularly significant feature of our software is the capability to produce high resolution spatial maps of growth patterns from a large number of samples; this will be essential for making quantitative comparisons of leaf growth between mutant and wild type plants, plants grown in different environmental conditions, or plants of different ecotypes, etc.

The results of future studies such as these will provide a link between molecular data and morphogenesis, and help uncover spatial and temporal control of gene products, which could ultimately lead to bio-engineering of crops with higher yields, faster growth rates, or better environmental tolerance. Future application of the methods presented will shed more light on the controls of leaf development, and in doing so, lead to a better understanding of the fascinating process of morphogenesis in general.

Literature Cited

Ainsworth E, Walter A, Schurr U (2005) Glycine max leaflets lack a base-tip gradient in growth rate. J Plant Res 5: 343-346

Aloni R, Schwalm K, Langhans M, Ullrich C (2003) Gradual shifts in sites of free-auxin production during leaf-primordium development and their role in vascular differentiation and leaf morphogenesis in Arabidopsis. Planta 216: 841-853

Anastasiou E, Kenz S, Gerstung M, MacLean D, Timmer J, Fleck C, Lenhard M (2007) Control of plant organ size by KLUH/CYP78A5-dependent intercellular signaling. Dev Cell 13: 843-856

Arthur W (2006) D'Arcy Thompson and the theory of transformations. Nat Rev Genet 7: 401-406

Avery GS,Jr. (1933) Structure and development of the tobacco leaf. Am J Bot 20: 565-592

Backhaus A, Kuwabara A, Bauch M, Monk N, Sanguinetti G, Fleming A (2010) LEAFPROCESSOR: a new leaf phenotyping tool using contour bending energy and shape cluster analysis. New Phytol 187: 251-261

Baskin TI (2005) Anisotropic expansion of the plant cell wall. Annu Rev Cell Dev Biol 21: 203-222

Bernd J (1997) Digital Image Analysis. Springer, New York

Boerjan W, Cervera MT, Delarue M, Beeckman T, Dewitte W, Bellini C, Caboche M, Onckelen HV, Montagu MV, Inze D (1995) superroot, a recessive mutation in Arabidopsis, confers auxin overproduction. Plant Cell 7: 1405-1419

Bohn S, Andreotti B, Douady S, Munzinger J, Couder Y (2002) Constitutive property of the local organization of leaf venation networks. Phys Rev E 65: 061914

Bylesjo M, Segura V, Soolanayakanahally RY, Rae AM, Trygg J, Gustafsson P, Jansson S, Street NR (2008) LAMINA: a tool for rapid quantification of leaf size and shape parameters. BMC Plant Biol 8: 82

Chehab EW, Eich E, Braam J (2009) Thigmomorphogenesis: a complex plant response to mechano-stimulation. J Exp Bot 60: 43-56

Chickarmane V, Roeder AH, Tarr PT, Cunha A, Tobin C, Meyerowitz EM (2010) Computational morphodynamics: a modeling framework to understand plant growth. Annu Rev Plant Biol 61: 65-87

Christ MM (2005) Temporal and spatial patterns of growth and photosynthesis in leaves of dicotyledonous plants under long-term CO2- and O3-exposure. PhD thesis. Heinrich Heine University Düsseldorf, Düsseldorf

Coen E, Rolland-Lagan A, Matthews M, Bangham JA, Prusinkiewicz P (2004) The genetics of geometry. P Natl Acad Sci USA 101: 4728-4735

Corson F, Adda-Bedia M, Boudaoud A (2009) In silico leaf venation networks: Growth and reorganization driven by mechanical forces. J Theor Biol 259: 440-448

Cosgrove DJ (2005) Growth of the plant cell wall. Nat Rev Mol Cell Biol 6: 850-861

Cronk Q (2009) The molecular organography of plants. Oxford University Press, Oxford

Donnelly PM, Bonetta D, Tsukaya H, Dengler RE, Dengler NG (1999) Cell cycling and cell enlargement in developing leaves of Arabidopsis. Dev Biol 215: 407-419

Edwards KD, Millar AJ (2007) Analysis of circadian leaf movement rhythms in Arabidopsis thaliana. Methods Mol Biol 362: 103-113

Erickson RO (1966) Relative elemental rates and anisotropy of growth in area: a computer programme. J Exp Bot 17: 390-403

Fujino K, Matsuda Y, Ozawa K, Nishimura T, Koshiba T, Fraaije MW, Sekiguchi H (2008) NARROW LEAF 7 controls leaf shape mediated by auxin in rice. Molec Genet Genomics 279: 499-507

Gonzalez N, Beemster GT, Inzé D (2009) David and Goliath: what can the tiny weed Arabidopsis teach us to improve biomass production in crops? Curr Opin Plant Biol 12: 157-164

Goodall CR, Green PB (1986) Quantitative analysis of surface growth. Bot Gaz 147: 1-15

Granier C, Tardieu F (1998) Spatial and temporal analyses of expansion and cell cycle in sunflower leaves . A common pattern of development for all zones of a leaf and different leaves of a plant. Plant Physiol 116: 991-1001

Hamant O, Heisler MG, Jönsson H, Krupinski P, Uyttewaal M, Bokov P, Corson F, Sahlin P, Boudaoud A, Meyerowitz EM, Couder Y, Traas J (2008) Developmental Patterning by Mechanical Signals in Arabidopsis. Science 322: 1650-1655

Hu Y, Poh HM, Chua N (2006) The Arabidopsis ARGOS-LIKE gene regulates cell expansion during organ growth. Plant J 47: 1-9

Jenks MA, Rashotte AM, Tuttle HA, Feldmann KA (1996) mutants in *Arabidopsis thaliana* altered in epicuticular wax and leaf morphology. Plant Physiol 110: 377-385

Kagale S, Divi U, Krochko J, Keller W, Krishna P (2007) Brassinosteroid confers tolerance in *Arabidopsis thaliana* and *Brassica napus* to a range of abiotic stresses. Planta 225: 353-364

Kaminuma E, Heida N, Tsumoto Y, Yamamoto N, Goto N, Okamoto N, Konagaya A, Matsui M, Toyoda T (2004) Automatic quantification of morphological traits via three-dimensional measurement of Arabidopsis. Plant J 38: 358-365

Kazama T, Ichihashi Y, Murata S, Tsukaya H (2010) The mechanism of cell cycle arrest front progression explained by a KLUH/CYP78A5-dependent mobile growth factor in developing leaves of *Arabidopsis thaliana*. Plant Cell Phys 51: 1046-1054

Kee J, Jun SE, Baek S, Lee T, Cho MR, Hwang H, Lee S, Kim J, Kim G, Im K (2009) Overexpression of the downward leaf curling (DLC) gene from melon changes leaf morphology by controlling cell size and shape in Arabidopsis leaves. Mol Cell 28: 93-98

Keller CP (2007) Leaf expansion in Phaseolus: transient auxin-induced growth increase. Physiol Plant 130: 580-589

Kennaway R, Coen E, Green A, Bangham A (2011) Generation of diverse biological forms through combinatorial interactions between tissue polarity and growth. PLoS Comput Biol 7: e1002071

Koenig D, Bayer E, Kang J, Kuhlemeier C, Sinha N (2009) Auxin patterns Solanum lycopersicum leaf morphogenesis. Development 136: 2997-3006

Langlade NB, Feng X, Dransfield T, Copsey L, Hanna AI, Thébaud C, Bangham A, Hudson A, Coen E (2005) Evolution through genetically controlled allometry space. P Natl Acad Sci USA 102: 10221-10226

Liu Z, Jia L, Mao Y, He Y (2010) Classification and quantification of leaf curvature. J Exp Bot 61: 2757-2767

Ljung K, Bhalerao RP, Sandberg G (2001) Sites and homeostatic control of auxin biosynthesis in Arabidopsis during vegetative growth. Plant J 28: 465-474

Maksymowych R (1962) An Analysis of Leaf Elongation in Xanthium pensylvanicum Presented in Relative Elemental Rates. Am J Bot 49: pp. 7-13

Maksymowych R (1959) Quantitative Analysis of Leaf Development in Xanthium pensylvanicum. Am J Bot 46: pp. 635-644

Massonnet C, Vile D, Fabre J, Hannah MA, Caldana C, Lisec J, Beemster GTS, Meyer RC, Messerli G, Gronlund JT, Perkovic J, Wigmore E, May S, Bevan MW, Meyer C, Rubio-Díaz S, Weigel D, Micol JL, Buchanan-Wollaston V, Fiorani F, Walsh S, Rinn B, Gruissem W, Hilson P, Hennig L, Willmitzer L, Granier C (2010) Probing the reproducibility of leaf growth and molecular phenotypes: A comparison of three arabidopsis accessions cultivated in ten laboratories. Plant Phys 152: 2142-2157

McConnell JR, Barton MK (1998) Leaf polarity and meristem formation in Arabidopsis. Development 125: 2935-2942

Micol JL (2009) Leaf development: time to turn over a new leaf? Curr Opin Plant Biol 12: 9-16

Nakamura A, Higuchi K, Goda H, Fujiwara MT, Sawa S, Koshiba T, Shimada Y, Yoshida S (2003) Brassinolide induces IAA5, IAA19, and DR5, a synthetic auxin response element in Arabidopsis, implying a cross talk point of brassinosteroid and auxin signaling. Plant Physiol 133: 1843-1853

Nath U, Crawford BCW, Carpenter R, Coen E (2003) Genetic control of surface curvature. Science 299: 1404-1407

Ntziachristos V (2010) Going deeper than microscopy: the optical imaging frontier in biology. Nat Meth 7: 603-614

Palatnik JF, Allen E, Wu X, Schommer C, Schwab R, Carrington JC, Weigel D (2003) Control of leaf morphogenesis by microRNAs. Nature 425: 257-263

Piazza P, Jasinski S, Tsiantis M (2005) Evolution of leaf developmental mechanisms. New Phytol 167: 693-710

Poethig R,S., Sussex I,M. (1985) The developmental morphology and growth dynamics of the tobacco leaf. Planta 165:158-169

Reinhardt B, Hanggi E, Muller S, Bauch M, Wyrzykowska J, Kerstetter R, Poethig S, Fleming A (2007) Restoration of DWF4 expression to the leaf margin of a dwf4 mutant is sufficient to restore leaf shape but not size: the role of the margin in leaf development. Plant J 52: 1094-1104

Richards OW, Kavanagh AJ (1943) The analysis of the relative growth gradients and changing form of growing organisms: Illustrated by the tobacco leaf. Am Nat 77: 385-399

Rolland-Lagan A, Amin M, Pakulska M (2009) Quantifying leaf venation patterns: two-dimensional maps. Plant J 57: 195-205

Saurer W, Possingham JV (1970) Studies on the growth of spinach leaves (*Spinacea oleracea*). J Exp Bot 21: 151-158

Savaldi-Goldstein S, Peto C, Chory J (2007) The epidermis both drives and restricts plant shoot growth. Nature 446: 199-202

Scarpella E, Marcos D, Friml J, Berleth T (2006) Control of leaf vascular patterning by polar auxin transport. Genes Dev 20: 1015-1027

Schmundt D, Stitt M, Jähne B, Schurr U (1998) Quantitative analysis of the local rates of growth of dicot leaves at a high temporal and spatial resolution, using image sequence analysis. Plant J 16: 505-514

Seber GAF (2008) Cluster analysis: Multivariate observations. John Wiley & Sons, Inc., pp 347-394

Strutt D (2005) Organ shape: Controlling oriented cell division. Cur Biol 15: R758-R759

Tardieu F, Granier C (2000) Quantitative analysis of cell division in leaves: methods, developmental patterns and effects of environmental conditions. Plant Mol Biol 43: 555-567

Taylor G, Tricker PJ, Zhang FZ, Alston VJ, Miglietta F, Kuzminsky E (2003) Spatial and temporal effects of free-air CO2 Enrichment (POPFACE) on Leaf growth, cell expansion, and cell production in a closed canopy of poplar. Plant Phys 131: 177-185

The Arabidopsis Genome Initiative (2000) Analysis of the genome sequence of the flowering plant Arabidopsis thaliana. Nature 408: 796-815

Thompson DW (1917) On growth and form. Cambridge University Press, Cambridge

Tsuge T, Tsukaya H, Uchimiya H (1996) Two independent and polarized processes of cell elongation regulate leaf blade expansion in Arabidopsis thaliana (L.) Heynh. Development 122: 1589-1600

Tsukaya H (2006) Mechanism of leaf-shape determination. Ann Rev Plant Biol 57: 477-496

Tsukaya H (2002) The leaf index: Heteroblasty, natural variation, and the genetic control of polar processes of leaf expansion. Plant Cell Phys 43: 372-378

Walter A, Roggatz U, Schurr U (2003) Expansion kinematics are an intrinsic property of leaf development and are scaled from cell to leaf level at different nutrient availabilities. Plant Biol 5: 642-650

Walter A, Schurr U (1999) The modular character of growth in *Nicotiana tabacum* plants under steady-state nutrition. J Exp Bot 50: 1169-1177

Walter A, Silk WK, Schurr U (2009) Environmental effects on spatial and temporal patterns of leaf and root growth. Ann Rev Plant Biol 60: 279-304

Wang L, Beyer ST, Cronk QC, Walus K (2011) Delivering high-resolution landmarks using inkjet micropatterning for spatial monitoring of leaf expansion. Plant Meth 7: 1

Weight C, Parnham D, Waites R (2008) LeafAnalyser: a computational method for rapid and large-scale analyses of leaf shape variation. Plant J 53: 578-586

White D (2006) PEAPOD regulates lamina size and curvature in Arabidopsis. Proc Natl Acad Sci USA 103: 13238-13243

Widjanarko T, Hardie RC (2002) A post-processing technique for extending depth of focus in conventional optical microscopy. Optics Laser Tech 34: 299-305

Wiese A, Christ MM, Virnich O, Schurr U, Walter A (2007) Spatio-temporal leaf growth patterns of Arabidopsis thaliana and evidence for sugar control of the diel leaf growth cycle. New Phytol 174: 752-761

Wolf SD, Silk WK, Plant RE (1986) Quantitative patterns of leaf expansion: Comparison of normal and malformed leaf growth in *Vitis vinifera* cv. *Ruby Red*. Am J Bot 73: 832-846

Wu F, Yu L, Cao W, Mao Y, Liu Z, He Y (2007) The N-Terminal double-stranded RNA binding domains of Arabidopsis HYPONASTIC LEAVES1 are sufficient for pre-microRNA processing. Plant Cell 19: 914-925

Zar JH (1996) Biostatistical Analysis, Third Edition. Prentice Hall, New Jersey, pp 591-614

Zhang Y, Turner JG (2008) Wound-induced endogenous jasmonates stunt plant growth by inhibiting mitosis. PLoS ONE 3: e3699

Zhao Y, Christensen SK, Fankhauser C, Cashman JR, Cohen JD, Weigel D, Chory J (2001) A role for flavin monooxygenase-like enzymes in auxin biosynthesis. Science 291: 306-309